SANDIA REPORT
SAND2008-6547
Unlimited Release
Printed October, 2008

Creating Bulk Nanocrystalline Metal

David D. Gill, Pin Yang, Aaron C. Hall, Tracy J. Vogler, Timothy J. Roemer, D. Anthony Fredenburg, Christopher J. Saldana

Prepared by
Sandia National Laboratories
Albuquerque, New Mexico 87185 and Livermore, California 94550

Sandia is a multiprogram laboratory operated by Sandia Corporation,
a Lockheed Martin Company, for the United States Department of Energy's
National Nuclear Security Administration under Contract DE-AC04-94AL85000.

Sandia National Laboratories

Issued by Sandia National Laboratories, operated for the United States Department of Energy by Sandia Corporation.

Available to DOE and DOE contractors from
U.S. Department of Energy
Office of Scientific and Technical Information
P.O. Box 62
Oak Ridge, TN 37831

Telephone: (865) 576-8401
Facsimile: (865) 576-5728
E-Mail: reports@adonis.osti.gov
Online ordering: http://www.osti.gov/bridge

Available to the public from
U.S. Department of Commerce
National Technical Information Service
5285 Port Royal Rd.
Springfield, VA 22161

Telephone: (800) 553-6847
Facsimile: (703) 605-6900
E-Mail: orders@ntis.fedworld.gov
Online order: http://www.ntis.gov/help/ordermethods.asp?loc=7-4-0#online

SAND2008-6547
Unlimited Release
Printed October, 2008

Creating Bulk Nanocrystalline Metal

David D. Gill and Pin Yang
Manufacturing Science and Technology Center

Aaron C. Hall
Material Science and Engineering Center

Tracy J. Vogler
Physical and Engineering Sciences Center
Sandia National Laboratories
P.O. Box 5800
Albuquerque, New Mexico 87185-MS1245

Timothy J. Roemer
Ktech Corporation, Cold Spray Laboratory
1800 Eubank Blvd. SE
Albuquerque, NM 87123

D. Anthony Fredenburg
Georgia Institute of Technology
Atlanta, GA 30332

Christopher J. Saldana
Purdue University
West Lafayette, IN 47907

Abstract

Nanocrystalline and nanostructured materials offer unique microstructure-dependent properties that are superior to coarse-grained materials. These materials have been shown to have very high hardness, strength, and wear resistance. However, most current methods of producing nanostructured materials in weapons-relevant materials create powdered metal that must be consolidated into bulk form to be useful. Conventional consolidation methods are not appropriate due to the need to maintain the nanocrystalline structure. This research investigated new ways of creating nanocrystalline material, new methods of consolidating nanocrystalline material, and an analysis of these different methods of creation and consolidation to evaluate their applicability to mesoscale weapons applications where part features are often under 100μm wide and the material's microstructure must be very small to give homogeneous properties across the feature.

CONTENTS

FIGURES

TABLES

1 INTRODUCTION

Nanocrystalline materials are super-materials with grain size under 100nm. This small grain size causes the materials to exhibit very high hardness and strength which could be advantageous for many applications. Additionally, the fine grain structure might also create more homogenous material properties for small features on meso scale parts. These features are often small enough that they consist of only a few grains across their width causing the material to behave differently than would be predicted by analyses using bulk material properties.

There are several size scales that all exhibit different amounts of strengthening based on grain size. Figure 1-1 shows the terminology that corresponds to different ranges of grain size for the microstructure of fine grained materials. This project has utilized powders and materials with microstructure ranging from ultra-fine grained down to nanocrystalline. Because of the methods used to make the materials, many of the grain structures used during this project actually fell into different categories depending on the orientation of the sample. The project included methods that created lamellar structures that were tens of nanometers in two dimensions with the third dimension being 100s of nanometers long. So, the range of grain size in each general definition is important, as is a description of the morphology of the particle and the morphology of the grains as well.

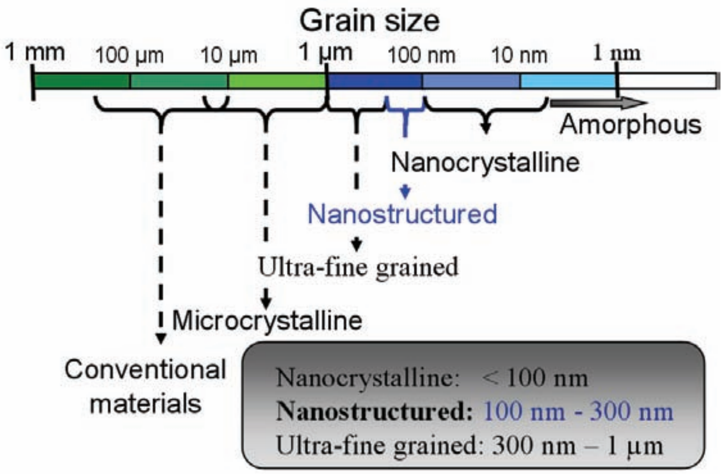

Figure 1-1 The Terminology and Grain Size Ranges Used to Describe the Microstructure of Fine Grained Materials.

The purpose of the project was to evaluate several methods of creating nanocrystalline metal, investigate means of consolidating the powdered nanocrystalline metals into bulk material, and then to perform testing and analyses on these materials to understand the microstructure and the mechanical properties.

1.1 Creating Nanostructured Material

There are numerous means of creating nanocrystalline metal and each has some advantages and some disadvantages. Figure 1-2 shows a number of the most researched means of creating nanocrystalline materials. This project used cryogenic ball milling because of its ability to create high density nanocrystalline material from high strength materials of interest to weapons designers. These materials include Inconel which was studied in the third year of the project.

The film methods were not used due to the lack of an ability to create bulk structures. Similary, equal channel angular extrusion and high pressure torsion were not used due to their inability to create nanocrystalline structures in high strength materials like Inconel.

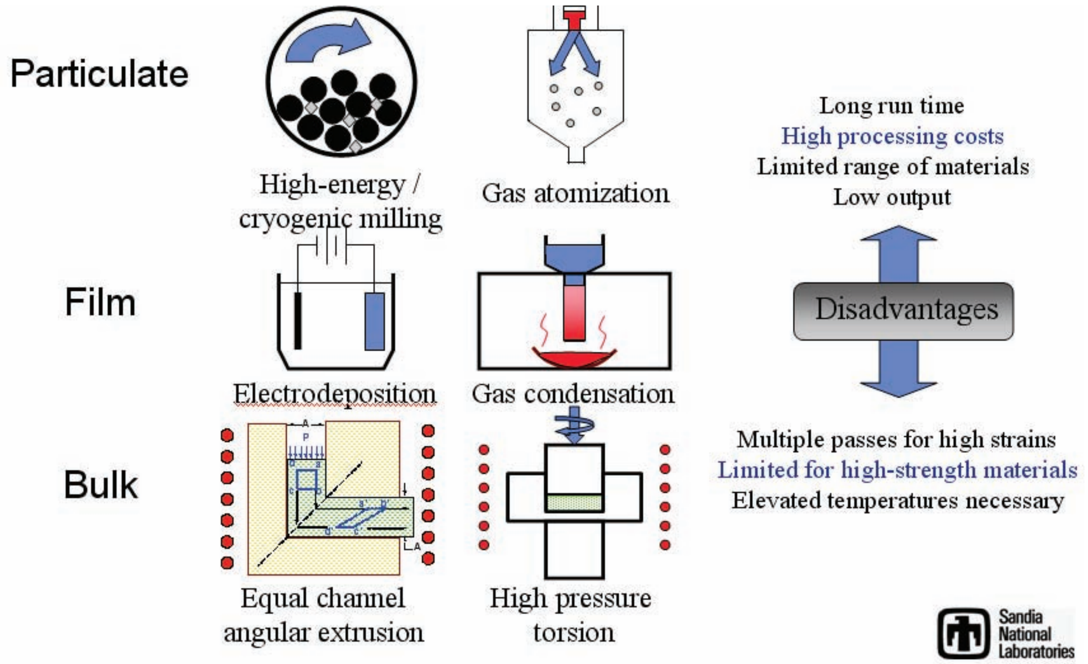

Figure 1-2 There Are Multiple Means of Creating Nanocrystalline Materials Depending on the Material of Interest, the Size of Material Required, and the Desired Material Properties.

In addition to the methods shown in the figure, two new methods of creating nanocrystalline materials were also researched and evaluated during the course of this project. These methods were Modulation Assisted Machining (MAM) and Large Strain Extrusion Machining (LSEM). MAM and liquid nitrogen ball milling, processes that create powdered metal that must later be consolidated by some means, were studied for their ability to create fully nanocrystalline material, their cost, and their ability to create powders from materials of interest to the weapons community.

1.1.1 Modulation Assisted Machining

Modulation assisted machining is a process in which a single point tool is oscillated at a high rate while cutting a workpiece. This oscillation produces a higher strain on the machined chip than is achieved in normal machining. Also, in a turning operation, the rate of oscillation can be adjusted in conjunction with the rate of rotation of the workpiece to tune for different strain and to tune for different particle (chip) morphology. The team investigated 3 morphologies including platelet, needle, and equiaxed. It was hoped that this method would be good for quickly creating nanocrystalline materials at a cost much lower than ball milling. However, research into cutting methods showed very slow chip production with hours of work producing just a few grams of material. Material was purchased from M4 Science of West Lafayette, IN. This material was prohibitively expensive for the average application. The project team investigated the material produced by this method and the results of this analysis are given in Section 3.

1.1.2 Liquid Nitrogen Ball Milling

Liquid nitrogen or cryogenic ball milling is a method used to induce significant cold work into metal powder. In the process, the powder and some type of milling balls are put into a cylinder and rotated around a horizontal axis. The repeated impact of the balls on the material induce cold work and the introduction of liquid nitrogen both makes the material more brittle and also prevents heating from the deformation process. It is important to prevent heating so that the grains in the material will not grow. The project utilized cryomilled powder which was purchased from Novemac, LLC of Dixon, CA. This powder was used in both the cold spray and the shock consolidation processes and showed great promise for both applications.

1.2 Creating Bulk Nanostructured Material

The nanocrystalline metal powders created by the methods detailed in the previous sections are often not practically usable due to the small particle size. Common methods of compacting or consolidating particles rely on high pressure or high temperature applied over a long time period which makes them unusable for the consolidation of nanocrystalline material. Extended time under high temperature or high pressure causes grain growth in the material and the unique nanocrystalline properties are lost. To address these significant challenges, the project team conducted research and experimentation on 3 potential methods of creating bulk material. The first method, Large Strain Extrusion Machining (LSEM) creates material directly from large machining chips. This method is only usable for mesoscale devices because of the difficulty in achieving machining chips large enough for macroscale parts. The next two methods rely on short duration events at high pressure. Cold spray uses the high speed impact of particles on a surface to achieve a coating. Shock consolidation uses a very short time frame impact created by a gas gun. Each of these methods was evaluated for its ability to create or maintain nanocrystallinity in the material, its ability to create fully dense bulk material, and the microstructural and mechanical properties of the material created. The three methods are described in more detail in the following sections.

1.2.1 Large Strain Extrusion Machining

Large Strain Extrusion Machining (LSEM) is a process that uses a machine tool such as a lathe to create a machining chip or foil. The lathe tool has a special gate arrangement at the back of the tool such that the foil coming off the rotating workpiece is fed through the gate. The gate helps to straighten the foil and to smooth one side somewhat. For the process, the workpiece is brought to speed on a powerful lathe and the tool is fed into the part at a high rate. A continuous foil comes out quickly through the gate at the back of the tool and feeds out rapidly until the lathe either loses power or the tool is backed away from the workpiece. The long foil created by this process has nanocrystalline properties due to the high strain event that it experienced. This foil can be lapped or machined to be flat and then mesoscale parts can be cut from the foil. The strain in the foil is controlled by the machining parameters, and the strain predicts the grain size in the final foil material.

The project team evaluated the LSEM process for making foils from which meso scale parts could be machined. As would be expected, there is significant stress in the material and this can lead to problems in utilizing the foil for precise parts with mesoscale features. The activities completed for creating and understanding this method of creating nanocrystalline material are covered in Section 2.

1.2.2 Cold Spray Consolidation

Cold spray, a new member of the thermal spray process family, can be used to prepare dense, thick metal coatings. It has tremendous potential as a spray forming process. In the cold spray process, finely divided metal particles are accelerated in an inert gas jet to velocities in excess of 500 meters/sec. When accelerated to velocities above a material-dependent critical velocity, V_c, metal particles will bond to the substrate and form a dense, well-adhered deposit, this is the foundation of the cold spray process. The cold spray process is capable of preparing deposits of low-oxide content in air at near-room-temperature conditions. This makes cold spray very attractive for many applications. Some of those applications, such as spray forming, require the cold-sprayed material to exhibit a modest amount of ductility. In their as-sprayed state, cold-sprayed metals tend to be brittle because the particles are heavily cold worked during the deposition process and interparticle bonding tends to be incomplete.

For this project, the stock metal powder used in the cold spray process was nanostructured, nanocrystalline, or ultra-fine grained, depending on the material. The team tested powders created by liquid nitrogen ball milling and by Modulation assisted machining. The tests showed the ability of cold spray to consolidate materials into a bulk material sample with relatively large dimensions. The team evaluated the use of liquid nitrogen cooling of the cold spray substrates to remove any built-up heat from the process. Figure 1-3 shows a schematic of the cold spray process as well as a sample of nanocrystalline material cold sprayed on the end of an aluminum substrate. A journal paper written to cover much of the work done during this project is presented in Section 4.

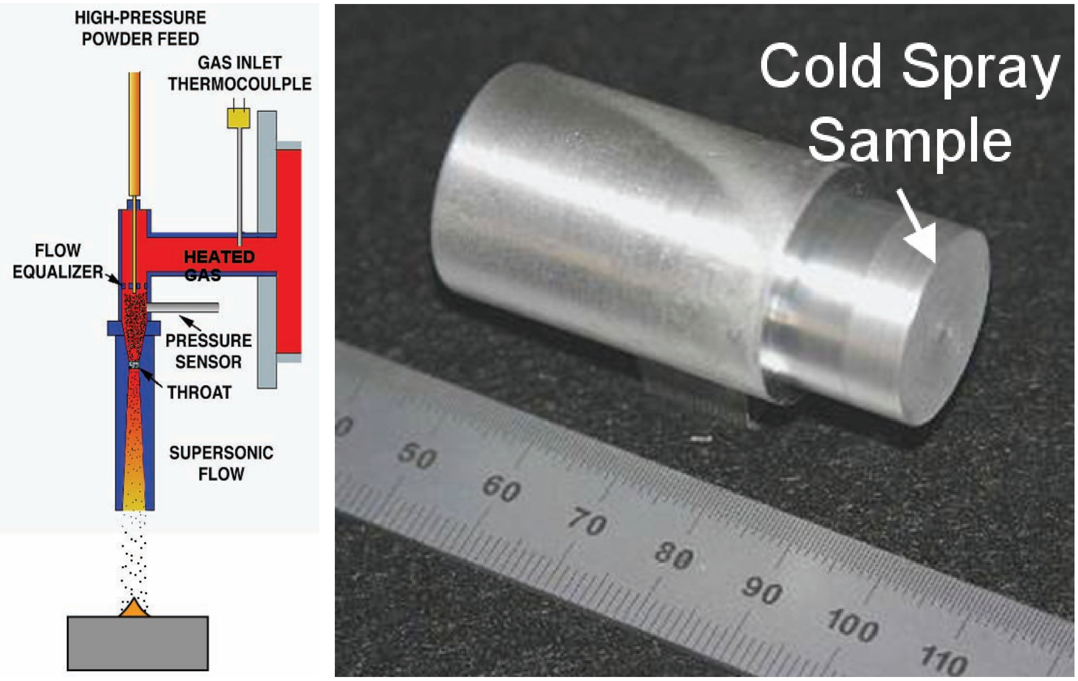

Figure 1-3 Schematic of the Cold Spray Process (left) and a Cold Sprayed Aluminum Sample Deposited On the Right-End of the Bar (right).

1.2.3 Shock Consolidation

The shock consolidation process was used due to the high rate of impact which prevents excessive heat build-up. The shock testing was performed at Sandia National Laboratories and utilized the two gas guns shown in Figure 1-4 as well as an 80mm gas gun at Georgia Tech University. The remainder of this section of text has been adapted from the Ph.D. proposal of team member D. Anthony Fredenburg.

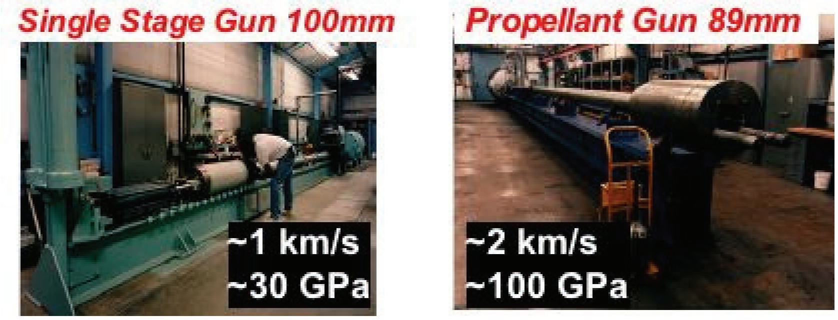

Figure 1-4 These Gas Guns were Used in the Shock Consolidation of Nanocrystalline Metals.

Shock Compression of Solid and Porous Media

When a stationary material is impacted under intense dynamic loading conditions, large compressive stress waves are induced in both the impacting material and the body initially at rest. The stress waves produced can take several forms [1-1], and are largely dependent upon the impact velocity and mechanical properties of the material through which the wave is travelling. A strong shock is characterized by a stress pulse with a constant speed and near instantaneous rise to peak pressure; the front is relatively thin and discontinuities exist across the front. Relationships have been developed to correlate the state of material ahead of and behind the discontinuous front through conservation of mass, momentum, and energy. They are termed the Rankine-Hugoniot relationships and serve to connect the particle velocity U_p, shock velocity U_S, specific volume $V = 1/\rho$ = 1/density, pressure P, and specific internal energy E [1-2]:

$$U_P - U_0 = U_S(1-V/V_0) \qquad \text{(Mass Conservation)} \qquad (1)$$
$$P - P_0 = (U_S/V_0)(U_P-U_0) \qquad \text{(Momentum Conservation)} \qquad (2)$$
$$E - E_0 = \tfrac{1}{2}(P+P_0)(V_0-V) \qquad \text{(Energy Conservation)} \qquad (3)$$

where the subscript $_0$ indicates initial values for the uncompressed state. The assumptions inherent in the above relationships require that the pressure, volume, and energy states measured are in thermodynamic equilibrium, and that the amount of compression for a given applied pressure is the same as would be produced by a hydrostatic pressure of equal magnitude [1-2]. The first assumption requires a very narrow shock front, and the second is valid for applied pressures that far exceed the yield strengths of the solids; effectively restricting the application of the above relationships to strong shocks. In addition to the above equations, a fourth relationship, commonly referred to as the equation of state (EOS) is required. For inert solids a linear relationship between U_S and U_P has been found to be valid for many materials at pressures below ~100 GPa. The EOS for a non-reacting solid material in response to a strong shock takes the form [1-2]:

$$U_S = C_0 + S_1 U_P \qquad (4)$$

where C_0 is the sound speed of the material and S_1 is a material constant. Once any two of the unknown variables are experimentally determined, it is possible to derive all other unknowns through these four equations.

Using these relationships one can construct a compressibility curve for the material, termed the 'Hugoniot', which shows the response of a material in pressure-volume (P-V) space. The curve, illustrated in Figure 1-5, is not a continuous pressure-volume path, but rather the location of attainable shock states. The line joining the initial and final states of the shocked material represents the actual path of the material under shock loading, referred to as the Rayleigh line, and is proportional to shock speed.

The energy imparted during impact is the area under the Rayleigh line, and during subsequent release to ambient pressure the energy absolved is the area under the release isentrope, which is often approximated as the Hugoniot curve. Thus for a solid system, the total energy retained (dashed area in Figure 1-5) is the area between the Hugoniot and the Rayleigh line. With the passage of a strong shock, stress values in a porous media can reach values near or above the "crush strength" (point C in Figure 1-5), an applied stress that will compress a material to full density. As such, upon release to ambient pressures the energy absolved is often approximated by the area under the corresponding solid Hugoniot. The amount of energy retained by a porous material is much greater than that of a solid for similar pressures, as shown in Figure 1-5, where the release isentrope for the porous sample is separated from the solid Hugoniot and follows the path A' → C → O.

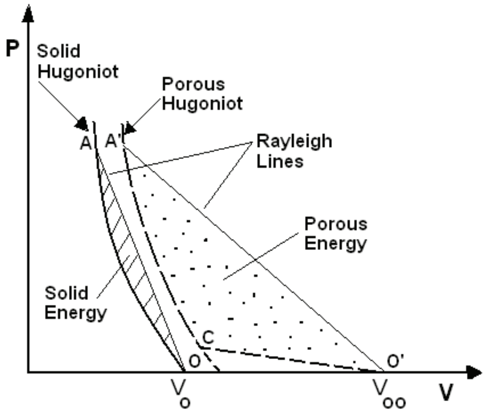

Figure 1-5 Stress-Volume Hogoniot for Non-Reactive Solid and Porous Materials. V_{oo} and V_o Indicate the Initial Specific Volume for Porous and Solid Material, Respectively.

In order to develop the Hugoniot of porous materials, various EOS have been proposed to relate material properties in the porous and condensed states. One such EOS is the Mie-Grüneisen equation of state, relating the pressure and internal energy difference between the porous and solid states. The Mie-Grüneisen EOS is [1-2]:

$$P - P_K = (\gamma/V)(E - E_K) \tag{5}$$

where γ is the Grüneisen parameter and P_K and E_K represent the pressure and specific internal energy at zero Kelvin, respectively, such that γ can be assumed as only a function of volume. Though useful in establishing compressibility curves for heterogeneous mixtures, application of the Mie-Grüneisen EOS has shown that substantial deviations occur between predicted and experimental results for porous media due to the constant volume assumption and large dependency on obtaining an accurate γ function.

Shock Compaction of Powders

Transforming a powder from its initial loosely associated state to final solid density state is a complicated process, and becomes even more involved when dealing with heterogeneous powder mixtures. Several models have been developed that describe the compaction process for homogenous powders and will be subsequently discussed; however, a complete model describing the compaction of heterogeneous powders (mixtures) is still lacking.

One such model developed for ductile distended or porous materials is the so called “P-α” model proposed by Herrmann [1-3] to provide a description of the compaction behavior at low stresses and the correct thermodynamic behavior at higher stresses. The complete equation of state relates the pressure *P*, specific volume *V*, and specific internal energy *E* through [1-3]:

$$P = f(V/\alpha , E) \; (6) \qquad \text{and} \qquad \alpha = g(P, E) \quad (7)$$

where α is the porosity defined as the ratio of the specific volume of the porous material to the specific volume of the analogous solid density material ($\alpha = V_{oo}/V_o$). Defining α as such allows the change in volume due to bulk compression and pore collapse to be separated. This equation is based on the assumption that the relation between pressure, specific volume, and specific internal energy for the matrix material is the same for the porous and nonporous states, and that the surface energy of the particles is negligible. Herrmann suggests that the initial compression of a highly porous material is elastic and is a result of the buckling of the particle walls. Once the elastic limit of the particles is reached, plastic deformation begins to occur as the particle walls permanently deform and the pores collapse. As porosity decreases toward unity and approaches that of a solid material, the bulk of compression will be due to volume compression of the material, with little change in porosity. This concept is illustrated schematically in Figure 1-6 for multiple loading and unloading schemes.

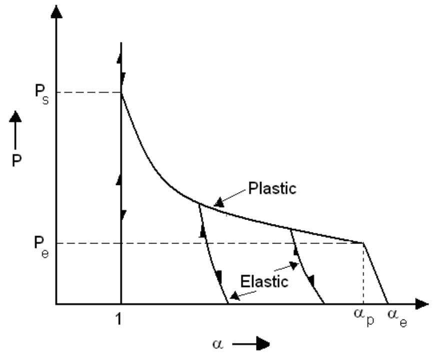

Figure 1-6 Illustration of Elastic and Plastic Region of Compression in P- α Model for Loading and Unloading.

Modifying Herrmann's P-α model, Carroll and Holt [1-4] included an additional term supposing the volume average of the stress in the matrix is a pressure P_m, and not P, such that:

$$P_m = \alpha P \qquad \text{and} \qquad P = \alpha^{-1} f(V/\alpha, E). \tag{8}$$

Building upon the above relation and extending the work of Mackenzie [1-5] to the dynamic regime, Carroll and Holt [1-6] developed a model for the compaction of a porous material assuming pore geometry is only a function of initial porosity and pore diameter. This pore collapse relation is expressed:

$$\alpha = 1 + (\alpha_p - 1)\{(P_S - P)/(P_S - P_E)\}^2 , \tag{9}$$

where α_p is the distention achieved during elastic compression, P_E is the elastic compression pressure, and P_S is the crush strength. This spherical shell model assumes that pores in a material collapse in the same manner as would a hollow sphere of the matrix material, and that during pore collapse there is incompressibility of the matrix. Using a finite difference computer code they have shown that compression of aluminum hollow spheres occurs in three distinct phases, a purely elastic phase, an elastic-plastic phase, and a purely plastic phase where change in porosity occurs almost exclusively in the plastic phase. These distinct phases are observed during both static and dynamic compaction.

Similar observations are made for extremely distended ceramic powders under static compression; suggesting three defining stages in the compaction process [1-7]. At low initial pressures the first stage is characterized by particle rearrangement with little to no fracture occurring. During this stage intimate contact is established with neighboring particles such that voids or pores are formed between the particles. The second stage, characteristic of an increased applied load, will exhibit either deformation or fracture of the particles, and allows for additional rearrangement. At higher loads still, the particles or granule fragments undergo further rearrangement. It is supposed that all three stages occur simultaneously with one being the dominant process for a specific pressure range [1-7].

It has been proposed by Raybould [1-8, 1-9] and supported by others [1-10 - 1-12] that, if the applied pressure is high and the width of the shock front short, during dynamic compaction particles are thrown against one another so violently that oxide layers can be broken. Heat is also generated at interparticle contacts as a result of friction and deformation of moving particles, and temperatures can reach that of the melt. For melting at the particle surfaces to occur, Raybould [1-13] has introduced a criteria for shock rise-time which requires the rate at which the energy of the shock is deposited must be greater than the rate of heat conduction to the particle interior, and has shown this criteria can be reached for lead, aluminum, and steel powders at impact velocities of 500, 1000, and 1000 m/s, respectively [1-8]. In an attempt to quantify the process of energy deposition and resultant microstructural changes during dynamic compaction a model has been proposed by Gourdin [1-14 - 1-17]. This model, shown in Figure 1-7, relates the energy flux at the particle surface F_o to the specific energy behind the shock E, the rise time τ, and the specific area of the powder A,

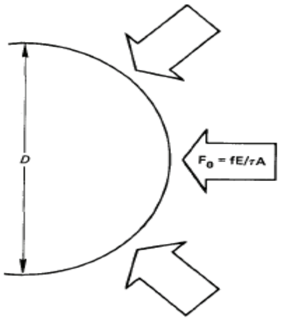

Figure 1-7 Schematic Illustration of the Flux Model Developed By Gourdin, Where the Flux is Represented as F_o.

and provides a quantitative link between shock conditions, powder characteristics, and the final microstructure of the compact. Good agreement between model and experiment has been found for 4330V steel, aluminum-6% silicon, and copper powders. Separate investigations by Roman, Nesterenko, and Pikus [1-18] and Gourdin [1-19] on how particle size effects melting have been conducted and show that for a homogenous monodispersed powder the amount of dynamic densification and subsequent melting is increased as the particle diameter is increased.

Particle Packing

The dynamic compression of heterogeneous powder particles is a complicated process and is far from well understood. However, with a solid theoretical understanding of the packing of powder particles and the use of computer simulations to observe the mesomechanics of deformation and flow during compaction, one can begin to estimate, and even predict, the behavior of heterogeneous powders under dynamic compression. It is intuitive to begin with the ideal scenario for packing of powder particles, then consider some of the physical interactions that occur between particles, followed by an examination of the actual process of compaction.

It is well established [1-19] that a narrow bimodal distribution of powder particle size will lead to a higher density than that of a unimodal distribution. According to Cumberland and Crawford [1-20] a dense mixture of heterogeneous spheres can be formed in two ways. First, one can start with a large sphere system in dense random packing and insert small spheres into the existing voids without disturbing the arrangement of the large spheres. If random dense packing is assumed for both the large sphere matrix and the small sphere interstitials, then the fractional solid content (FSC) for both the large spheres, v_1, and the small spheres, v_2, is $v_1 = v_2 = 0.625$. The minimum fraction by weight of the coarse particles, C_{min}, such that density is maximized is then determined through:

$$C_{min} = v_1 / (v_1 + v_2 - v_1 v_2) \qquad (10)$$

and is equal to 0.73. The optimal FSC, V'_{opt}, for the mixture is accordingly:

$$V'_{opt} = v_1/C_{min} = v_1 + v_2 - v_1 v_2. \qquad (11)$$

For a random dense packing of large spheres with a similar packing of small spheres in the intersticies, the optimal FSC for the mixture is 0.86. The other option for obtaining a dense mixture is to start with a matrix of small spheres and subsequently add large spheres until the number of large spheres increases to the point where there is a matrix of large spheres in dense random packing and small spheres in the intersticies. Similar to the previous scenario, the weight fraction of large spheres to small spheres that maximizes density is $C_{min} = 0.73$ and the optimal FSC for the mixture is 0.86. This approach assumes that both large and small spheres have the same density. However, if the densities of the large and small spheres are not the same, then the weight fraction of large spheres that maximizes density is:

$$C_{min} = v_1\rho_1 / (v_1\rho_1 + (1-v_1)v_2\rho_2) \tag{12}$$

where ρ_1 and ρ_2 are the densities of the large and small particles, respectively. In practice however, densities achieved by mixing of heterogeneous powders are almost always lower than theoretical prediction.

When real powder particles are mixed, additional considerations must be taken into account when attempting to achieve dense packing, especially as particle size is decreased. It has been found that as particle size decreases and the surface area to volume ratio of the particles increases, friction, adhesion, and other surface forces begin to play a more important role in the arrangement of particles [1-21]. For particle sizes less than 100 μm, gravity is no longer the dominant force and body forces such as van der Waals and electrostatic forces begin to dominate and become more influential as particle size decreases, with electrostatic forces only becoming significant for particle sizes less than 1 μm [1-22]. These attractive forces can lead to lower coordination and an increase in porosity as particle size decreases, as well as the formation of agglomerates. Surface effects also become more dominant as particle size decreases. As the surface becomes increasingly more rough, the sliding and rolling friction coefficients increase which inhibit the motion of particles, leading to more porous structures [1-23]. Irregularity of particle shape, though decreasing the van der Walls attractive force, can increase the porosity as an irregular shaped particle can bridge the gap between two adjacent particles, leading to the formation of voids beneath the particle [1-24].

Die filling can also have a substantial effect on the initial density of the particles [1-21]. It has been observed that as the intensity of particle deposition increases, i.e. the number of spheres falling per unit time per unit area, in the range between 100-1400 particles/in^2-s the packing efficiency improves. Conversely, increasing the height at which the particles are dropped tends to decrease the packing efficiency; where there is an optimal height of drop for a given intensity of deposition that will produce the closest packing. Cumberland and Crawford [1-21] also reported that a large container to particle size ratio is necessary to ensure the most close-packed particle arrangement, on the order of ~50:1. High frequency, low amplitude vibration during packing has also been found to increase the packing efficiency, especially for irregular shaped particles because they can fit into the indentations and irregularities of neighboring particles. Location and arrangement of powder particles during mixing or filling is important, especially in heterogeneous powder mixtures, because significant segregation can occur which can lead to density gradients and non-uniformity in compacts.

Consolidation of Particles

The mechanics of compaction for the quasi-static and dynamic regime vary greatly and produce compacts with significantly different characteristics. However, a general relationship has been developed that can be used to predict the pressures necessary to produce a certain density compact in both the quasi-static and dynamic regimes. This relationship, known as the Fishmeister-Artz relationship [1-25], is given by:

$$P_y = 2.97\rho^2(\rho-\rho_0)/(1-\rho_0)\sigma_0 \tag{13}$$

where P_y is the pressure needed to achieve a density ρ, starting from an initial density of ρ_0, where the powder mixture has an effective yield strength of σ_0. This model, originally developed for the compaction of homogeneous mono-sized spheres, can also be used as a rough approximation for predicting the pressures necessary to compact heterogeneous powder mixtures. In an effort to better understand the different phenomena occurring during quasi-static and dynamic compaction, simulations on homogeneous mono-sized spheres have been carried out at different impact velocities [1-26]. The authors have shown that during quasi-static compaction, plastic strain is generally initiated and spread throughout the contact regions between particles, whereas during dynamic compression plastic strain initiates near the impact surface and travels in the direction of stress propagation. The development of plastic strain from an array of monosized spheres modeled in two dimensions is shown in Figure 1-8. Note that at the low impact velocity of 300 m/s the strain develops at the contact points between particles and grows outwardly, showing quasi-static compression characteristics and leads to a hexagonally shaped particle. For the higher impact velocity of 1000 m/s the plastic strain travels in the direction of wave propagation, leading to very low plastic strains in the particles ahead of the stress front and high plastic strains behind the front. This causes the lower particles to behave as rigid bodies, such that the upper particles will deform on to the top of the lower particles [1-26], as shown in Figure 1-9. Other important parameters investigated [1-26] are interparticle friction, strain hardening, and particle size. It has been found that interparticle friction effects increase under dynamic compaction because of the increased particle shearing that occurs along the particle surfaces. An increased amount of strain hardening in a particle will not change the overall shape of the particle, but rather increases the temperatures generated during dynamic compaction. Decreasing particle size causes an increase in temperature when both small and large particles are subjected to the same particle velocity because there is an increase in strain rate for the smaller particle [1-26].

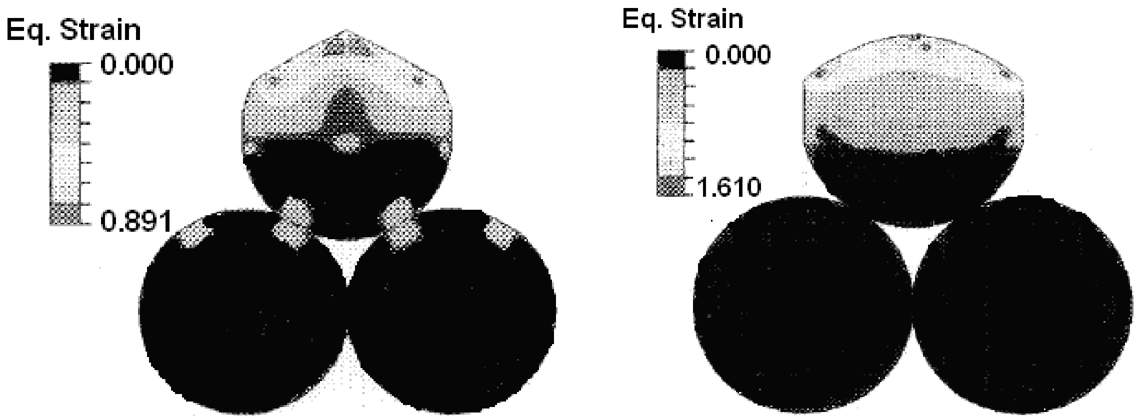

Figure 1-8 Equivalent Plastic Strain for Two-Dimensional Cylinders Compacted at 300 m/s (left) and 1000 m/s (right).

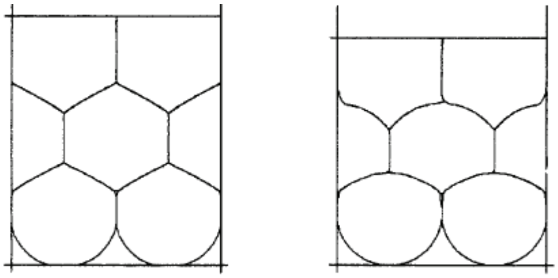

Figure 1-9 Resultant Shape From Two-Dimensional Compaction of Cylinders at 300m/s (left) and 1000m/s (right).

The preceding analysis deals with an idealized system of homogeneous mono-sized spheres, and it is expected that for heterogeneous systems composed of ductile and brittle components with varying particle sizes and volume fractions, behavior during compaction will be quite different. For simulated mixtures of ductile and brittle particles [1-27] preferential deformation of the ductile particles occurs during compaction. If the volumetric percentage of the ductile component is high enough, the brittle particles can become surrounded by a ductile matrix without undergoing much, if any, deformation or fracture [1-27]. However, when the amount of ductile component is limited, the strength of the compact is dominated by the brittle component and compaction occurs by fracture and rearrangement of the brittle particles. In a compaction study on Cu-W, a system composed of ductile and brittle components, optimal mechanical properties were observed for mixtures containing 20-50% of the brittle tungsten particles [1-28]. The effect of particle size, shape, strength, density, etc., is expected to be very influential on dynamic compaction characteristics.

2 FABRICATION OF NANOSTRUCTURED INCONEL 718 BY LARGE STRAIN EXTRUSION MACHINING

In an effort to create low cost nanocrystalline material, the team investigated the use of material from the Large Strain Extrusion Machining (LSEM) process. This work, done in conjunction with team members from Purdue University, characterized LSEM material, created parts from LSEM material, and evaluated its performance. The text in this section is from a paper by Pin Yang that will be submitted at a later time. Coauthors on the paper include David Gill and Michael Saavedra of Sandia National Laboratories and Christopher Saldana, James B. Mann, Willie Moscoso, Srinivasan Chandrasekar, and Kevin P. Trumble of Purdue University.

2.1 Abstract for Large Strain Extrusion Machining

This study investigated the feasibility of fabricating nanostructured engineering alloys by a low-cost, severe plastic deformation process. Special focus was placed on large strain extrusion machining of solution treated and precipitation hardened Inconel 718 alloy as a precursor material for manufacturing of mesoscale parts. This approach and its generalization are shown to be well suited for production of small components and structures of high-aspect ratio from nanostructured alloys. Correlations between the amount of strain induced by the extrusion machining and microstructure evolution, as well as the mechanical performance were established. In addition, the hardness evolution and thermal stability of a solution treated, strain refined nanostructured Inconel were investigated. Prototyping of meso-scale parts with nanostructured Inconel super alloy was demonstrated.

2.2 Introduction for Large Strain Extrusion Machining

Meso-scale components play an important role in system miniaturization. The size reduction from a mechanical clock to a wrist watch is a practical example of the past. Emergent needs ranging from stronglink components, satellite flexures, microelectromechanical systems (MEMS), to compact biomedical devices are just a few examples looming. These meso-scale components vary from a few millimeters (10^{-3} m) in size to the finest feature of few microns (10^{-5} m), and normally carry higher mechanical stresses, experience severe sliding contact, and sustain greater torque [2-1]. Therefore, high strength-to-weight ratios are critical for the miniaturization of structural components. Sometimes, thermal stability is also required during high temperature brazing or diffusion bonding to assure hermeticity of the micro-systems and to protect these components from hazardous environments. In addition, feature sizes in micro-scale components are often on the same order as the grain size when conventional microcrystalline alloys are used as precursor materials, a potentially undesirable mechanical design condition [2-2]. For these reasons, ultrafine grained (UFG) and nanostructured alloys with enhanced strength and hardness are attractive candidates for micro-system applications.

In the 1990s, LIGA (German acronym for Lithographie, Galvanoformung, Abformung) emerged as an important process for making small-scale components out of electro-formable metals such as nickel. The electrochemically-deposited metal is typically nanocrystalline, with high strength and hardness. Perhaps, a more versatile manufacturing approach for making 3-D micro-scale components is by direct fabrication from bulk nanostructured materials using conventional micro-machining processes such as electro-discharge machining (EDM), electro-chemical machining (ECM), micro-milling, and femto-second laser beam processing [2-1]. These processes have the advantage of being applicable over a broad parameter space both in terms of materials and component geometries [2-1, 2-3], and are capable of overcoming the low machining efficiency imposed by these high strength materials through traditional machining process. For example, micro-EDM is used to make 3-D structures and features down to a few micrometers in size and of high-aspect ratios for fuel system components, jet-engine turbine blades and micro-power systems [2-1]. However, central to this approach is the availability of high-strength nanostructured materials in bulk forms.

The challenge of creating bulk nanostructured materials from high-strength alloys can now be at least partially addressed with severe plastic deformation (SPD) techniques [2-4, 2-5]. Conventional SPD techniques like Equal Channel Angular Pressing (ECAP) are well developed to the stage where bulk nanostructured materials can be routinely produced from alloys of initial low or moderate strength. A few high-strength, nanostructured alloys can also be made by these techniques by heating the precursor bulk material to elevated temperatures during the SPD, with some attendant trade-off in the level of microstructure refinement[2-6]. Recently, a new class of SPD processes based on large strain machining has emerged; a constrained variant, large strain extrusion machining (LSEM) is used in the present work. These machining processes are well suited for SPD of difficult-to-deform alloys (e.g., Inconel, Ti alloys, stainless steels, Ta) by chip formation, without pre-heating of the bulk microcrystalline material[2-7 – 2-10]. LSEM, in particular, is capable of not only affecting microstructure refinement by imposition of large plastic strains, but is also amenable for producing bulk chips with controlled geometry (e.g., foil, sheet, wire, bar) and UFG and/or nanocrystalline microstructures.

In this study, a low-cost production of nanostructured Inconel 718 in bulk foil/sheet forms using LSEM is first demonstrated. This approach and its generalization are shown to be well suited for production of small components and structures of high aspect ratio from nanostructured alloys. In the next few sections, a brief background on the LSEM process is reviewed and various microstructures developed under different processing conditions (shear strain induced by LSEM process) and their mechanical performances are reported. Fabrication of micro-scale components from high-strength Inconel foils were then demonstrated, using a wire micro-EDM process. In addition, the effect of thermal aging (or precipitation hardening) on the microhardness of nanostructured Inconel is compared.

2.3 Background for Large Strain Extrusion Machining

Imposition of large plastic strains is the most effective method to produce bulk metals with ultra-fine grained (UFG) and nanocrystalline microstructure[2-9, 2-11 – 2-13]. Materials with the refined microstructure generally possess a significantly improved strength and hardness as compared with their microcrystalline counterparts [2-8, 2-13]. Large plastic strains can be introduced by SPD methods such as wire drawing [2-11], equal channel angular pressing [2-12, 2-13], high-pressure torsion [2-4, 2-14], and rolling [2-15]. Most of these processes involve multiple passes of deformation to achieve a desired microstructure and enhanced mechanical properties. However, this practice becomes progressively more difficult as material is cumulatively strengthened by each deformation cycle. This is particularly true for high-strength materials where tooling difficulties have usually precluded using these methods without some preheating above ambient levels. These constraints make the aforementioned methods cumbersome, time-consuming and expansive to scale up for large volume production.

Simplicity of chip formation in plane-strain machining enables grain refinement by SPD at near-ambient temperatures in the full range of commercial alloys, including high-strength alloys which are difficult to process by conventional SPD [2-7 – 2-10]. LSEM is the experimental configuration used to create bulk foil samples under controlled conditions of strain and strain rate [2-9]. Figure 2-1 illustrates an LSEM process wherein a bulk foil/sheet sample (chip) of controlled thickness is produced by machining and extrusion imposed in a single step using a specially designed tool. The tool consists of two components – a bottom section with a sharp cutting edge inclined at a rake angle (α) and a wedge-shaped top section that acts as a constraining edge. The tool moves radially into a disk-shaped workpiece rotating at a constant peripheral speed, V. The chip is simultaneously forced through an ‘extrusion’ die formed by the bottom rake face and the top constraining edge, thereby effecting dimension and shape control. The velocity of the material at the exit of the tool is $V_c = Vt/t_c$, where t and t_c are the undeformed and deformed thickness of the chip, respectively. LSEM, unlike conventional machining, involves chip formation by constrained deformation where the deformed chip thickness is controlled *a priori*. Thus, microstructure refinement by large strain machining is effected in combination with shape and dimensional control.

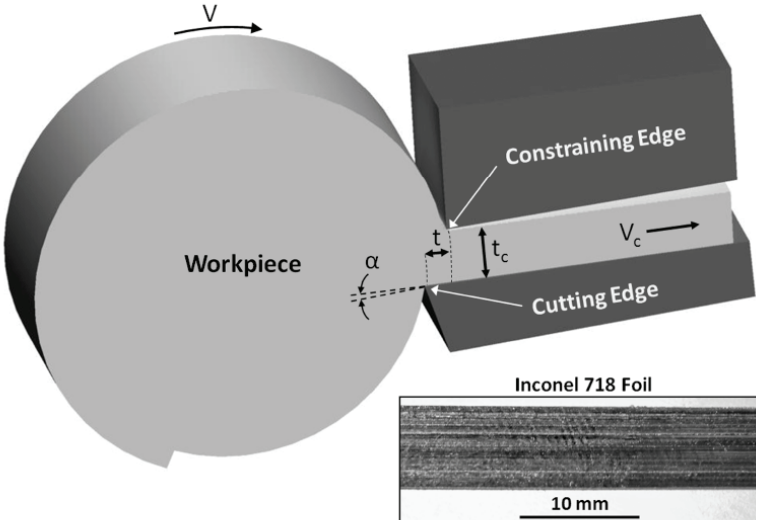

Figure 2-1 Schematic of Large Strain Extrusion Machining (LSEM). Insert at the Bottom Right Shows a Typical Inconel 718 Foil Strip Created Using This Process

The LSEM process produces bulk UFG and nanostructured materials at small deformation rates that suppress *in situ* heating and microstructure coarsening [2-10]. LSEM can be considered a generalization of ECAP with the exception that the thickness of the material at the tool exit can be different than that at the inlet. This ensures imposition of strain levels that are sufficiently high to induce formation of an UFG microstructure in a single-step deformation process. The shear strain (γ) imposed in the foil/sheet sample is determined by the extrusion (chip thickness) ratio ($\lambda = t_c / t$) and the rake angle, α, as [2-10, 2-16]:

$$\gamma = \frac{\lambda}{\cos\alpha} + \frac{1}{\lambda\cos\alpha} - 2\tan\alpha \qquad (1)$$

A wide range of strain (1-10) can be imposed in the foil/sheet samples by varying α and λ in a single pass of the cutting tool, while strain rate can be varied by varying the velocity of LSEM; to first order, the strain rate varies linearly with velocity. Most importantly, bulk foil/sheet samples with UFG and nano-scale microstructures can be created even from high-strength alloys at near-ambient temperatures [2-6 – 2-8]. The process produces good surface quality, uniform properties over several meters of extruded chip [2-10], and is versatile for fabrication of bulk materials in the form of foils, bars and wires [2-11]. Therefore, LSEM is an excellent candidate to make foil sheets that can serve as precursor materials for the meso-scale components.

2.4 Experimental Procedure for Large Strain Extrusion Machining

LSEM was used to produce bulk Inconel foils having UFG microstructure for manufacturing of small-scale components and mini-tensile specimens for mechanical evaluation. For this purpose, the as-received, precipitation hardened bulk Inconel 718 alloy was solution treated at 1035˚C for 1 hour followed by a rapid air quench, in order to ensure that any precipitates that were initially present went into solution. The initial grain size in the solution-treated Inconel 718 was ~50 μm, as measured by the line intercept method, and the Vickers hardness after the solution treatment was ~2.16 GPa. Additional hardness and elastic modulus were determined by a MTS nanoindenter XP system, based on the force-displacement curve. To account for the influence of elastic unloading on the projected area of the indentation impression, the Oliver-Pharr method [2-17] was used. The elastic stiffness (S) was obtained from the slope of the unloading curve. Elastic modulus can then be determined by the contact area (A_c), Geometry ratio for Berkovich indentation tip ($\beta = 1.024$), and Poissons ratio (ν) through the following expression,

$$E = \frac{\sqrt{\pi}}{2\beta(1-\upsilon^2)}\frac{S}{\sqrt{A_c}} \qquad (2).$$

Chips in the form of bulk foils were created from the solution-treated material by LSEM at a speed of 40 m/min with tungsten carbide tools having rake angles of 0˚ and +15˚. The undeformed chip thickness was ~130 μm and the width of cut was 6 mm. Using Eqn. 1, the strain in the foils was estimated as 2.1 (t_c = 260 μm) and 3.5 (t_c = 415 μm) for the +15˚ and 0˚ rake angle tools, respectively. Foils of different shear strains were made by a CNC Fryer lathe. Hardness and microstructure of the foils were characterized by Vickers indentation and transmission electron microscopy (TEM). For the hardness measurements, 20 indents, each at least 50 μm in size, were made on 3 samples for each condition. The microstructure of the foils was examined using a JEOL 2000FX TEM operating at 200 KeV. TEM samples were prepared by mechanical thinning of the chips to ~150 μm, followed by electrolytic thinning in a Struers Tenupol-5 using a solution of 25% HNO_3 and 75% CH_3OH.

Tensile testing was performed by dog-bone shape mini-tensile specimens fabricated from LSEM foils by micro-EDM process on a Sandia developed test system (see Figure 2-2). Prior to the micro-EDM process, the LSEM foils were first flatten and then about 10 µm surface layers (the secondary deformation arising from tool-chip friction) were removed by lapping. Sample was loaded and aligned in a custom built fixture before testing. The system was controlled by the Teststar programmable controller (MTS Inc, Mineapolis, MN) under a strain rate of 25.4 µm (or 0.001")/second. Strain was measured with an optical extensometer (Keyence LS7000 LED shadow edge detection).

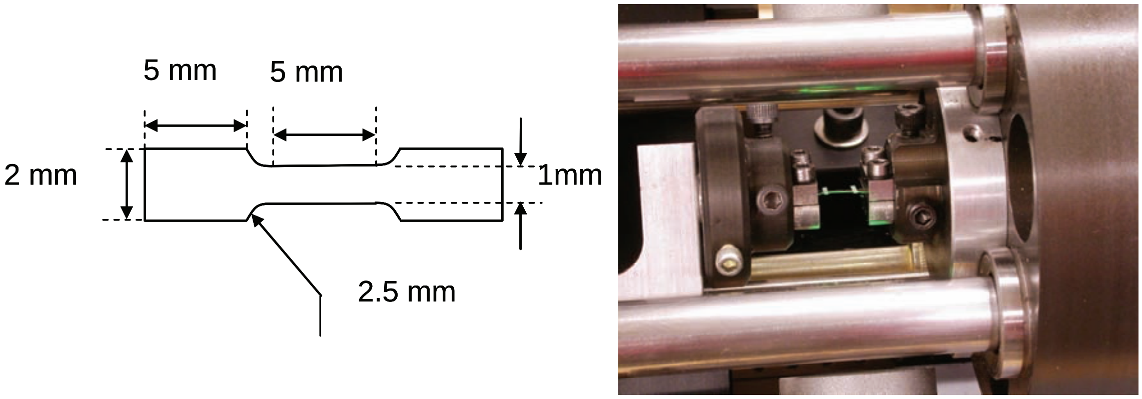

Figure 2-2 The Schematic of Physical Dimensions of a Mini-Tensile Test Specimen and Tensile Test System with an Optic Extensometer.

Prototype micro-scale components – spur gears with ~2 mm diameter – were produced from the foils by micro-EDM. This component geometry was selected because it incorporates sufficiently complex features of high-aspect ratio typical of 3-D micro-components [2-1, 2-18]. A wire electrical discharge machine (Agie AC Vertex 2F) was used to machine the gears from the foils. Machining was carried out using low-energy discharges with a high pulse rate, conditions that are ideal for machining of micro-scale features. Feature sizes as small as 40 μm were achieved as determined by OGP Avant video measurement system. De-ionized water was used as the dielectric medium. EDM process created about 1 μm thick recast layer with rough appearance on the surface. The gears were subsequently electro-polished using a mixture of sulfuric acid (73 Vol. %), glycerol (20 Vol.%), and water (7 Vol.%) to obtain a smooth surface finish [2-19]. The electro-polishing was performed with 220 mA current for 60 seconds with a custom designed tungsten spring as electrical contact. The gears were characterized using a scanning electron microscope (SEM, JEOL JSM-6490LA).

2.5 Results and Discussion for Large Strain Extrusion Machining

2.5.1 Shear Strain and Hardness

Figure 2-1 (inset) shows a typical Inconel foil produced by LSEM of the solution treated material. The foils were approximately 600 mm long and 6 mm wide. The straightness of the foils facilitated subsequent processing. The hardness values of the foils created with shear strain (γ) of 2.1 and 3.5 were 4.84 ± 0.22 GPa and 5.51 ± 0.11 GPa, respectively. These values, determined by the Vicker hardness, are much greater than the hardness (2.17 ± 0.07 GPa) of the solution treated bulk microcrystalline Inconel, suggesting a significant level of microstructure refinement during LSEM. Indeed, the foil hardness values are nearly that of aged (or precipitation hardened) microcrystalline Inconel 718 (4.12 ± 0.05 GPa). In comparison to a LSEM foil created from a bulk precipitation hardened Inconel 718 (shear strain unknown), the hardness value of this material reached 5.46 ± 0.11 GPa which is 32.6% increase for the bulk microcrystalline material. Uniaxial tensile test results from the foils showed increases in strength that are directly proportional to the increases in hardness [2-20].

These experiments were repeated with 4 different strain values (up to 4.1) to establish correlations between processing conditions with the hardness and microstructure by nano-indentation and TEM. Indentation impressions and the force-displacement curve for a chip deformed to strain of 1.5 is given in Figure 2-3, with indentation depth controlled at ~ 1 μm and indents ~ 20 µm apart. The average hardness and modulus were obtained from 15 indents for each condition. Results of the measured hardness and modulus data are given in Table 2-1. Results indicate that the hardness increases while the modulus decreases with the increase of shear strain. The increase in hardness can be attributed to microstructural refinement induced by SPD where dislocations are hindered by the grain boundary and plastic deformation becomes more difficult, as shown by a classic Hall-Patch behavior. Most modulus values determined from the nanoindentation technique are lower than the bulk modulus of microcrystalline Inconel 718 (~215 GPa). Many researchers have attribute to the decrease in modulus to the increase of grain boundary areas in these hard UFG materials.

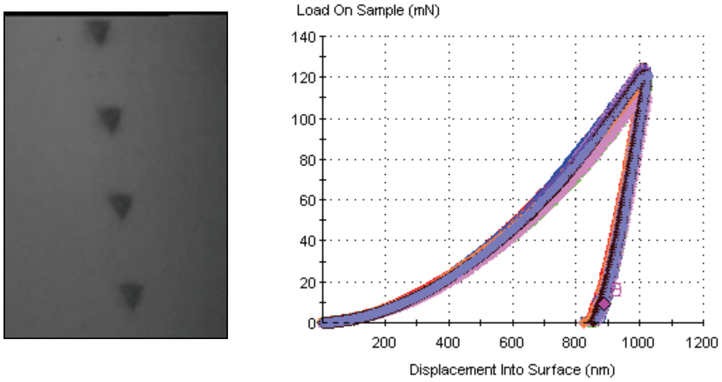

Figure 2-3 Indents and Force-Displacement Curve for a Chip Deformed to Strain of 1.5. The Increase and Decrease in Loading with Respect to the Displacement Correspond to the Loading and the Unloading Conditions Respectively.

Table 2-1 Hardness and Modulus of Solution Treated Extrusion Machined Inconel 718 as Measured by the Nano-Indentation Technique.

Hardness (GPa)					
Rake angle, °	-20	-5	+5	+15	+45
Shear Strain[†]	4.1	3.9	2.7	2.3	1.5
Average	6.7	6.1	6.3	5.9	5.5
Std Dev	0.35	0.31	0.21	0.28	0.25

Elastic Modulus (GPa)					
Rake angle, °	-20	-5	+5	+15	+45
Shear Strain[†]	4.1	3.9	2.7	2.3	1.5
Average	163	173	159	181	192
Std Dev	6.5	7.0	3.9	5.5	8.7

[†] The amount of shear strain was controlled by the raking angle in a LSEM process.

2.5.2 Microstructure of Large Strain Extrusion Machining

Direct measurements of strain and strain rate in chip formation using Particle Image Velocimetry (PIV)[9] have shown the deformation to be uniformly distributed across the chip thickness. Thin surface layers (~10 µm thick, see Figure 2-4(a) on the right hand size of the cross section, separated by a dotted line) on both faces of the chip are, however, affected by secondary deformation arising from tool-chip friction. The uniform distribution of strain is consistent with observed uniformity of the hardness through the chip volume. Additional support for homogeneity of the deformation comes from electron backscattered diffraction (EBSD) investigations that have revealed a uniform microstructure through the foil thickness [2-21].

In this investigation, we used an electron beam channeling contrast imaging technique to examine the plastic deformation induced by the LSEM process from precipitation harden Inconel 718 alloy at the microscopic level. Figure 2-4(a) shows the electron beam channeling image of a cross section of finely polished LSEM foils and Figure 2-4(b) shows a TEM micrograph from the secondary deformation region (immediately adjacent to the cutting tool) sliced by focused ion beam technique. The arrow direction shows the rolling direction during the machining. TEM results indicate that the secondary deformation area is truly nanocrystalline i.e., average grain size less than 100 nm with fine carbides (majority are the niobium rich carbides as determined by EDS technique) uniformly dispersed within the microstructure. Electron beam channeling reveals an elongated microstructure in Figure 2-4(a) which is consistent with TEM observation in the bulk LSEM foil (see next section). The aligned carbides and the elongated microstructure in the electron beam channeling image reveal the curved plastic deformation flow lines (or flow plane for simple shear) in front of the secondary deformation area at the cutting tool edges (dotted lines for guiding the eyes only). Microstructural observations indicate that during the SPD process, titanium carbides, mostly in a cubic shape, remain coherent to the Inconel matrix (as shown by the dark particles in Figure 2-5(a)), while the niobium rich carbides (white particles in the image in Figure 2-5(b)) tend to crack and sometimes turn into smaller particles that elongate along the plastic deformation direction, leaving microscopic defects in the materials. These defects play an important role on final failure during tensile test.

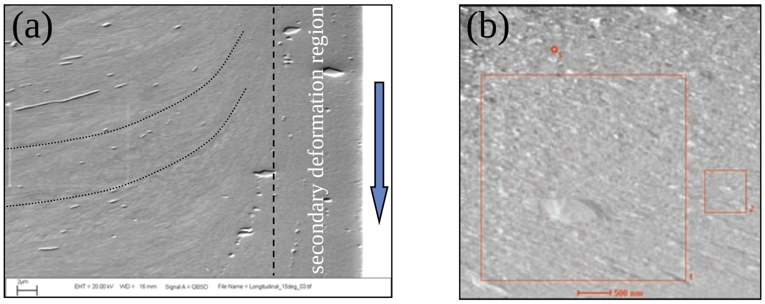

Figure 2-4 Microstructure of a Severely Plastic Deformed Precipitation Hardened Inconel 718 After LSEM. The Micrograph (a) of a Cross Section of Deformed Foils Along the Rolling Direction (Shown By Arrow), and (b) TEM Image of the Secondary Deformation Area.

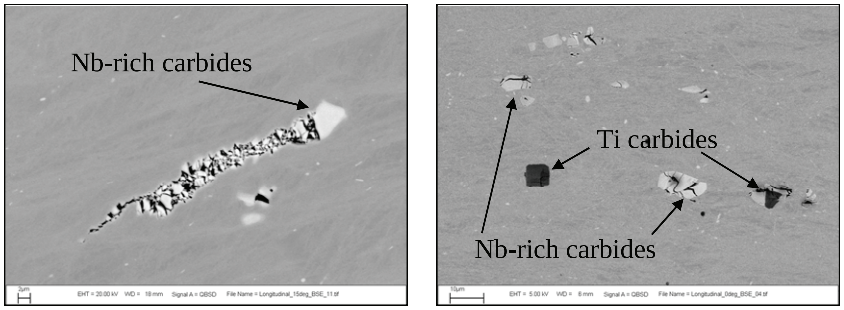

Figure 2-5 Plastic Deformation Around Precipitated Carbides. Black Titanium Carbides Retain Their Integrity While the Large Nb Rich Carbides (white) Tend to Crack or Deform Along the Plastic Deformation Direction.

2.5.3 Shear Strain and Microstructure Refinement

Direct evidence for ultrafine microstructures of the foils is seen in the TEM images and selected-area diffraction (SAD) patterns shown in Figure 2-6 to Figure 2-9, with shear strains from 1.5 to 3.9. The micrographs illustrate increased microstructure refinement and formation of nano-scale and UFG structures with increasing strain, which is consistent with the well-known dependence of microstructure on strain. At lower shear strains (1.5 and 2.3), the appearance of elongated microstructural features is evident. Diffraction patterns that indicate the presence of operating reflections in the crystal lattice are observed. The elongated nature of these structures, as well as the details in the diffraction patterns, suggest that these features are deformation twins in the Inconel. This will be verified later with the indexing of the diffraction patterns of these structures.

Figure 2-6 and Figure 2-7 show the bright and dark field TEM images of LSEM foil with shear strain of ~1.5 and ~2.3, respectively. Many regions show elongated features resembling twinned structures. Diffraction patterns of these areas indicate operating reflections in the lattice, which could be indicative of twinning. Other regions show dense accumulation of dislocations. Deformation twinning is the more dominant mode of deformation in certain material systems at higher strain rates and lower strains and has been observed to occur in Inconel 718 in the literature. Deformation twins are lower energy grain boundaries and may play a role in enhanced ductility and thermal stability.

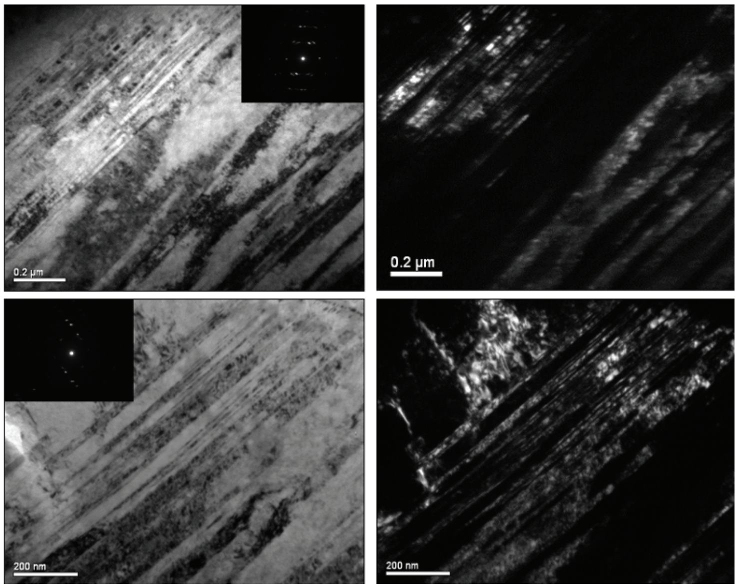

Figure 2-6 Bright-Field (left) and Dark-Field (right) TEM Micrographs of Inconel 718 Foils Created with Shear Strain of ~1.5, Showing the Nano-Size Microstructure.

As the shear strain increases, these elongated structures are no longer evident as twinning is presumed to no longer be the prevalent mode of deformation. Figure 2-8 and Figure 2-9 depict the microstructure changes in the LSEM Inconel 718 as the shear strain increases up to ~2.7 and ~3.9. Both figures show the absence of the elongated structures. The microstructure evolves from one characterized by dense areas of dislocations to one with sub-500 nm grain sizes. With increasing strain, the diffraction patterns also transform from a smeared single crystal pattern to one that is more ring-like and indicative of high angle misorientation between grains. This has also been confirmed by sample-tilting experiments in the electron microscope.

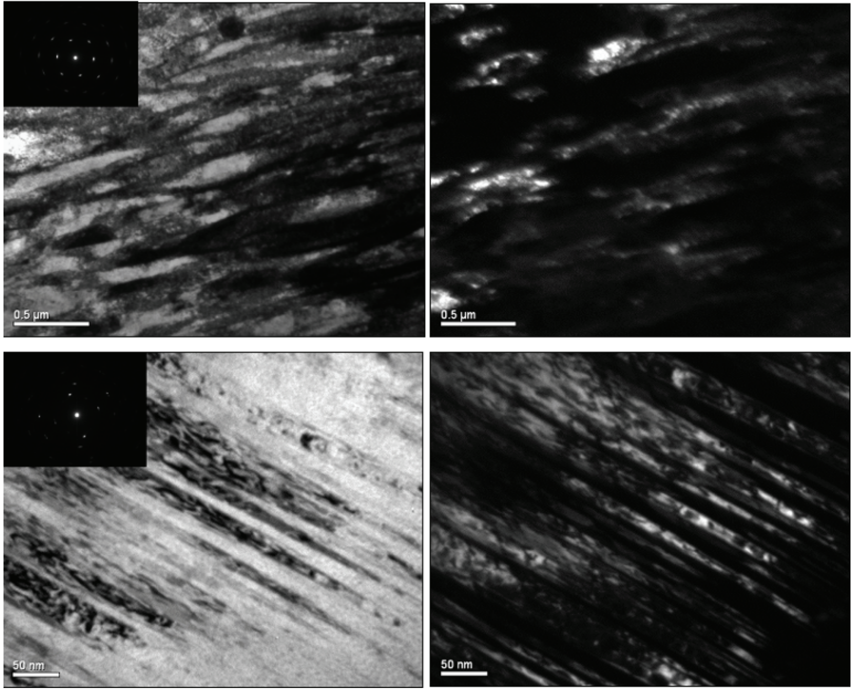

Figure 2-7 Bright-Field (left) and Dark-Field (right) TEM Micrographs of Inconel 718 Foils Created with Shear Strain of ~2.3 Showing the Nano-Size Microstructure

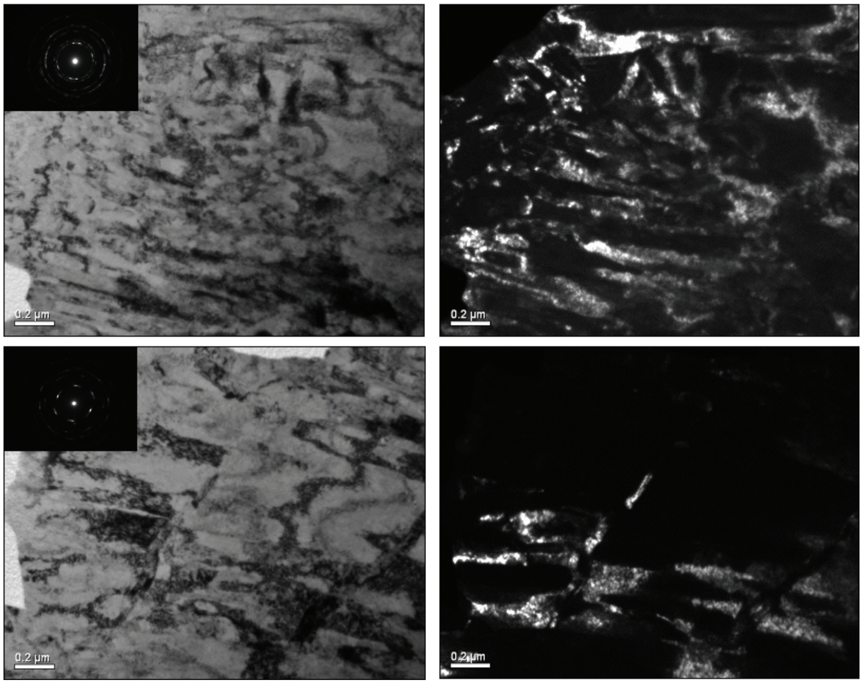

Figure 2-8 Bright-Field (left) and Dark-Field (right) TEM Micrographs of Inconel 718 Foils Created with Shear Strain of ~2.7 Showing the Nano-Size Microstructure.

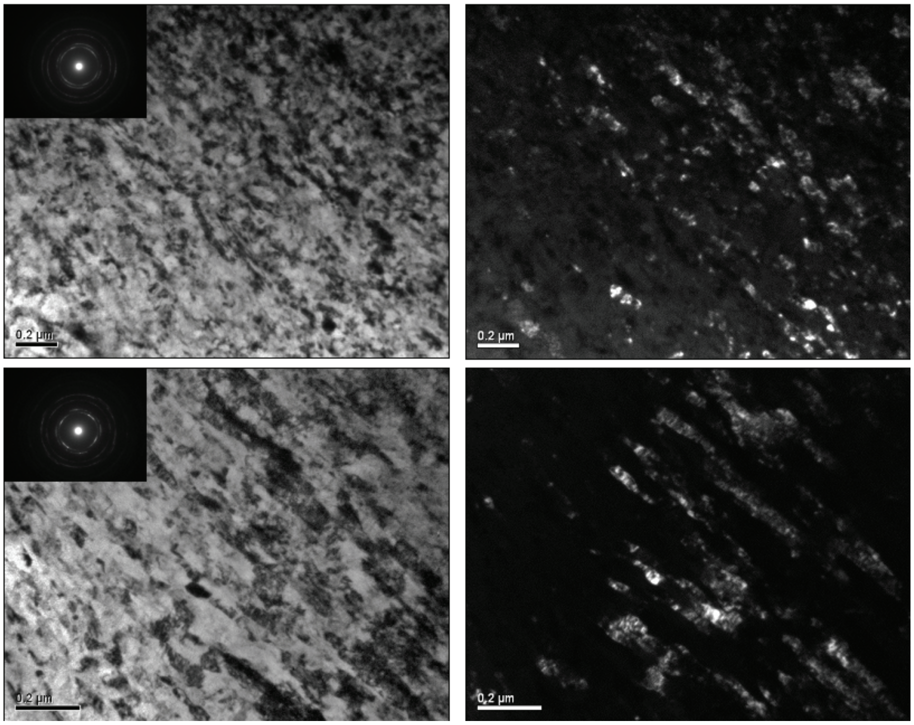

Figure 2-9 Bright-Field (left) and Dark-Field (right) TEM Micrographs of Inconel 718 Foils Created with Shear Strain of ~3.9 Showing the Nano-Size Microstructure.

2.5.4 Shear Strain versus Mechanical Properties

The stress-strain responses for LSEM Inconel 718 samples are given in Figure 2-10. Mini-tensile specimens fabricated from a bulk precipitation hardened (ppt) Inconel 718 alloy were also tested (green curve) for comparison purposes. Yield stress is determined at 0.2% engineering strain on the stress-strain curve. Results show that there is a significant increase in yield strength for the LSEM specimens. A 50% increase in the yield strength for a precipitation hardened LSEM sample (strain ~ 3.1) was observed in comparison to the microcrystalline bulk material; however, the maximum strain to failure (ε_f) was also significantly reduced (from 13% to below 2%). For solution treated (ST) samples, both yield strength (σ_{ys}) and maximum strength (σ_{max}) increase with the amount of strain induced during the extrusion machining process, while the average strain to fail (based on 5 test specimens) decreases from 3.5% to 2.5% and eventually to 1.4% as the strain values in LSEM process increased from 1.5, 2.7 to 3.9. When the maximum strain to failure exceeds 2%, necking at gauge region is readily observed, suggesting ductile deformation is dominant before failure. A 2% of strain before failure might not be suitable for large structure applications; however, it could be adequate to provide a sufficient reliability for meso-scale components. Data indicate that strengthening is more effective in the precipitation hardened samples than these solution treated specimens; however, the amount of ductility will be forfeited. Therefore, there is a moderate trade-off between strength and ductility, either by machining conditions or initial microstructure.

Elastic moduli estimated from the slope of the stress-strain curve ($d\sigma/d\varepsilon$) show that these LSEM samples have a lower modulus in comparison to the bulk materials. The observation is consistent with nano identation measurements. However, the estimated modulus increases with the shear strain induced by the LSEM process, which contradict the indentation results. It is plausible that errors in estimating the slope of the stress-strain curve were introduced since these samples are all slightly warped after extrusion machining. In parallel, we suggest to continue future investigation on this subject to obtain a better understanding of this issue.

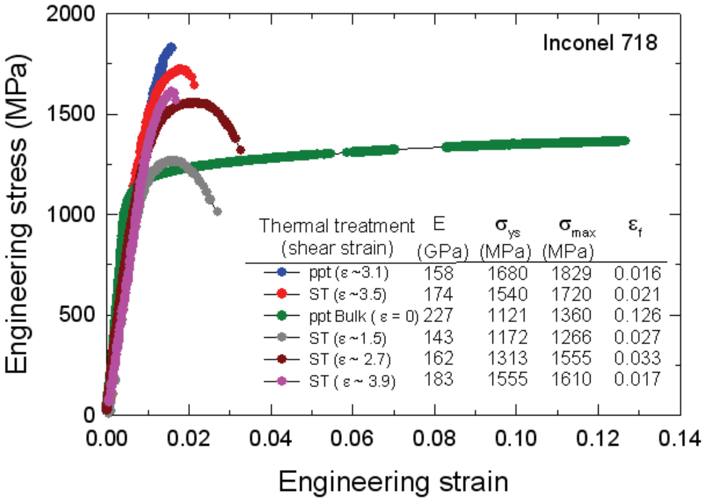

Figure 2-10 The Stress Strain Behavior of Extrusion Machined Inconel 718.

Microstructure of the fracture surface for precipitation hardened, extrusion machined specimens was examined because of the dramatic increase in its yield strength and the significant loss in its ductility. Fracture surface were examined by SEM. A typical fracture surface obtained by SEM for these specimens is given in Figure 2-11. The fracture surface exhibits regions with ductile and brittle failure morphologies. The dimpled rupture on the top is characteristic of a ductile failure; while the bottom region with many brittle cracks associated with niobium-rich carbides (determined by electron microprobe analysis) shows evidence of a brittle fracture. Observation suggests that fracture might be initiated from these large cracked niobium rich carbides (see Figure 2-5) during the extrusion machining process. Upon pulling under a tensile stress, cracks can quickly propagate through the sample as the material reaches its yield point, therefore contributing to the shorter elongations observed in these specimens

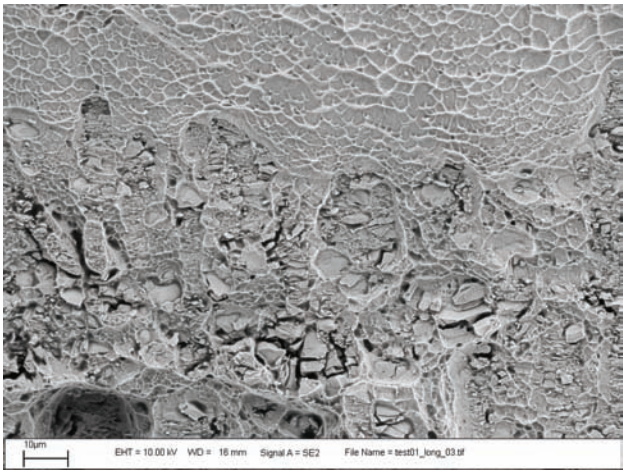

Figure 2-11 Microstructure of the Facture Surface for a Precipitation Hardened, Extrusion Machined Inconel 718 Alloy. The Top Portion Exhibits a Dimpled Rupture and the Bottom Shows Brittle Fracture from Cracked Carbides ($\gamma = 3.1$).

2.5.5 Thermal Stability of Extrusion Machined Inconel 718 Alloy

The thermal stability of precipitation-hardenable alloys such as Inconel 718 is largely determined by the stability of the precipitate phase [2-22]. This is even more important for metals with a nano-scale matrix, as the precipitates serve to pin grain boundary motion, hindering coarsening and softening of the fine-grained material. An aging study was conducted to investigate the precipitation kinetics (precipitate formation and ripening) in the microstructure (or grain size) refined Inconel 718 by LSEM process. The thermal aging study will help to determine the feasibility of the use of nanostructured Inconel 718 in micro-component applications at elevated temperature (i.e. > 650°C).

The original plan was to study the kinetics of the precipitation process of extrusion machined Inconel at different strain conditions [2-23] by SEM, TEM, x-ray diffraction [2-24, 2-25] (phase volume fraction, precipitate phases (γ', γ", and δ) [2-26], and their lattice parameters), and differential scanning calorimetry [2-27] (DSC). Results will be compared to the tensile testing data and microhardness measurements. Follow-up will also include a precipitation strengthening study to investigate the effect of over-ageing (OA) and peak-ageing (PA) on the strength, ductility and thermal stability of Inconel 718. The correlation of hardness data with the data from DSC and XRD testing will provide a good foundation for understanding precipitation kinetics and thermal stability, while the tensile data will give insight into ductility of nanostructured Inconel 718. However, due to the time constraint, only the microhardness experiment was completed and will be reported here.

The hardness evolution at 680 °C for bulk and extrusion machined Inconel 718 is given in Figure 2-12. Results show that the time required for peak aging of the nanostructured Inconel is much quicker than in the bulk material. The bulk material peak hardens to a value of about 4.73 GPa after aging at 200 hours. A peak in hardness (6.24 GPa) is seen after a treatment of 5 hours for a shear strain of 3.9. With longer exposure up to 300 hours at 680 °C, the strength of the highly nanostructured Inconel is seen to be stable at ~ 5.85 GPa. As the shear strain during the extrusion machining is reduced, the peak hardness falls and the time to peak hardness increases, as illustrated by sample with $\gamma = 1.5$.

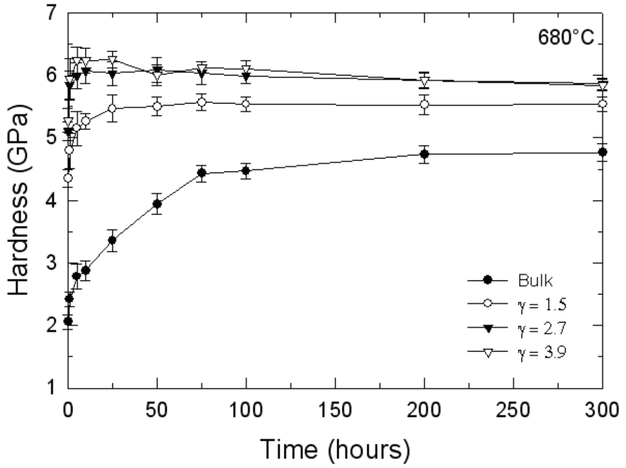

Figure 2-12 Hardness Evolution for Solution Treated Inconel 718 at 690˚C (Melting Point = 1300˚C).

The level of strengthening seen in the bulk material and nanostructured materials is consistent with the formation of γ' and coherent γ" precipitates in the matrix [2-26]. The primary mode of strengthening in Inconel 718 is the γ" precipitate. Softening of Inconel 718 has been shown to correspond to the transformation of the second phase from γ" to the δ phase, this does not appear to be the case for the range of conditions tested here due to the lower temperature.

Of particular interest is the stability of the nanostructured Inconel 718 with extended time at 680C, which is greater than half the melting point of alloy (T_m ~ 1300 °C). Materials with grain sizes in the nanometer regime typically suffer from low thermal stability, with re-crystallization and grain coarsening occurring at temperatures as low as 0.3 to 0.4 T_m. These preliminary results are promising in this regard, suggesting extrusion machined Inconel alloys might have a great potential for high temperature applications.

The aging curves for 750C are markedly different than those at 680C (see Figure 2-13). The time to peak hardness for the bulk material is much quicker in this case (in comparison to 680 °C) and the peak hardness of the high strain samples is quickly lost with time at this temperature. The bulk material also begins to lose strength with treatment beyond 100 hours, exhibiting a similar softening trend to that of the nanostructured material. One observation to note is that the extrusion machined materials are able to retain about 10% higher strength than the bulk up to 300 hours.

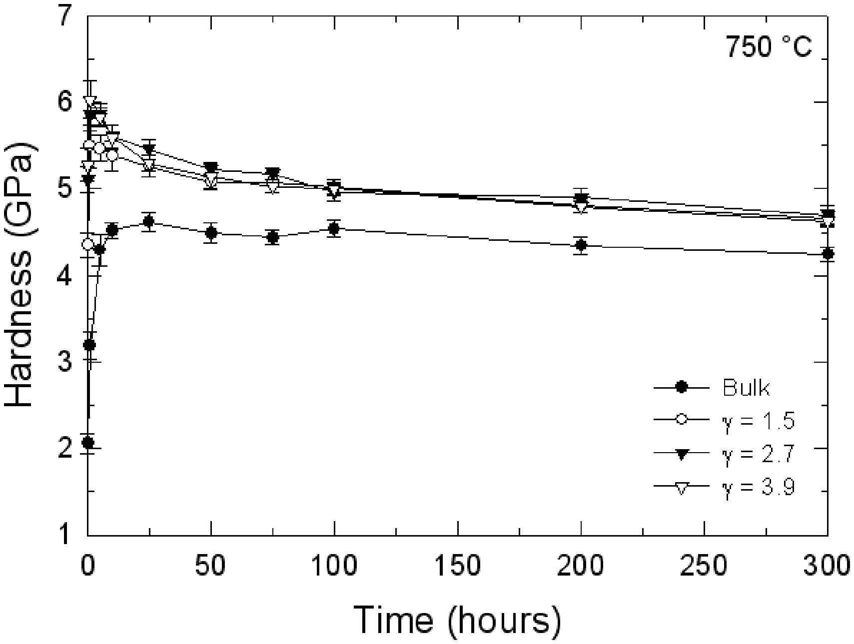

Figure 2-13 Hardness Evolution for Solution Treated Inconel 718 at 750˚C (Melting Point = 1300˚C)

The level of strengthening seen in the bulk material is once again consistent with the formation of γ' and coherent γ" precipitates in the matrix [2-26]. The softening of the undeformed bulk and the extrusion machined materials suggests the loss of thermal stability of the γ" precipitate phase in both the microcrystalline bulk and the nanostructured Inconel in this time/temperature regime.

The decreasing hardness for the nanostructured Inconel 718 samples with time, therefore, could be attributed to the ripening of the γ” phase or the fast transformation of the γ” to the δ phase at this temperature. Further characterization of the precipitate phases by high-resolution TEM in the future will shed light on these ideas. Nevertheless, these results indicate that the nanostructured Inconel is able to maintain strength improvement over the bulk material and exhibit a higher hardness value.

2.5.6 Prototype Meso-Scale Component Fabrication

Production of small components from the nanostructured Inconel foils was carried out using micro-EDM. These foils were extrusion machined from a precipitation hardened Inconel 718. Prior to the micro-machining, about 10-20 μm of material was taken off from each of the two extended foil surfaces by mechanical polishing to remove layers deformed by the tool faces. Micro-EDM produced a rough surface finish with ~ 1 μm thick recast layer (see Figure 2-14). The recast layer has a coarser grain structure with residual tungsten (from the wire used in the EDM machine) and complex oxides on the surface (Nb-Cr-Ti-Al-O, determined by EDX), presumably due to oxidation in the electro-discharge process. Figure 2-15 shows an SEM picture of micro-scale gears created by micro-EDM and electro-polishing. Measurements showed the form accuracy and tolerances to be excellent and the surface finish (Ra) value on the gear teeth to be ~0.1 μm. The high-aspect ratio features associated with the gear teeth are sharply demarcated in the picture, demonstrating the capability of micro-EDM to create a complex micro-scale part from pre-cursor nanostructured materials. Electron microscopy of the gear surfaces showed an almost complete absence of recast layers (see insert in Figure 2-15). However, white niobium-rich carbides can still be observed on the surface. The absence of the recast layers is undoubtedly a consequence of the low discharge energies used to effect material removal. Thus, the nano-scale microstructure of the Inconel foil, with its enhanced mechanical properties, is retained in the gear.

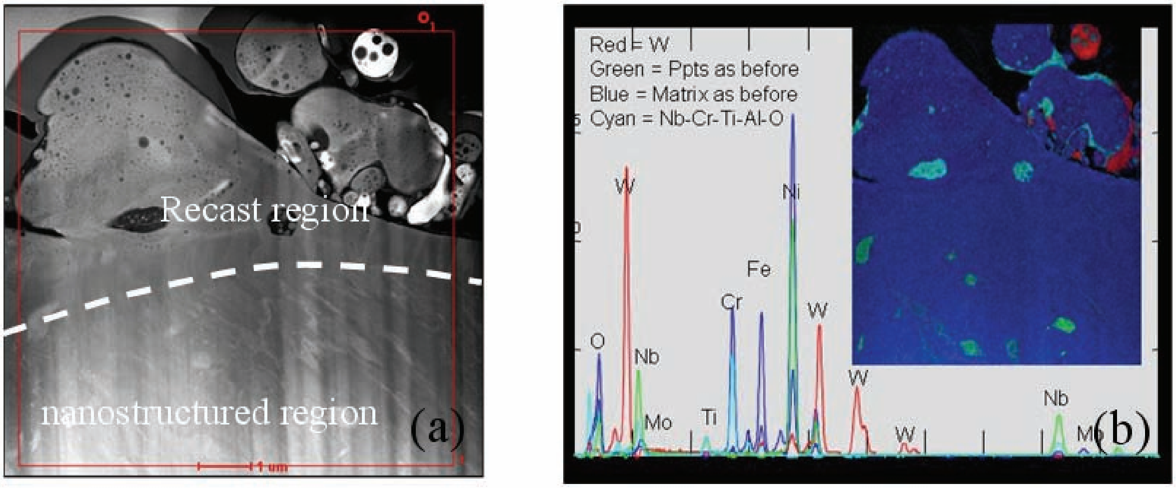

Figure 2-14 TEM Micrgraph of the Micro-EDM Surface of an Inconel Component(a), and the EDX Analysis of the Recast Region (γ=3.1).

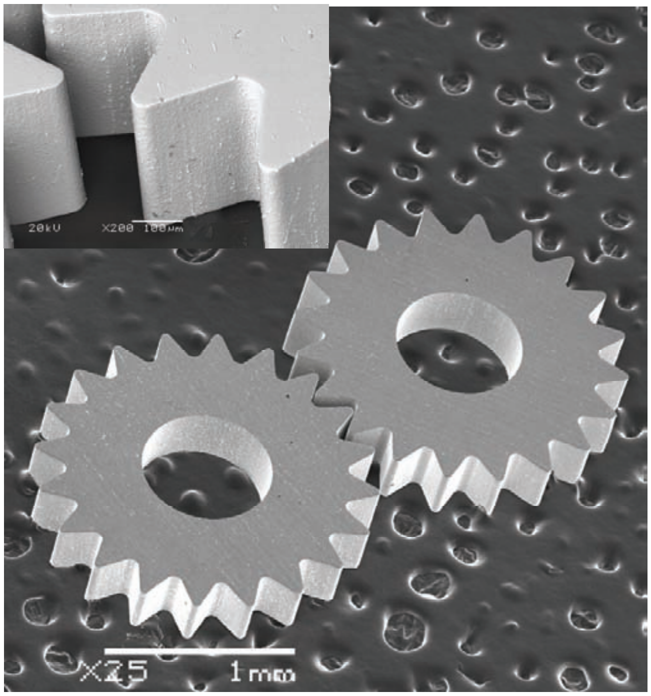

Figure 2-15 Meso-Scale Gears Produced by Micro-EDM and Electro-Polishing of Precipitation Hardened Inconel Foil (γ=3.1).

The combined LSEM/micro-machining approach offers exciting opportunities for creation of a new-class of small-scale components with enhanced structural performance. This manufacturing approach is flexible and applicable to a variety of high-strength nanostructured material systems such as titanium alloys and stainless steels. The nanostructured alloys created by LSEM can serve as pre-cursor materials for conventional micro-machining or micro-forming processes. This offers, potentially, a new paradigm for micro-systems manufacturing that incorporates nano-scale microstructure control. Ongoing work is aimed at developing this manufacturing framework for a broader class of nanostructured alloys and micro-scale components.

2.6 Conclusions for Large Strain Extrusion Machining

LSEM has been used to create foils of Inconel 718 with nano-scale microstructure. The nanostructuring is a consequence of the large plastic strains imposed in the Inconel 718 by SPD. Although the LSEM is a relatively low cost manufacturing process to fabricate nanostructured precursor materials for meso-scale components, small warp and residual stress could be an issue in fabrication of high precision components. The evolution of the microstructure with increasing shear strain is evident from TEM study. At low shear strain, the appearance of elongated microstructural features, as well as the details in the diffraction patterns, suggest that these features are deformation twins in the Inconel, presumably due to lower energy grain boundaries which may play a role in enhanced ductility. As the shear strain increases, these elongated structures disappear and are replaced by dense areas of dislocation to one with sub-500 nm grain sizes and high angle misorientation between grains becomes evident. These microstructural changes are reflected by the increased hardness and yield strength, as well as by reduced elongation during tensile testing. Fracture surface exhibits regions with both ductile and brittle failure morphologies. Microhardness evolution with thermal aging at 680°C shows that the time required for peak aging of the nanostructured Inconel is much quicker than in the bulk material.

With longer exposure up to 300 hours at 680 °C, the strength of the highly nanostructured Inconel is seen to be stable at ~ 5.85 GPa, which is 23.6% higher than the bulk microcrystalline material. The peak hardness slightly decreases for bulk and highly strained Inconel after thermal aging at 750°C for100 hours. However, the extrusion machined materials are able to retain about 10% higher strength than the bulk up to the 300 hours. Prototype 3-D micro-scale components from the nanostructured Inconel foils have been demonstrated using micro-EDM and electropolishing. This approach is applicable to a range of alloys and micro-machining processes.

2.7 Acknowledgements for Large Strain Extrusion Machining

This work was supported in part by an NSF Graduate Fellowship (to Christopher Saldana at Purdue University.). The majority of the funding and work are support by Sandia’s LDRD program. We are grateful to Professor S. Chandrasekar and C. Saldana (both from Purdue University) for their work on extrusion cutting, TEM, and thermal aging characterizations, Michael Saavedra for assistance with micro-EDM, Gilbert Benavides for encouraging development of this micro-scale manufacturing approach, David Schmale and Thomas Buchheit for mini-tensile test evaluations, Michael Rye and Joseph Michael for electron beam channeling contrast imaging, Richard P. Grant for SEM study, and Paul G. Kotual for the TEM investigation.

3 FABRICATION OF NANOSTRUCTURED ALUMINUM 6061-T6 PARTICULATES BY MODULATION ASSISTED MACHINING

A major focus of the project was to utilize particles created by Modulation Assisted Machining (MAM) as a potentially inexpensive source of nanocrystalline materials. This work was done with project partners from Purdue University. Below is a paper yet to be submitted which details the project efforts toward the creation, analysis, and utilization of MAM particles. The paper is authored by Pin Yang, David Gill, Luke Brewer, Bonnie McKenzie, and Joseph Michael of Sandia National Laboratories, with co-authors Christopher Saldana and Srinivasan Chandrasekar of Purdue University's Center for Materials Processing and Tribology.

3.1 Abstract for Modulation Assisted Machining

This study investigated the feasibility of fabricating nanostructured particulates of aluminum 6061-T6 alloy by a low-cost, modulation assisted machining method. These particulates were used for low temperature consolidation processes, including cold spray and shockwave consolidation, to provide high-strength nanostructured materials in bulk forms for meso-scale component fabrication. Small particulates, less than 100 µm with controlled morphology, were produced by modulation assisted machining during turning. Particle size, morphology and distribution were studied by optical and scanning electron microscopy (SEM), as well as particle size analyzer. Microstructure of these particulates was analyzed by SEM, electron channeling contrast imaging, electron backscatter diffraction, and transmission electron microscopy.

3.2 Introduction for Modulation Assisted Machining

Despite all the extraordinary properties [3-1 – 3-3] of nanocrystalline metals reported in the literature for more than 20 years, the transition of these materials from laboratory curiosity to viable engineering materials has not yet been realized. To deliver the promised properties of nanostructured metals and unleash their full potential for military and commercial applications, two major obstacles including the development of an effective consolidation process and the cost [3-4] and availability of nanostructured materials have to be overcome. Recent advances show that chips generated from machining operations are nanocrystalline, and cost 1/100th of current production methods. In addition, a variety of nanocrystalline metals and alloys can be produced by this technique for specific engineering applications. We used cold spray and shockwave compaction as low temperature forming processes to consolidate these particulates and form bulk materials that can be machined into practical meso-scale components (such as gears and cams) without compromising their unique microstructure.

It has been known for some time now that the application of a superimposed, low frequency modulation to conventional machining processes can result in controlled "chip breakage". This observation has been exploited to develop a modulation assisted machining (MAM) method for producing micron-sized particulate, i.e. chip particles, of varied morphology and controlled size distribution. Furthermore, since machining imposes large plastic strains in chips it results in significant refinement of the microstructure[3-5, 3-6]. These particulates are expected to be nanostructured. This prediction has been directly supported by the high hardness and strength observed in chips created by large strain machining[3-7 – 3-10]. This strengthening mechanism is best illustrated in the pioneering work of Hall[3-11] and Petch[3-12] who showed the yield strength of metal varies as the inverse square root of the grain size. The present study seeks to exploit these observations by incorporating two aspects of MAM to create nanostructured particulates: (1) the ability to control the geometry and size of the particle and (2) the ability to impose severe plastic strains during machining that affect microstructure refinement. It is anticipated that microstructure, morphology, chip size and distribution of these MAM produced particulates can significantly affect packing efficiency and final density during low temperature consolidation processes, and will be the focus of this investigation. Special emphasis is placed on the microstructure of these machined chips as it has never been reported in the literature due to the complexity of sample preparation for transmission electron microscopy (TEM) study.

3.3 Background for Modulation Assisted Machining

Aluminum 6161-T6, a precipitation hardenable AL-Mg-Si alloy, was used for this study. This material has been strengthened by a heat treatment at 175°C for 8 hours (temper process, T6) after solution treatment and water quench. During the tempering process, precipitates such as β” (needles), β’ (rods or spheres), β (Mg_2Si), and FE-Mn-Cr-Si precipitates, homogeneously form from an oversaturated solid solution and strengthen the aluminum alloy. The strength of this alloy can be further increased by strain hardening. Imposing severe plastic strains during MAM would, therefore, refine the microstructure and strengthen the particulates, as evidenced by a 39.2% increase in the hardness in comparison to the stock material[3-13].

MAM in turning is used for production of micro-sized particulates using a conventional lathe machining configuration as shown in Figure 3-1. A sinusoidal modulation, $\Delta z(t)$, is superimposed in the feed direction (i.e., direction of undeformed chip thickness), which is perpendicular to the cutting velocity (v_c). Particulate production is possible via interrupted cutting of the workpiece at the fine-scale due to sinusoidal motion of the tool. The formation of this particulate via a direct cutting process capitalizes on the severe plastic deformation that causes microstructural refinement. This is advantageous due to the aforementioned enhancements in material characteristics seen in metals that have undergone severe plastic deformation. Thus, the capabilities of this technology include (1) the ability to directly control the size and shape of this particulate, (2) the ability to generate particulates in a wide variety of metals and alloys of varying mechanical properties, and (3) the ability to generate particulate with a fine grain size in the submicron regime, a consequence of severe plastic deformation imposed during the material removal process. These features enable alternative ways to make nanostructured bulk materials by low temperature consolidation processes. Unlike other severe plastic deformation routes, such as equal channel angular extrusion[3-14] and high pressure torsion[3-15], this approach can produced desirable microstructure without multiple passes, expensive tooling and inability to process materials of high initial strength without the use of elevated temperatures that may lead to coarsening of the microstructure.

In a turning MAM process, the tool is fed linearly into the rotating workpiece with the modulation superimposed. Particulates are created by the intersection of the successive machining passes on the workpiece. An example of this is depicted in Figure 3-1 as the intersection of passes *n* and *n-1*. Tool motion, which defines the morphology of the particulate created from the cutting process, is a function of modulation and machining parameters, which are summarized in Table 3-1.

Each parameter influences the final geometry of the particulate. Modulation frequency (f_m) and workpiece rotational frequency (f_w) determine the contact time of the tool with the workpiece and affect the resultant particulate length. This is evident, as increased workpiece rotation frequencies required increased modulation frequencies to create particles of equivalent length. Modulation amplitude (A) and feed rate (s_o) describe the axial position of the tool at any point of time, defining the thickness and cross-sectional shape of the resultant undeformed particulate. Similarly, increased feed rates require increased modulation amplitudes to ensure interrupted cutting and deformation of particulate. Any determination of particulate morphology must account for each of these variables. A two dimensional model of the process depicted in Figure 3-1 was developed[3-13] to quantitatively determine the particle's undeformed dimensions as a function of machining and modulation parameters. The geometric characteristics of the undeformed particulate (length, width and thickness) are determined from this model. Details of the mathematical modeling and the validation of the shape and morphology with respect to machining parameters were documented in Saldana's thesis[3-13]. The present work utilizes his code to fabricate aluminum 6061-T6 particulates with equiaxed, needle, and platelet shapes for low temperature consolidation processes.

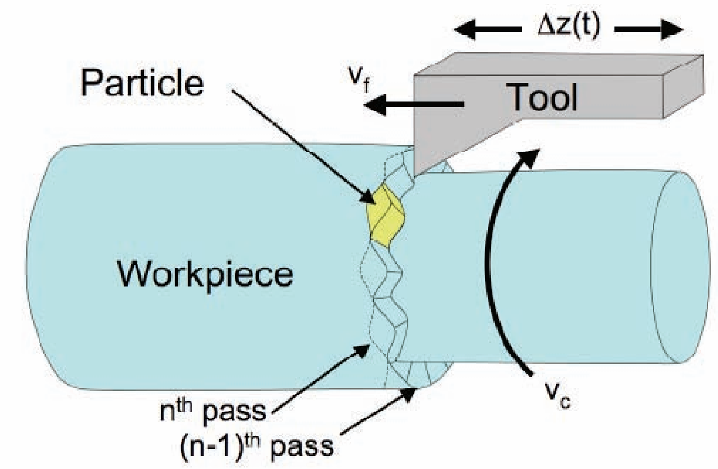

Figure 3-1 A Schematic Illustration of Modulation Assisted Machining for Particulate Production.

Table 3-1 Modulation Assisted Machining (MAM) Parameters.

Type	Parameter	Symbol	Units
Machining	Feed Rate	s_o	mm/rev
	Particle Width	w_o	mm
	Workpiece Rotational Frequency	f_w	RPM
	Workpiece Diameter	d	mm
Modulation	Amplitude	A	mm
	Modulation Frequency	f_m	Hz

3.4 Experimental Procedure for Modulation Assisted Machining

A three-axis computer numerical control lathe (Miyano, BNC-42CS) was used as the machining platform for this study. Particles were created using a carbide tool located in a tool holder retrofitted with modulation capabilities. The MAM tool holder (US Patent Pending #

60/667,247)[3-13] was mounted in the turret of the Miyano lathe. The cutting tool is fixed to a ball spline shaft, which is attached to a piezoelectric actuator. A waveform generator (Agilent 33220A) and signal amplifier (Physik Instrumente E-505) send electronic waveforms that drive the lead zirconate titanate linear actuator (Physik Instrumente 843.60), causing the cutting tool to displace position based on the motion of the actuator.

Aluminum 6061-T6 used in this experiment were 3 to 6 mm diameter round stock. The carbide tool used in the assembly had a rake angle of zero degrees, a clearance angle of 45 degrees, and edge radii of approximately 20 µm. The edge radii of the tools used in these experiments are of importance as preliminary experimental work has shown that as the edge radii values are approached with respect to particulate size, the accuracy of particulate creation becomes unpredictable. Thus, the geometrical characteristics of the tools employed in this process define the lower limit on the particulate size creation.

Continuous lubrication of the tool-chip interface is necessary in MAM. High-speed imagery of the tool-chip interface in particulate production has shown that under dry cutting conditions, particulates become bonded to each other, forming a chain of particles that resemble a serrated chip. Though the nature of the bonding mechanism has not been fully investigated, it is theorized that this phenomenon is a results of the friction present between the freshly cut particle surfaces. Experimental work has shown that isopropyl alcohol provides adequate wetting of the particulate surfaces to prevent unwanted agglomeration. Isopropyl alcohol also evaporates relatively quickly and helps to maintain the cleanliness of the particle surfaces, thus reducing any potential contamination.

The theoretical capabilities of the piezoelectric actuator and amplifier combination were considered in the experiments that were conducted. From the data provided by the manufacturer, the modulation system used in this study begins to loss the ability to achieve ‘instantaneous’ response at full amplitude for frequencies greater than 200 Hz.

Optical microscopy equipped with digital measurement system and scanning electron microscopy (SEM, JOEL) were used to directly observe the particulate size, shape, and distribution. Electron channeling contrast imaging was utilized to analyze the deformation and the morphology of the particulates produced by the MAM. TEM was employed to investigate the microstructural details of these machined particulates. The particulates under investigation were thinned using focused ion beam (FIB) techniques to thin the particulate to electron transparency.

3.5 Results and Discussion for Modulation Assisted Machining

3.5.1 Preliminary Evaluation of the MAM Process

A preliminary study in fabrication of micron-size aluminum 6061-T6 particulates with practical quantity at Sandia during the first year of this program led to the conclusion that MAM was extremely time consuming. This is particularly true for fabricating particulates with sizes less than 100 µm, which are most suitable for low temperature consolidation processes. The low output can be attributed to a low material removal rate for producing finer particulates during the machining process. As a result, particulates of different morphology used in the cold spray and shockwave consolidation evaluations were purchased from an outside vendor. Expenditure of these purchases indicates that current MAM technology in producing particulates is far less cost effective as most literature has predicted.

3.5.2 Controlling Particulate Size and Morphology by MAM

A preliminary evaluation of the MAM process in producing different morphology machining chips confirmed the mathematic modeling[3-13] in controlling the shape and size of particulates. Figure 3-2 demonstrates the different shapes of particulates created by the MAM process at Sandia and the respective machining and modulation parameters are given in Table 3-2. Optical images in Figure 3-2 suggest that the particulate size and shape are quite consistent with the model's prediction.

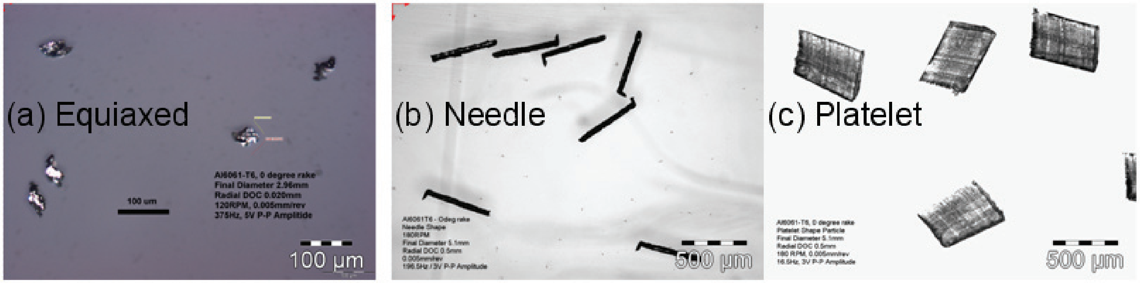

Figure 3-2 Optical Microscopy Images of Different Shape Particulates Created by MAM of Aluminum 6061-T6 Alloy (Machining and Modulation Parameters are Given in Table 3-2)

Table 3-2 Machining and Modulation Parameters for Particulate Fabrication (see Figure 3-2).

Parameter, Symbol	Units	Equiaxed	Needle	Platelet
Feed rate, s_o	mm/rev	0.005	0.005	0.005
Particle width, w_o	mm	0.02	0.50	0.50
Rotational frequency, f_w	RPM	120	180	180
Workpiece diameter, d	mm	2.96	5.10	5.10
A (Voltage to actuator)	V (peak-to peak)	5.0	3.0	3.0
Modulation frequency, f_m	Hz	375	16.5	196.5

The particulates used in the cold spray and the shockwave consolidation (see other parts of this SAND report) were purchased from a commercial source (M4 Sciences, West Lafayette, Indiana). The size and shape of the aluminum 6061-T6 particulate fabricated by MAM is shown in Figure 3-3, apparently these smaller size chips (< 100 µm) were made with a different set of MAM parameters. The equaxied particles are slightly elongated in the long axis (the average particle size is 63.6±23.55 µm), but the average size of each shape particulate, including needle and platelet shapes, are quite uniform. A dry, optical-based, particle size distribution analysis was performed for the equiaxed particulates and the result is given in Figure 3-4. The data indicates that the sizes of these machined chips varied from 20 to 110 µm, with a bimodal distribution where only a small fraction of powder (< 10 vol. %) is greater than 100 µm.

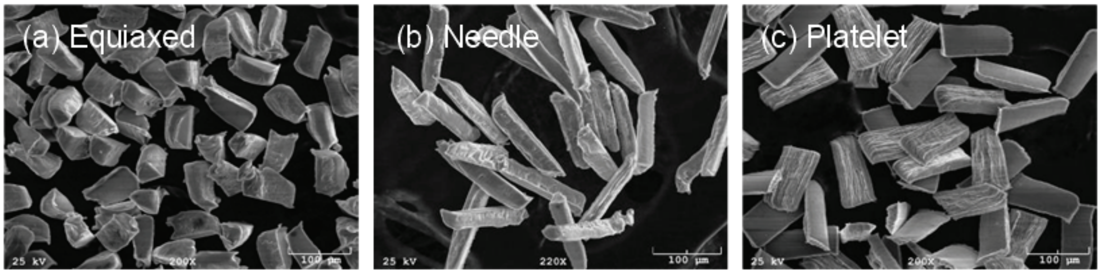

Figure 3-3 SEM Images of Commercial MAM Particulates Made for Aluminum 6061-T6 Alloy (M4 Sciences, West Lafayette, IN).

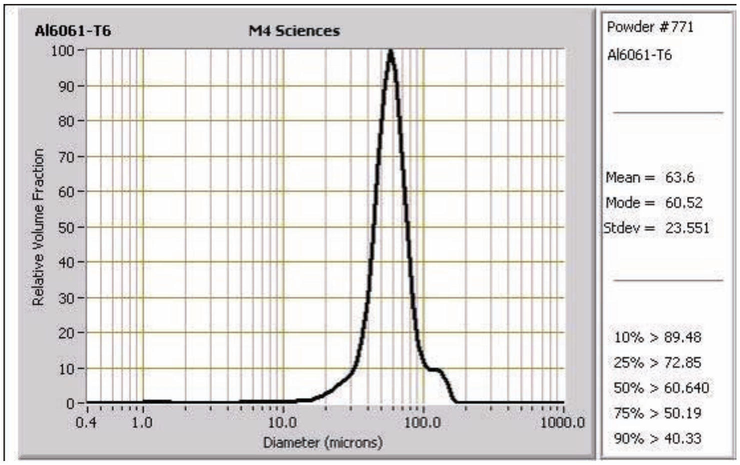

Figure 3-4 Particle Size Distribution of Equiaxed Particulates Produced by MAM Process (M4 Sciences, West Lafayette, IN).

3.5.3 Microstructure Study of MAM Particles

SEM, electron channeling contrast imaging, electron back scatter diffraction (EBSD), and TEM were used to characterize the microstructure of commercial MAM particulates. Special emphases were placed on the microstructure refinement induced by the MAM and the possibility of texture development induced by plastic deformation. For SEM, electron channeling contrast imaging and EBSD studies, particulates were uniformly dispersed on a glass slide and then placed in an epoxy filled mold. After the resin was cured, the sample was ground and polished so that particulates of different orientations could be studied. In this section, these microstructure characterization results will be presented and discussed, based on their particle morphology. Some cautions must be taken when interpreting these micrographs since these images were taken at different locations and orientations with respect to the chip forming process. However, some generalization can be concluded based on these microstructure investigations.

(a) <u>Equiaxed Particulate</u>

Figure 3-5 shows the electron channeling contrast images of equiaxed particulates fabricated by MAM. The channeling technique reveals the texture development induced by the plastic deformation (in terms of image contrasts due to the differences in the electron-material interactions at various crystal orientations) during the chip fabrication process. Figure 3-5(b) and (c) suggest that there is a significant difference in the plastic deformation near the edge (Figure 3-5(b)) and at the center of the particulate (Figure 3-5(c)). The center region seems to have an elongated, fibrous structure, while the edge has a much finer structure. Participates (white spots) are uniformly distributed in the microstructure and seems to follow the direction of plastic deformation. The interface between these silicon-rich precipitates (determined by EDS, not shown here) and the aluminum alloy matrix is intact. Pits or voids (dark spots), verified by both secondary electron and backscatter electron images, are mostly submicron in size, and can be observed throughout the machined chip. Small pits (<100 nm) are concentrated at edge region (see Figure 3-6), where the microstructure of this thin layer (< 2 µm) near the surface can be affected by the secondary deformation arising from tool-chip friction.

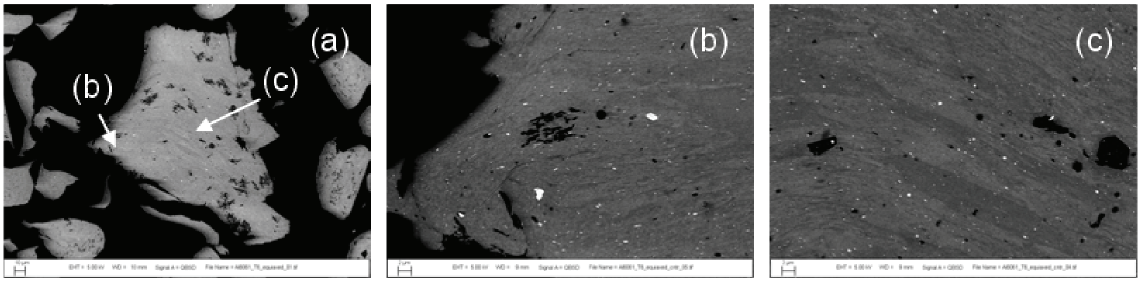

Figure 3-5 Micrographs Obtained by Electron Channeling Contrast Imaginig Technique for Equiaxed Aluminum 6061-T6 Particulates Fabricated By MAM (a) Image of a Machined Chip, (b) Image of the Edge of the Chip, and (c) Image At the Center of the Chip.

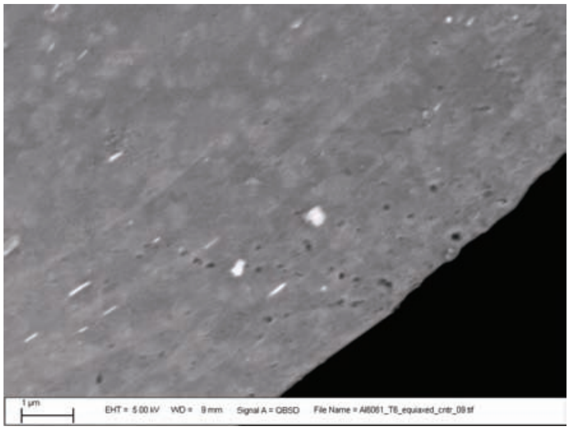

Figure 3-6 Electron Channeling Contrast Image Near the Edge of an Equiaxed Particulate Fabricated by MAM.

The observation of a different microstructure at the edge and the center of a machined chip prompted a detailed study by EBSD to map out the texture development induced by the plastic deformation, which in turn will help to discern the crystallite size and orientation for these two regions. Figure 3-7 illustrates the inverse pole figures of a MAM chip. The color figure in each image gives the orientation of the crystallite distribution with respect to sample axes (see the color of each pole in the aluminum slip systems). Results show that there is a strong gradient in grain size from the edge (ultra-fined grain microstructure i.e., 100-300 nm) to the center (fine grain with grain width close to 1 µm and length more than 3 µm) of the machined chip. In addition, there is no preferred orientation of crystallites in the edge region, while the grains in the center are highly textured (as seen in the Y and Z inverse pole figures). The black regions are where patterns could not be indexed and may be attributed to heavy dislocations bands.

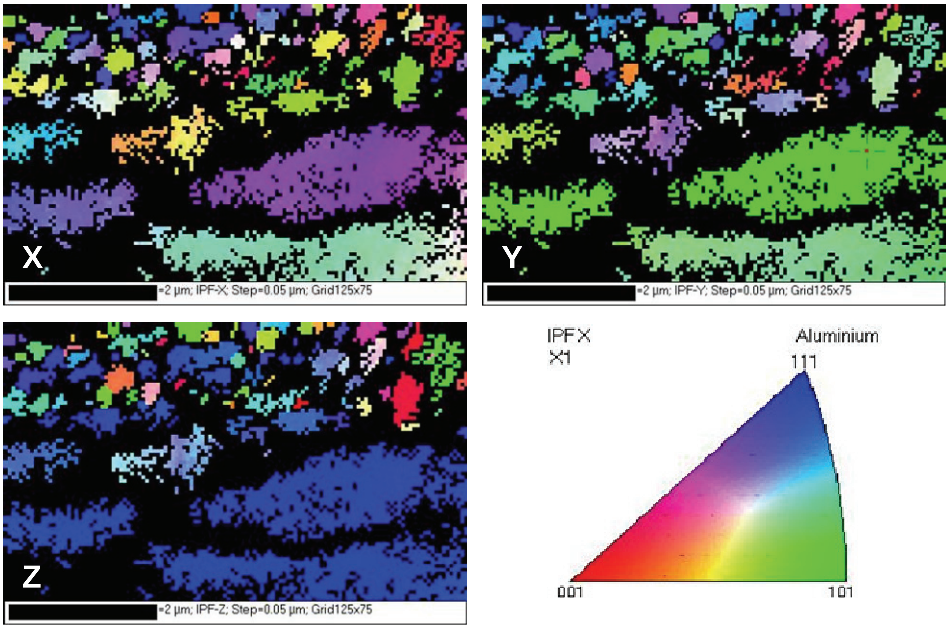

Figure 3-7 EBSD Inverse Pole Figures Shown with Respect To The Sample Axes of an Equiaxed Particulate Fabricated by MAM of Aluminum 6061-T6 Alloy. The Top Region of These Figures is Close to the Edge of a Machined Chip, While the Large Elongated Grains on the Bottom Are Near the Middle of the Machined Chip.

The graded microstructure was further investigated by TEM with a bright field (BF) and dark field (DF) image pair, using the {111} reflection (see Figure 3-8(a) and (b)). Results show there is an ultra-fine grained microstructure at the surface of the sample (or the edge of the machined chip) and large elongated grains with heavy dislocations bands at the bottom (center of the machined chip). This observation is consistent with EBSD analysis. The selected area diffraction (SAD) pattern collected at the large grained region shows spotty rings suggesting that the average grain size in this region is greater than 100 nm. The strong intensities in the {220} and {111} rings indicate there is a strong texture developed in the specimen. Furthermore, detailed study indicates that the fine crystallites near the surface are approximately equiaxed in shape and between 100 nm and 300 nm in size (see Figure 3-9).

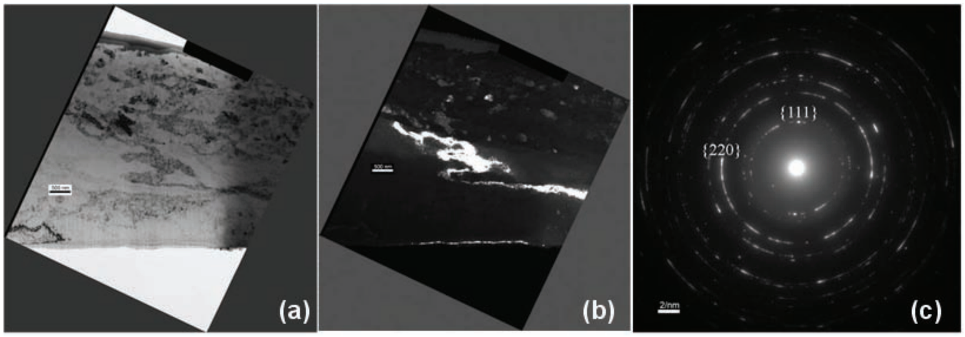

Figure 3-8 (a) The Bright Field and (b) Dark Field TEM Micrographs of an Equiaxed Particulate and (c) the SAD Pattern (Scale Bar = 500nm).

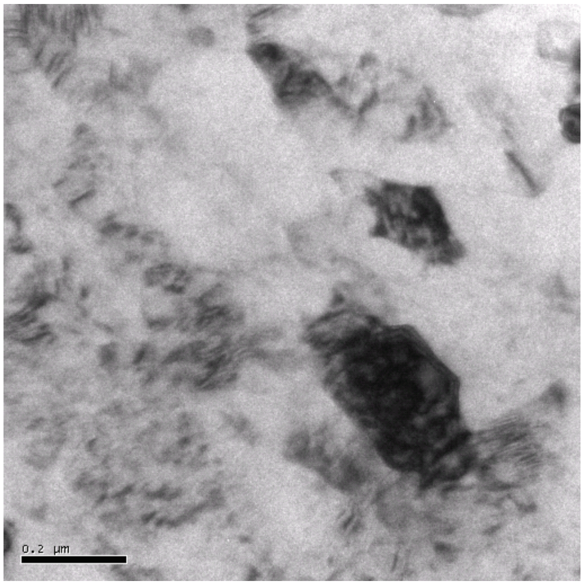

Figure 3-9 A Bright Field TEM Micrograph Near the Surface of an Equiaxed Particulate Illustrating an Ultra-Fine Grained Microstructure.

(b) Needle Particulate

The needle shape particulates were first studied by an electron channeling imaging technique. Figure 3-10 gives the microstructure of these particulates. Once again, the contrast shows a core-shell structure with a fine microstructure near the surface and coarse, elongated grains stretched along the long axis of the particulate. However the overall contrast is lower in comparison to the equiaxed particles. Voids tend to aggregate and align perpendicular to the long axis. Under a back scatter electron imaging condition where these images were taken, precipitates can be seen in white and well dispersed in the alloy matrix. The long axis of some precipitates (with a high aspect ratio) tends to align perpendicular to the long axis of the particulates, and more often voids can be found near to the precipitate (to the right). For small precipitates, the interface between precipitate and matrix remains coherent. These observations suggest that the region under investigation might be close to the secondary deformation region where friction between tool and chip could modify the structure and put a compressive stress along the long axis of the chip. As a result, voids were aligned perpendicular to the compressive stress direction and less texture induced contrast was detected.

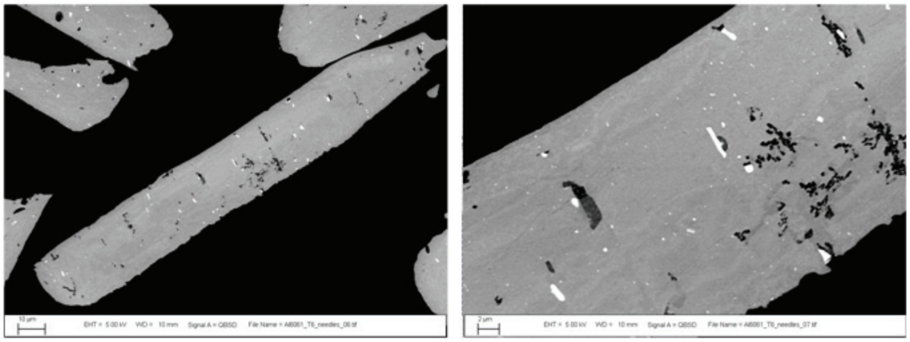

Figure 3-10 Electron Channeling Contrast Images of Needle Shape Particulates Produced by MAM.

TEM was used to study the microstructure of the needle shape particulates. This time a {200} reflection was used in comparison of the BF and DF images. Results of these images, together with the SAD pattern, are given in Figure 3-11. Similar to the equiaxed particulates, layers of ultra-fine grain microstructure was developed near the surface, and large grains with heavy dislocation bands were observed at the inner region of the particulate. The SAD collected at the inner region shows strong texture as indicated by the strong intensity of {200} and {220} rings. Note the texture induced in these needle shape particulate is different than that of equiaxed (C.1) and platelet (C.3) particulates. Microstructure near the surface reveals layers of grains with elongated aspect ratio (see Figure 3-12). The thickness of these layers is in the 100 nm to 200 nm range.

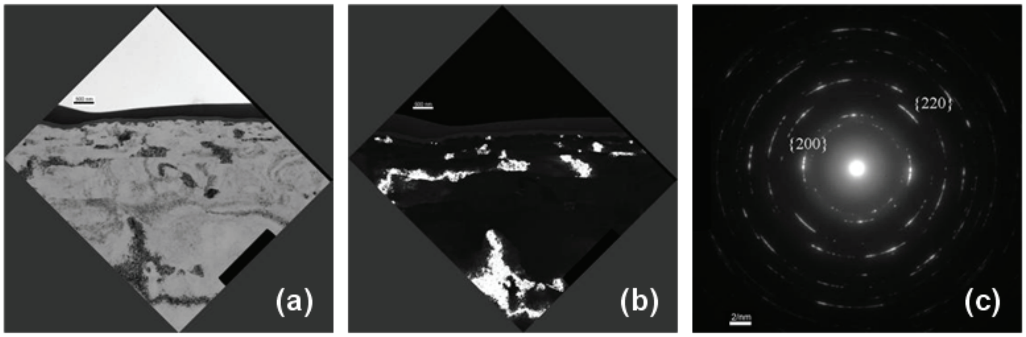

Figure 3-11 (a) The Bright Field and (b) The Dark Field TEM Micrographs of a Needle Shape Particulate, As Well As (c) The SAD Pattern (Scale Bar = 500nm).

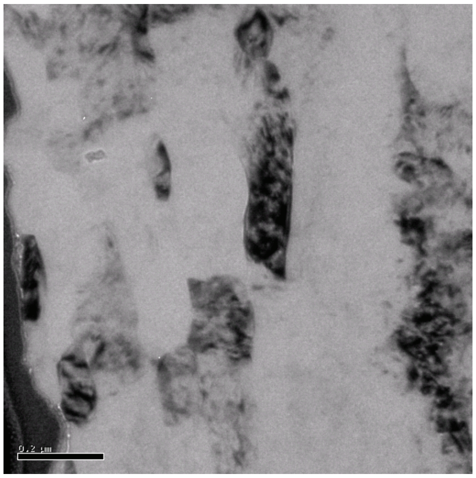

Figure 3-12 TEM Micrograph Near the Surface of a MAM Needle Shape Particulate.

(c) Platelet Particulate

Electron channeling contrast images of platelet particulates are given in Figure 3-13. Similar to the equiaxed and needle shape particulates, these micrographs show there is an ultra-fine grained microstructure near the edge while 2 to 3 µm away from the edge an elongated, fibrous structure is found in the particulate. Voids and precipitates are uniformly distributed in these machined chips. For the most part, the interface between precipitate and matrix remains coherent, and high aspect ratio precipitates are randomly oriented.

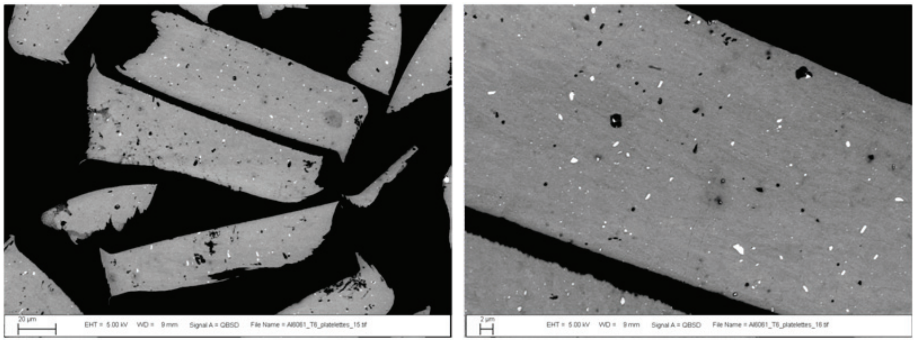

Figure 3-13 Electron Channeling Contrast Images of Platelet Particles Prepared by MAM.

The bright field and the dark field TEM micrographs, as well as the SAD pattern for a platelet particulate is given in Figure 3-14. The SAD pattern was obtained at the bottom region (see bright field image) where large grains with heavy dislocations bands were observed. The SAD pattern shows stronger intensities of {111} and {220} rings, indicating that this region is highly textured. The TEM image (see Figure 3-15) reveals that there are layers of highly elongated grains (layer thickness between 50 to 200 nm) near the surface. The morphology of these grains is quite similar to the needle shape particle.

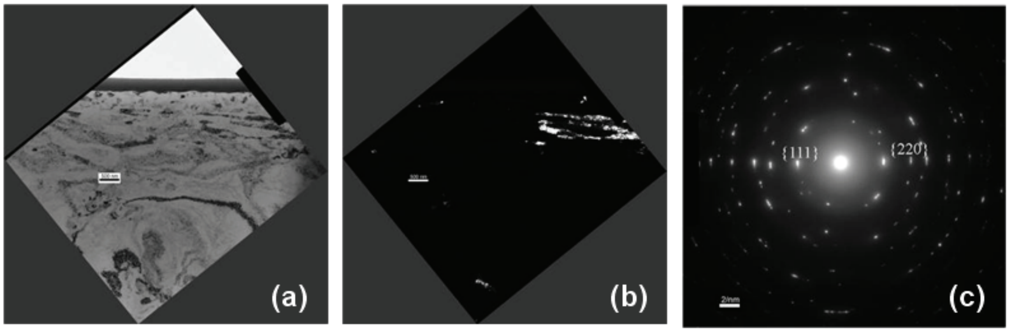

Figure 3-14 TEM Micrographs and the SAD Pattern of a Platelet Particle Created by MAM (Scale Bar = 500nm).

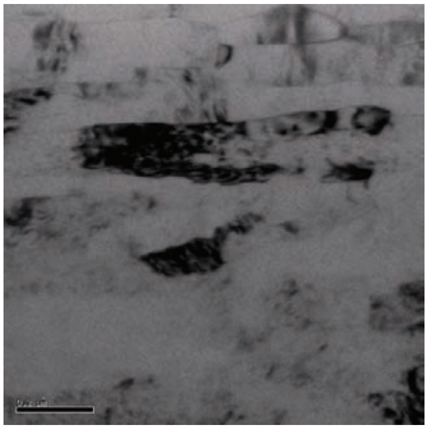

Figure 3-15 TEM Micrograph Near the Surface of an Aluminum 6061-T6 Platelet Particle Prepared by MAM (Scale Bar = 200nm).

3.6 Conclusions for Modulation Assisted Machining

This work demonstrates that modulation-assisted machining is effective to produce micron-sized particulates with tightly controlled morphology and size from aluminum 6061-T6 alloys. The resulting particulates exhibit a core-shell microstructure with ultra-fined grains at the surface (100-300 nm) and coarser, elongated grains (~1 to 2 µm in width and 4 to 6 µm in length) at ~2 micron inside the particulate surface. These coarser grains show characteristics of texture and heavy dislocations bands, indicating a lesser degree of strain induced microstructure refinement. Therefore, it is expected that the surface layer will be harder, while the inner region will be soft and can accommodate more plastic deformation. This unique microstructure can play an important role on cold consolidation processes and affect their final mechanical performance.

3.7 Acknowledgements for Modulation Assisted Machining

This work was supported in part by an NSF Graduate Fellowship (to Christopher Saldana at Purdue University.). The Majority of the funding and work are support by Sandia’s LDRD program. We are grateful to Professor S. Chandrasekar and C. Saldana (both from Purdue University) for their work on MAM, George R. Burns and Michael Saavedra for their assistance for equipment set-up and testing , Gilbert Benavides for encouraging development of this micro-scale manufacturing approach, and Michael Rye for the FIB sample preparation.

4 PREPARATION OF ALUMINUM COATINGS CONTAINING HOMOGENOUS NANOCRYSTALLINE MICROSTRUCTURES USING THE COLD SPRAY PROCESS

The thermal spray process has proven to be a successful means of not only creating bulk nanocrystalline material, but of also further refining the grain size during the high velocity impact cold working that occurs during the process. This section consists of a peer reviewed paper selected for publication by the Journal of Thermal Spray Technology. The paper’s authors are Aaron C. Hall and Luke N. Brewer of Sandia National Laboratories and Timothy J. Roemer of Ktech.

4.1 Abstract for Cold Spray

Nanostructured materials are of widespread interest because of the unique properties they offer. Well proven techniques, such as ball milling, exist for preparing powders with nanocrystalline microstructures. Nevertheless, consolidation of nanocrystalline powders is challenging and presents an obstacle to the use of nanocrystalline metals. This work demonstrates that nanocrystalline aluminum powders can be consolidated using the cold spray process. Furthermore, TEM analysis of the nanocrystalline cold spray coatings reveals that the cold spray process can cause significant grain refinement. Inert gas atomized 6061 and 5083 aluminum powders were ball milled in liquid nitrogen resulting in micron sized powder containing 250-400 nm grains. Cold spray coatings prepared using these feed stock materials exhibited homogenous microstructures with grain sizes of 30-50 nm. TEM images of the as-received powders, ball milled powders, and cold spray coatings are shown.

4.2 Introduction for Cold Spray

Nanostructured materials are of widespread interest to the scientific community because of the unique and unusual properties offered by these materials [4-1, 4-2]. The high grain boundary content of nanocrystalline materials results in grain boundary properties contributing significantly to the bulk material properties. Dislocation behavior in nanocrystals is different from larger crystals and can result in significant strengthening of nanocrystalline metals [4-3, 4-4].

Many techniques have been developed for preparing nanocrystals including inert gas condensation, precipitation from solution, ball milling, rapid solidification, and crystallization from amorphous phases [4-1, 4-2]. Many of these techniques result in free nanocrystals (precipitation and inert gas condensation) or in micron sized powders (ball milling) containing nanocrystalline microstructures. One of the most challenging problems associated with nanocrystalline materials is the consolidation of these small powders into larger shapes that can be used for practical applications [4-2]. This is a problem that Sandia National Laboratories is particularly interested in because of Sandia’s interest in the manufacture of meso-scale machinery. Meso-scale machines are miniature mechanical systems. Individual components in these systems may have part dimensions on the order of a few hundred microns. The gears pictured in Figure 4-1 were manufactured using traditional meso-scale machining [4-5, 4-6, 4-7] approaches not LIGA [4-8, 4-9] or MEMS techniques [4-10].

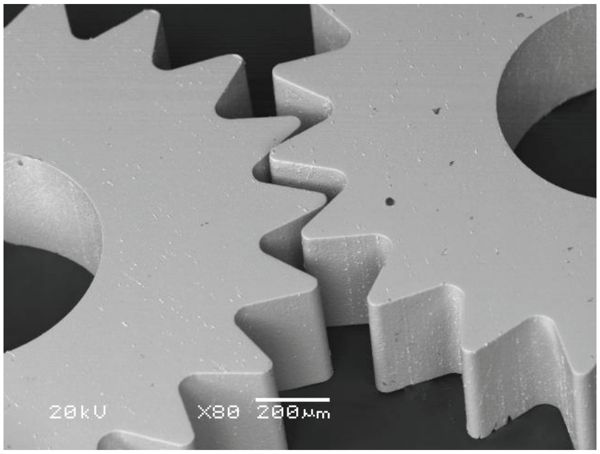

Figure 4-1 Example of a Meso-scale Mechanical Component. Fabrication of Meso-scale Mechanical Components Requires Extremely Fine Grained Materials; Otherwise Component Performance is Determined by Grain Boundary Locations and Crystal Orientations Within the Part.

A number of problems are encountered in mesoscale parts as part dimensions approach the grain size of the base material including unpredictable mechanical behavior and reduced component performance. These problems stem from the fact that as component dimensions approach the grain size of the base material, grain boundary properties and the orientation of individual grains dominate the mechanical behavior of the component. This problem can be solved by reducing the grain size in the base material.

One approach to preparing bulk material with nanocrystalline microstructures for the machining of meso-scale parts is to use the cold spray process to consolidate a feedstock powder containing a nanocrystalline microstructure. Preparation of micron size powder containing a nanocrystalline microstructure by ball milling under liquid nitrogen (LN_2) is well known [4-11, 4-2]. Ajdelsztajn has shown previously that cold spray can be used to successfully consolidate LN_2 ball milled powders containing a nanocrystalline microstructure (10-30 nm grain size) [4-12].

The goal of the work reported here is to demonstrate that cold spray is a feasible approach for preparing bulk metal shapes containing homogenous nanocrystalline microstructures suitable for fabrication of meso-scale mechanical components. Once prepared, the intent is that cold sprayed bulk metal shapes will be used as stock for machining meso-scale mechanical components. Near-net-shape forming followed by finish machining is not a goal of this work. Instead the intent is to prepare larger pieces of metal stock with grain sizes appropriate for meso-scale parts. The expectation is to machine multiple meso-scale components from a single cold spray nanocrystalline coating. This work only reports the feasibility of preparing metal stock with suitable microstructure, it does not address mechanical properties, aging, or machineability.

Cold spray is a well known coating process in which a metal feedstock powder is sprayed at high velocity (~ 1000m/s) and low temperature (<100°C) [4-13]. A cold spray torch consists of a converging-diverging nozzle, a gas control system, a powder feed system, and a gas heater. Feedstock powder is injected into a high pressure (> 200psig) He or N_2 gas flow just upstream of a converging-diverging nozzle. The powder is entrained in the gas stream and reaches supersonic velocities as it travels through the nozzle. The propulsion gas stream is often heated to moderate temperatures (< 600°C) in order to increase the sonic velocity of the gas and thus increase the particle velocity. Heating of the propulsion gas typically does not result in significant powder heating [4-14]. Upon impact with the substrate the metal powder experiences significant mechanical deformation. This deformation causes a hydrodynamic instability to form at the particle-substrate contact allowing breakup of surface oxides, shear along the particle-substrate interface, and ejection of material from the particle-substrate interface. This process results in mechanical and metallurgical bonding between the particle and substrate. It also results in significant plastic deformation of the impacting particle as well as the substrate in the immediate vicinity of the impacting particle. As subsequent particles impact and consolidate a coating or bulk shape is formed [4-15, 4-16]. Process vectors for cold spray are well understood. As particle velocity increases deposition efficiency, coating density, residual stress, and coating adhesion strength all increase [4-14].

The mechanisms responsible for nanocrystal formation during the ball milling process are also well understood. Fecht [4-11] explains that nanocrystals form during severe plastic deformation in three stages. Initially high density arrays of dislocations are formed. As plastic deformation continues these dislocations annihilate and recombine forming sub-grains with low angle grain boundaries. Further deformation causes the sub-grains to rotate forming high angle grain boundaries.

4.3 Experimental Procedure for Cold Spray

4.3.1 Feedstock

The 5083 aluminum powder was purchased from Novemac LLC, (Dixon, Ca). The 6061 aluminum powder was purchased from Valimet (Stockton, Ca). Both powders were produced using inert gas atomization. All LN_2 ball milling of these powders was also conducted by Novemac LLC using a proprietary, high efficiency, LN_2 ball milling process. All powder size distribution measurements were made using a Beckman-Coulter Laser Diffraction Particle Size Analyzer. This machine is a dry-type particle size analyzer using a Fraunhaufer diffraction criterion to determine particle size distribution. A field emission SEM was used to determine the morphology of each powder.

4.3.2 TEM Sample Preparation and Imaging

Transmission electron microscopy (TEM) samples were prepared using the focused ion beam (FIB) lift-out technique. This procedure used a dual electron-Ga ion beam instrument (FEI DB-235). For the starting powders, particles were sprinkled onto carbon tape on an aluminum stub. Areas on the surface of a given particle were selected and coated with electron beam and ion beam deposited platinum to protect the surface of the section during ion milling. TEM sections approximately 10μm by 5μm by 200nm were milled using a 30keV Ga ion beam. The section was then ion polished with a 5keV Ga ion beam prior to detachment and lift-out. The resultant TEM section was placed onto a thin carbon membrane on a copper TEM grid. For the sprayed coatings, the process was identical except that the sample was simply placed into the chamber in a plan view orientation, and an area for analysis was chosen.

The TEM characterization was performed using a Phillips CM30 TEM at 300keV. Bright field images, dark field images, and diffraction patterns were collected using both a solid state image plate system (DITABIS) and a Gatan Image Filter (GIF) camera.

4.3.3 Cold Spray

Cold spraying was conducted at Sandia's Thermal Spray Research Laboratory in Albuquerque, NM using a cold spray system that was designed and built by Ktech Corp. Albuquerque, NM. The cold spray nozzle used for these experiments had a 2.0 mm diameter throat, a 100 mm long supersonic region, and a 5 mm diameter exit orifice. Helium was used as the propulsion gas. All coatings were sprayed using 2410kPa (350psig), 350°C He flow. All samples were prepared using a raster speed of 50 mm/s, a raster step size of 1 mm, and a standoff distance of 25 mm. All coatings were prepared on 6061 aluminum substrates that were grit blasted and solvent cleaned prior to spraying.

4.4 Results for Cold Spray

4.4.1 Powder, Morphology, Microstructure, and Size Distribution

Powder size distributions for the as-received 5083 and 6061 powders are shown in Figure 4-2. Figure 4-3 shows the powder size distributions for the LN_2 ball milled 5083 and 6061 powders. All of the powders have gaussian powder size distributions. Table 4-1 shows the mean particle sizes and approximate mean particle velocities at the spray conditions used to prepare the coatings reported here. All particle velocities in Table 4-1 were calculated using the method described by Dykhuzien and Smith [4-17], Equation #20. The measured mean size of both the 6061 and 5083 powders increased as a result of ball milling. SEM images of the as-received powder and the LN_2 ball milled powder, Figure 4-4 and Figure 4-5, respectively, show that these powders were flattened considerably during the ball milling process and are now flake-like, as expected. It is likely that the powder size measurement was skewed by the high aspect ratio of the ball milled particles. The Beckman-Coulter instrument assumes a spherical particle.

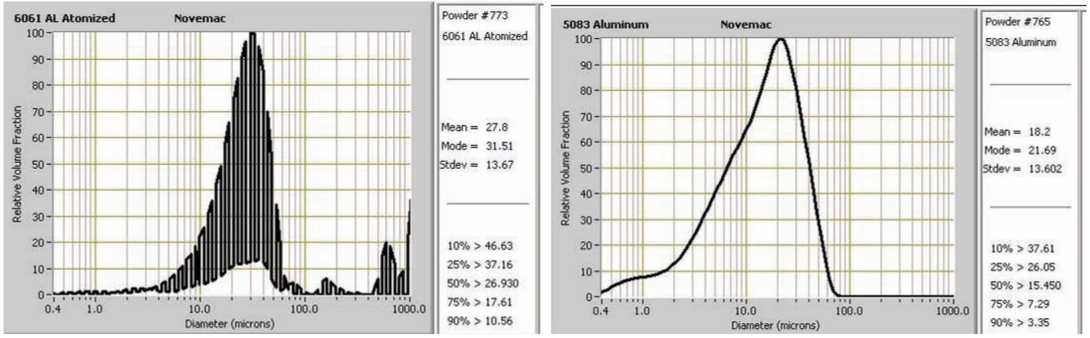

Figure 4-2 Powder Size Distribution Measurement for the As-Received 5083 Atomized (left) and the 6061 Atomized (right) Feed Stocks

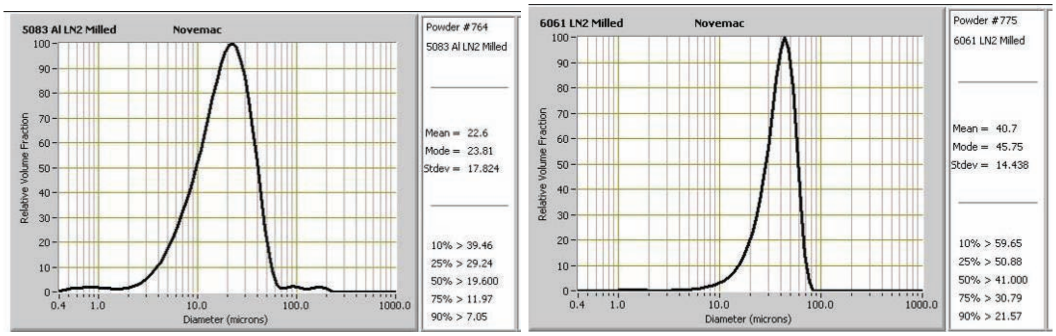

Figure 4-3 Powder Size Distributions for the 6061 (left) and 5083 (right) Powders After LN_2 Ball Milling.

Table 4-1 Mean Particle Sizes and Corresponding Particle Velocities Achieved with a 2410kPa (350 psig), 350° He Flow.

Powder	Mean Size (μm)	Calculated Mean Centerline Particle Velocity (m/s)
6061 As-received	27.8	1137
5083 As-received	18.2	1264
6061 LN2 Ball Milled	40.7	1022
5083 LN2 Ball Milled	22.6	1199

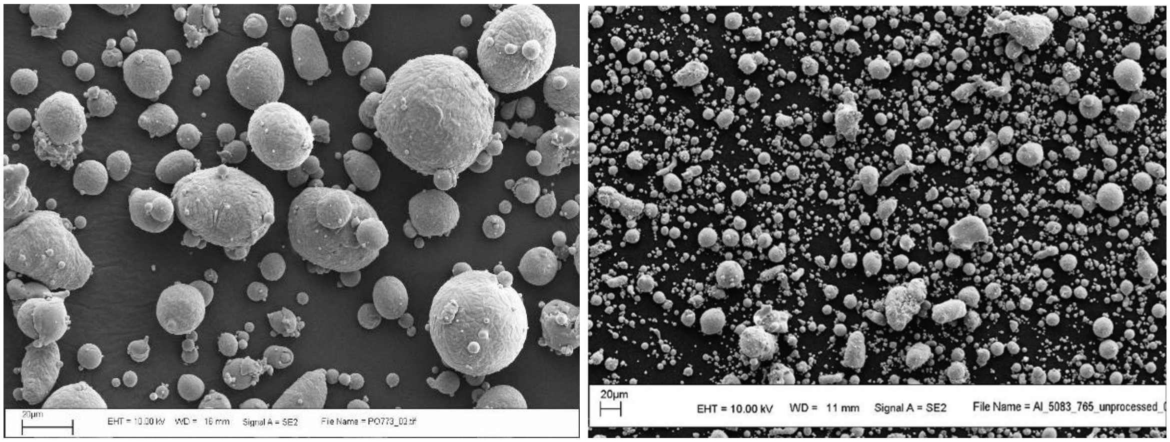

Figure 4-4 SEM Images Showing the As-Received Morphology of the Atomized 6061 (left) and the Atomized 5083 (right) Powders.

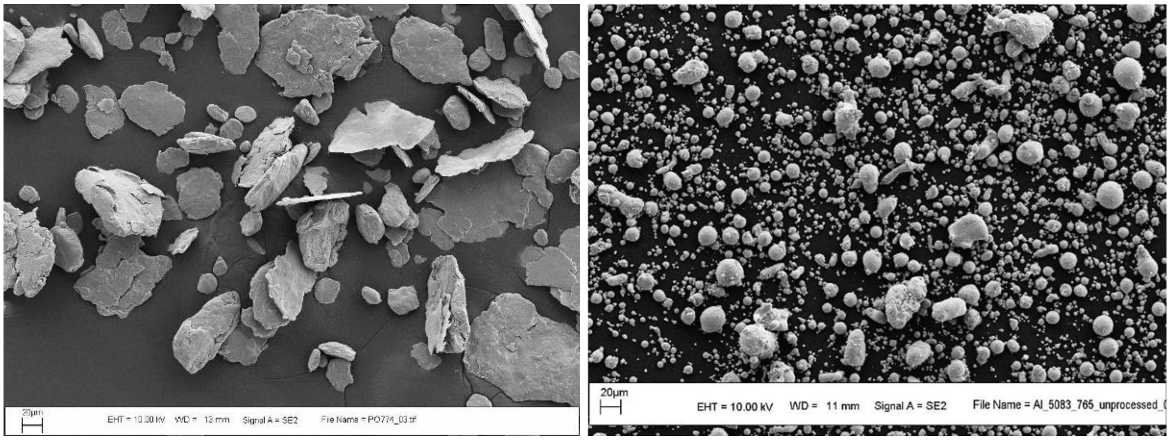

Figure 4-5 SEM Images Showing the Morphology of the LN_2 Ball Milled 6061 (left) and 5083 (right) Powders.

The ball milling process causes considerable flattening of the powder. This makes the powder more difficult to feed into the cold spray process, use of a pneumatic vibrator on the hopper is necessary, but does not appear to otherwise affect its behavior.

Figure 4-6 and Figure 4-7 show TEM images of the as received powders and the LN_2 ball milled powders, respectively. The LN_2 ball milling process has resulted in significant grain refinement creating an ultra-fine grained structure in the 6061 LN_2 ball milled powder and an elongated nano-crystalline structure in the 5083 powder. The grain size of the as received powders is on the order of microns. After LN_2 ball milling the 6061 grain size is between 250 and 400 nm. The 5083 grains are 20-40 nm in width but are highly elongated. Distinct morphological texture was observed for both ball-milled powders. The microstructure consisted of elongated lamellar or pancake-shaped grains with lengths 5-15 times their thickness. These grains were also oriented parallel to the surface of the powder particle and are likely the result of deformation associated with the ball milling process. Despite the strong morphological texture in the LN_2 ball milled powders, there was no particularly significant crystallographic texture observed in the selected area diffraction patterns (Figure 4-7). Note: All of the grain sizes given in this paper were determined using the TEM images shown. Thus, grain sizes are given as a range (e.g. 20-40 nm) and are somewhat approximate.

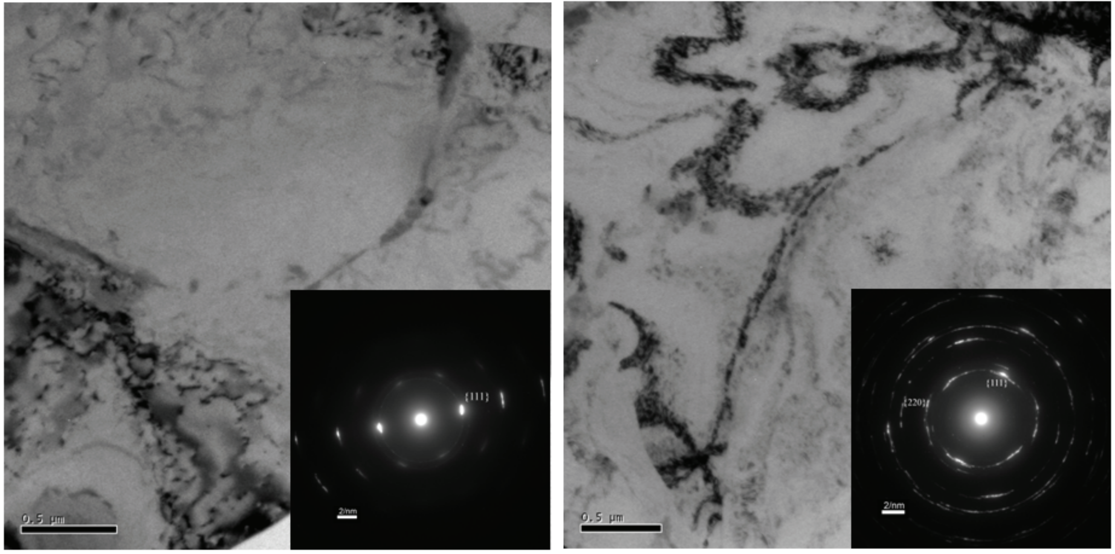

Figure 4-6 TEM Images Show Coatings Prepared Using the As-Received Atomized 6061(left) and 5083 (right) Powders. SADP Shows 6061(left) To From a Single Grain With Size >1µm. SADP From 5083 (right) Shows Heavily Smeared Spots From >500nm Deformed Grains.

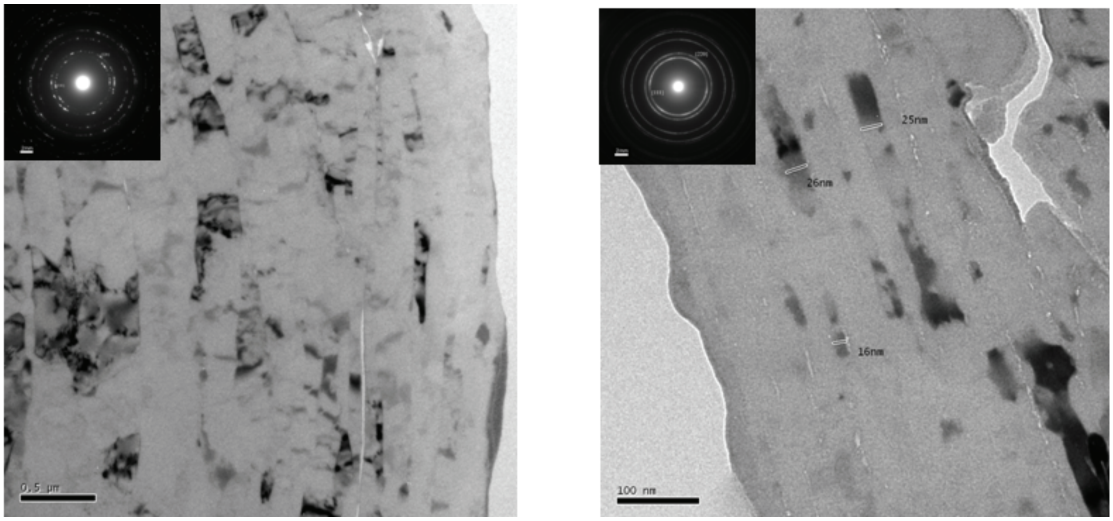

Figure 4-7 TEM Images Show the Microstructure of the 6061(left) and 5083 (right) Powders After LN2 Ball Milling. Notice That Both Powders Have Elongated Grains.

4.4.2 Coating Microstructures

Nanocrystalline 5083 and 6061 coatings were prepared on 50.8mm x 50.8mm x 3.175mm (2” x 2” x 1/8”) aluminum substrates. Figure 4-8 is a picture of the two coated test coupons. The 5083 coating is 0.058mm (0.0023”) thick. The 6061 coating is 0.513mm (0.0202”) thick.

Figure 4-9 and Figure 4-10 are TEM images showing microstructures of coatings prepared using the as-received and LN_2 ball milled powders. All coatings prepared with the as-received powders exhibited micron sized grains, as expected. However, both coatings prepared using the LN_2 ball milled powders exhibited 30-50 nm grain sizes. This was unexpected given the elongated grains in both powders and the 250-400 nm grain size in the 6061 LN_2 ball milled powder. In both cases, no crystallographic texture was observed in the diffraction patterns from the coatings. Additionally, a good deal of nano-scale porosity was observed in these coatings. The porosity was highly aligned with lath boundaries in the 5083 alloy and with much less alignment in the 6061 alloy.

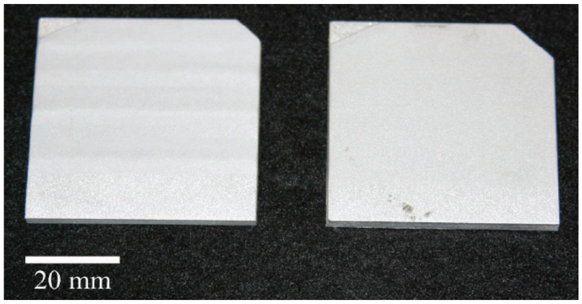

Figure 4-8 As-Sprayed Nanocrystalline Aluminum Coatings of Alloys 6061 (left) and 5083 (right) Are Shown.

4.5 Discussion for Cold Spray

As shown by the TEM images above (Figure 4-6 through Figure 4-9), the cold spray process resulted in significant grain refinement for both the 6061 and the 5083 LN_2 ball milled powders. The grain size reduction from 250-400 nm in the LN_2 ball milled 6061 powder to 30-50 nm in the cold sprayed coatings is approximately a factor of eight in grain size and close to a factor of 70 in grain volume. The grain refinement in the 5083 is similarly dramatic. The elongated 5083 grains are equiaxed in the cold sprayed coating. Most likely this grain refinement occurred through mechanisms similar to those proposed by Fecth [4-11]. It is reasonable to expect that the deformation associated with the cold spray process could result in sufficient dislocation generation and subgrain rotation to cause grain refinement. Grain refinement during the cold spray process has been documented before in pure aluminum of normal grain size [4-16]. The lath structure in the LN_2 ball milled powder appears to be retained in the 5083 cold spray coating.

Interestingly, the observation of grain refinement as a result of the cold spray process reported here appears to be in direct contrast to the results reported by Ajdelsztajn [4-11] in 2005. Ajdelsztajn also used the cold spray process to consolidate LN_2 ball milled 5083 aluminum powder. This study clearly showed that the cold spray process is an effective method of consolidating nanocrystalline powders. However, Ajdelsztajn reported that no grain refinement was observed during the cold spray process. The nanocrystalline grains in Ajdelsztajn’s coating were of similar size to the nanocrystalline grains in the LN_2 ball milled 5083 Al powder sprayed at Sandia. While the results of these two studies may appear to be in contrast; they are not. The experiment reported here was substantially different from Ajdelsztajn’s experiment in two important ways. First, Ajdelsztajn’s spray conditions were significantly different from the conditions used in this experiment. This may have resulted in lower average particle velocity in Ajdelsztajn’s experiment. Ajdelsztajn’s experiment used a room temperature 1.7MPa (~ 250psig) helium flow to propel the particles. The experiments reported here used a 2.41MPa (350°C), 350 psig helium flow to propel the particles. Thus, more energy and more plastic deformation were available in this experiment compared to Ajdelsztajn’s experiment. Second, and more importantly, Ajdelsztajn’s 5083 aluminum feedstock was ball milled to a grain size of 20-30 nm before spraying. Work by Romanov and Eckert suggests that it may become increasingly difficult or impossible to create grain sizes in aluminum smaller than 20 nm by plastic deformation mechanisms [4-3, 4-17]. Romanov explains that a critical crystal size exists below which gliding dislocations are unstable due to image forces. In aluminum Romanov estimates the critical size for dislocation stability as 18 nm. Below this size, gliding dislocations will be unstable and will rapidly move to grain boundaries or annihilate. Instability of dislocations would make it more difficult to create the dislocation networks, sub-grain boundaries, and ultimately the high angle grain boundaries required for deformation induced grain refinement. Eckert [4-17] explicitly considers the problem of minimum grain size obtainable by ball milling and explains that minimum grain size is determined by a competition between plastic deformation and the recovery behavior of the material. Minimum grain size for aluminum is shown to be between 20 and 25 nm.

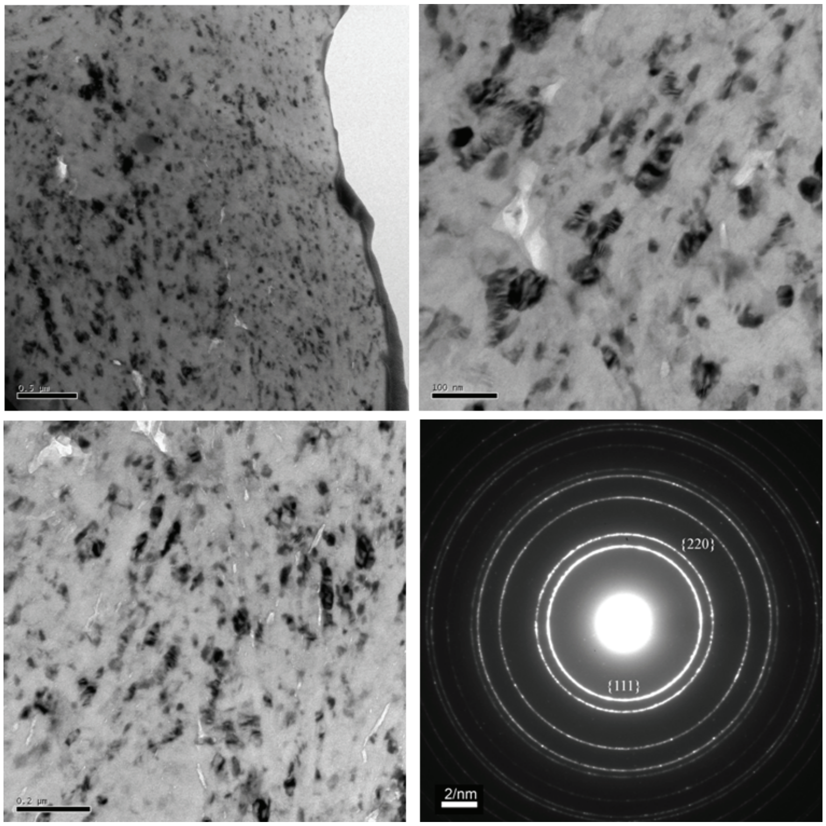

Figure 4-9 Three TEM Images Showing the Microstructure of the Cold Spray Coating Prepared Using the LN2 Ball Milled 6061 Powder. The Selected Area Diffraction Pattern (SADP) Shows Complete Rings with No Discernable Texture.

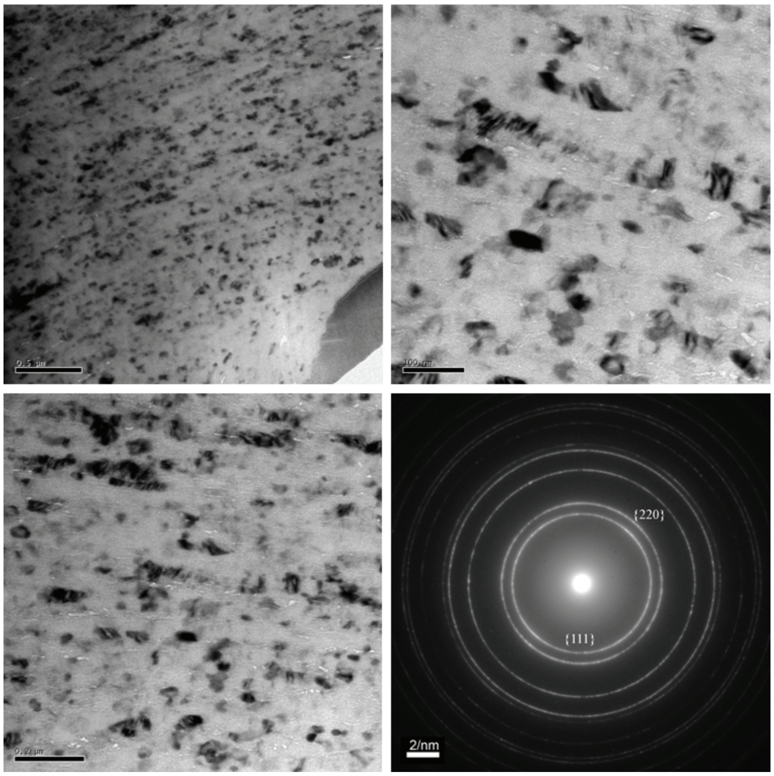

Figure 4-10 Three TEM Images Showing the Microstructure of the Cold Spray Coating Prepared Using the LN2 Ball Milled 5083 Powder. The SADP Shows Complete Rings with No Discernable Texture.

4.6 Conclusions for Cold Spray

This experiment clearly demonstrates that cold spray can be used to refine the microstructure of an ultra-fine-grained (100’s of nm grain size) powder and consolidate it to create a homogenous nanocrystalline (20-40nm) microstructure. When compared to the work of Ajdelsztajn which shows that the cold spray process can be used to consolidate nanocrystalline aluminum without causing recrystallization it illustrates the flexibility of the cold spray process. This flexibility is typical of spray processes and highlights the need to further understand the process-microstructure-property relationships in nanocrystalline cold spray coatings. The cold spray process is likely an extremely controllable method for preparing metal coatings and bulk metal shapes with homogenous nanocrystalline microstructures. If grain refinement in the cold spray process is occurring by the mechanism proposed by Fecth [4-11], cold spray should be capable of preparing nanocrystalline microstructures from almost any sprayable metal feedstock. The following specific conclusions were reached from the data presented in this study.

1. The cold spray process can cause the refinement of ultra fine grained powdered aluminum feed stocks creating a homogenous nanocrystalline microstructure.
2. Grain refinement observed in Al due to cold spray occurs because of the severe plastic deformation associated with the cold spray process.

4.7 Acknowledgements for Cold Spray

The authors would like to acknowledge Dr. Leonardo Ajdelsztajn for his advice on sources for LN_2 ball milled powder and for his insightful work on cold sprayed nanocrystalline aluminum. It was a foundation and significant motivator for the experiments reported here.

5 SHOCK CONSOLIDATION OF NANO-CRYSTALLINE 6061 ALUMINUM

The team developed methods to use shock compaction for the consolidation of nanocrystalline metal. The compacted materials were then studied to understand the effects of the process and incoming powder on the final part microstructure. The following section, written by team member D. Anthony Fredenburg, will be submitted for publication in the near future.

5.1 Abstract for Shock Consolidation

Nanostructured materials offer unique microstructure-dependent properties that have the potential to be far superior to course-grained materials; however, they also present new challenges in the formation of bulk components. In this work, both fully and partially nanocrystalline aluminum powders are consolidated into bulk form using dynamic compaction. Overall compact densities range from 98.4-99.0 %TMD; the partially nanocrystalline compact achieved the highest density. High hardness is recorded in the fully nanocrystalline compacts, averaging, and is attributed to the fine grain structure. Fully nanocrystalline starting powders show grain refinement in the compacted state with a bimodal microstructure composed on 50-100 nm thick laths and 10-50 nm equiaxed grains. Compact hardness averages ~193 $HV_{.05}$ for fully nanocrystalline compacts. Partially nanocrystalline powders retain graded microstructures following dynamic consolidation with evidence of subgrain formation. Hardness tends to decrease with distance from the impact face for partially nanocrystalline compacts.

5.2 Introduction to Shock Consolidation

Nanostructured materials, polycrystalline materials with average grain sizes < 100 nm in at least one dimension, are of engineering interest because they offer novel properties compared to their course-grained counterparts. As grain size decreases into the nanometer regime, mechanisms dominating the physical and chemical properties of materials change and have been reported to result in substantial improvements in thermal, mechanical, electrical, optical, and magnetic properties [5-1 - 5-6]. However, the formation of bulk materials with nanocrystalline grain structures poses significant engineering challenges.

In recent years the production and characterization of bulk nanocrystalline aluminum alloys has garnered much attention due to their high strength to weight ratio. Generally, for these alloys research has shown a reduction in grain size is accompanied by an increase in tensile strength and hardness and a reduction in ductility and toughness [5-7]. Han *et al*. [5-8], investigating a cryomilled nanocrystalline 5083 Al alloy, reported an increase in yield strength of ~365 % over the course-grained alloy to 713 MPa, however, this was accompanied by an elongation to failure of only ~0.3%. To make these alloys more attractive for structural applications ductility must be increased. One such method for increasing ductility is through the introduction of a bimodal grain structure composed of nano- and micron-scale grains through annealing [5-9], or the combination of nanocrystalline powders with unmilled course-grained powders [5-10]. These techniques have resulted in significant improvements in ductility with limited and controllable reductions in strength. However, special care must be undertaken during processing as Huang *et al*. [5-11] has found that annealing a 99.99% pure aluminum specimen at a low temperature, without the introduction of the bimodal structure, resulted in increases in flow stresses and decreases in ductility, in stark contrast to the annealing behavior of course-grained aluminum alloys. They also observed a reduction in flow stress and increase in ductility to approximate pre-anneal values through subsequent deformation of the annealed specimen. Thus through proper engineering controls, the production of high strength-moderate ductility nanocrystalline aluminum components is possible.

One of the more popular means of forming bulk nanostructured materials is through the consolidation of nanoscrystalline powders formed through cryomlling, the milling of micron-sized powders at cryogenic temperatures to form nanograined particulates. Generally, the evolution from micron to nanoscale grain structures during milling occurs in three distinct stages such that during the initial stage shear bands with high dislocation densities form as a result of large-scale plastic deformation. With further deformation, strain levels increase causing the annihilation and recombination of dislocations and result in the formation of low angle subgrains with nanometer length scales. Finally, single-crystal grains reorient to form random high-angle misorientations between grains [5-12]. In addition, when milling occurs at cryogenic temperatures, the annihilation of dislocations is suppressed allowing particles to rapidly accumulate very high dislocation densities. Another important aspect of milling is the introduction of impurities (O, N, C, Fe, etc.) during grain refinement in the form of nanoscale dispersions. These dispersions have been shown to limit grain-boundary migration and enhance thermal stability in aluminum alloys, helping to preserve nanocrystalline grain structures during consolidation [5-8].

A more recent technique of forming nanocrystallline particles for subsequent consolidation is through plain strain machining. During machining, large shear strains are introduced along a narrow deformation zone, the shear plane, transforming the original microstructure and ejecting the chip from the bulk. This process employs a modulation assisted machining (MAM) technique, and through variations in undeformed chip thickness, cutting speed, frequency, and rake angle of the cutting tool chips can be produced with varying degrees of nanocrystallinity and morphology [5-13, 5-14]. However, the challenge still remains to consolidate these powders into bulk forms whilst retaining their original microstructures.

Some of the more prevalent consolidation methods for producing bulk nanocrystalline materials are hot- and cold-isostatic pressing, spark-plasma sintering, cold spray, and shockwave consolidation. Hot-isostatic pressing and spark-plasma sintering can be deleterious to the preservation of nanocrystalline grain structures because temperatures can reach ~0.7 Tm (solvus temperature) and can lead to grain growth [5-15, 5-16]. Cold-isostatic pressing and cold spray technology have the advantage of being lower temperature processes; however, interparticle bonding suffers as a result of low diffusion rates in cold-isostatic pressing and is highly particle size dependent for cold spray technology [5-8, 5-17]. Conversely, under the correct processing conditions, shockwave consolidation can circumvent the shortcomings of the aforementioned processes and produce fully nanocrystalline bulk materials [5-18, 5-19].

During shockwave consolidation short duration (~ 1 μs) stresses in excess of the materials yield strength are applied, causing particle deformation and densification of the compact. Particle deformation is highly heterogeneous with much of the deformation restricted to particle surfaces, which can result in extremely high heating and quench rates at particle surfaces while temperatures near the particle interior remain relatively constant [5-20, 5-21]. When forming components with fully nanocrystalline microstructures loading conditions must be carefully controlled such that excessive heating and cooling is minimized. At excessive stresses, temperatures can reach that of the melt and result in substantial microstructural changes as Brochu and co-workers [5-22] have observed a bimodal microstructure with larger grains localized near particle surfaces following explosive compaction of an initially equiaxed Al-Mg alloy. Stresses localization can also lead to the breakup of surface oxides which can aid in interfacial bonding [5-23]. However, as particle size decreases it becomes more difficult to break surface oxides, and Nieh et al. [5-24] have shown that for aluminum particles with average sizes between 50-70 nm stresses of 2-3 GPa are unable to breakup surface oxides, inhibiting the formation of metallurgical bonds between particles. Thus the formation of bulk nanocrystalline aluminum components by means of dynamic compaction is favored by the compaction of micron-scale nanocrystalline particles at moderate stresses, which leads us to our current approach.

In this work the authors investigate the use of dynamic compaction as a means of consolidating nanocrystalline aluminum alloy powders formed through severe plastic deformation machining and cryomilling. First, characterization of the starting powders is presented, followed by details of the experimental approach. Results and discussion follow, covering compact density, microstructure, grain size, and microhardness for dynamically compacted samples. At this juncture no attempt is made at characterizing the elastic properties of the compacts, and reporting of said properties will be presented in a future work.

5.3 Experimental Procedure for Shock Compaction

5.3.1 Starting Powders

The powders used in this investigation are a liquid nitrogen ball milled aluminum 6061 alloy obtained from Novemac LLC (Dixon, CA), and an equiaxed aluminum 6061 alloy formed by a frequency modulation assisted machining process obtained from M4 Sciences (West Lafayette, IN). The former will henceforth be referred to as LN2 BM ##% and the latter M4Sci EQ ##%, where ##% indicates the initial packing density of the compacts in percent, with respect to theoretical mass density (TMD). Mean particle sizes and standard deviations for LN2 BM and M4Sci EQ powders were characterized using Fraunhofer diffraction as 40.7 +/- 14.4 µm and 63.6 +/- 23.5 µm, respectively. In addition to particle size, particle morphology and crystallite structures differ greatly between powders due to their highly heterogeneous processing methods. Representative particle morphologies and microstructures for the two starting powders are shown in Figure 5-1and Figure 5-2.

LN2 BM powders exhibit highly deformed regions on all surfaces, are spherical/elliptical in shape, and have a uniform lath-like grain structure with high dislocation densities. Lath thicknesses are between 200-400 nm. Similar elongated grain structures are observed by Han and co-workers [5-8, 5-25] in a cryomilled Al-Mg alloy and are attributed to milling times less than that required to achieve a fully equiaxed structure. TEM also shows limited porosity located almost exclusively at the grain boundaries, which may be a result of segregation of solute atoms to the grain boundaries causing void nucleation and/or grain boundary sliding during cryomilling [5-26]. Also, selected area diffraction (SAD) does not show evidence of any strong crystallographic orientation.

In contrast, M4Sci EQ powders appear physically smooth on some surfaces and jagged on others, are predominately blocky in shape, and have a graded microstructure. TEM images show a 1-2 µm thick layer near the particle surface of approximately equiaxed crystallites between 100-300 nm in diameter. As distance into the particle increases the microstructure consists of larger grains (> 1µm) with high dislocation densities. Evidence of this graded microstructure is also observed in SAD patterns where discrete reflections are observed in the particle interior and spotty rings are observed near the surface.

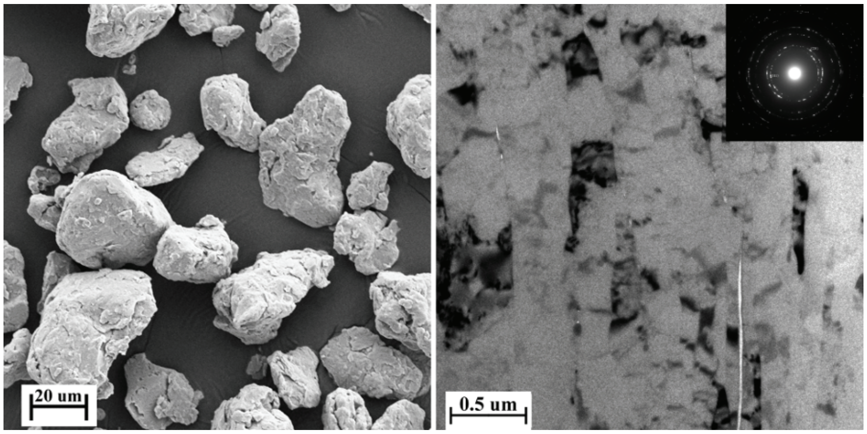

Figure 5-1 Images of LN2 Ball Milled Powder Showing (a) Particle Morphology and (b) Microstructure.

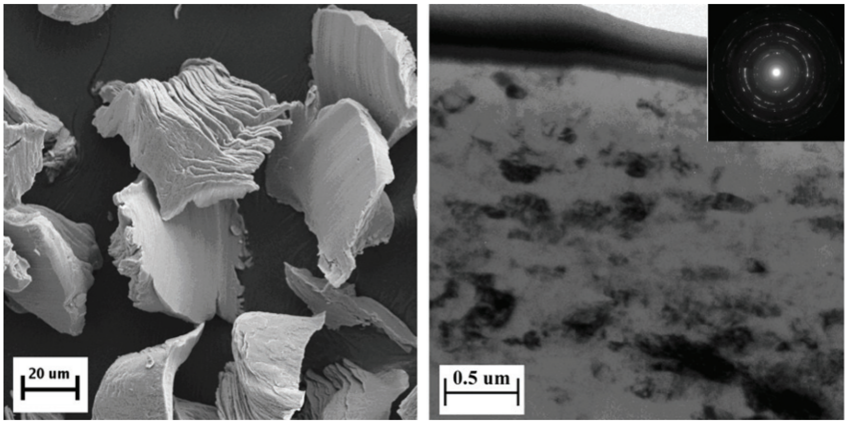

Figure 5-2 Images of M4Sci 6061 Equiaxed Showing (a) Particle Morphology and (b) Microstructure Near Particle Surface

5.3.2 Dynamic Consolidation and Analysis

Aluminum powders in this study were dynamically consolidated within a 3-capsule recovery fixture on an 80 mm bore diameter single-stage light gas-gun at the Georgia Institute of Technology. Mass of the powders were measured using a microbalance with 10^{-4} g resolution, and powders were pressed into individual steel capsules with an inner diameter of 11.988 mm using a Carver Auto Series “M” 3890 press. Powder thickness was measured using a depth micrometer with 10^{-3} inch resolution, and initial densities of the compacts range between 68 – 80 % theoretical.

Capsules were sealed with a steel plug and LOC-TITE ©, and a small amount of epoxy was used to attach capsule to the surrounding fixture. This fixture is similar to the fixture reported in a previous work [5-27], with the exception that in this investigation an air-gap exists between the capsule and the surrounding ring near the impact face and the entire fixture is steel. A radial cross section showing location of the air-gap is shown in Figure 5-3 The previous fixture design was modified to accommodate for the higher impact velocities used in this investigation such that the new design increases confinement of capsules in radial direction.

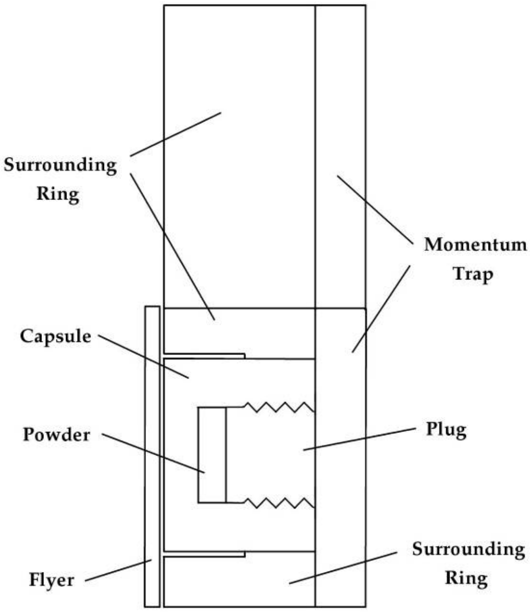

Figure 5-3 Cross-Section of One Capsule and Fixture Along Radial Direction Showing Location of Air-gap in Relation to Powder Compact.

Following assembly, the fixture was lapped to ensure planarity of the impact face and mounted to a set of planar stand-off blocks attached to the muzzle. The experiment tank was evacuated to ~ 50 mtorr, and an aluminum sabot and steel flyer plate were accelerated down the barrel of the gun using compressed helium as the driving gas. A series of four shorting pins were used to measure velocity of the incoming projectile, which was measured at ~ 730 m/s. Upon impact of the flyer plate with the fixture, compressive stress waves were generated causing compaction of the powder, and dimensions of the fixture and flyer are such that compaction of the powder was complete prior to arrival of release waves from the rear of the flyer.

The fixture and capsules were recovered in a soft-catch recovery tank, and compacts were machined out of the capsules with care taken to keep the temperature as low as possible. Following removal of the compact from the capsule, the rear surface of the compact was lightly sanded to remove any loose material and density determined using Archimedes displacement method with the aforementioned microbalance. Compacts were then sectioned into two halves parallel to the direction of impact for examination of compact cross-sections and transmission electron microscope (TEM) analysis. Optical micrographs and Vickers micro-hardness measurements of compact cross-sections were taken with a Leica DM IRM light microscope and a Leco MHT Series 200 micro-indenter. TEM specimens were cut near the impact and rear surfaces of the compacts using a gallium focused ion beam, where the plane of view is along the specimen cross-section. TEM imaging was carried out on an FEI Tecnai F30-ST microscope.

5.4 Results and Discussion for Shock Compaction

5.4.1 Dynamic Consolidation

The shock compaction stress in the powder compacts was 14.75 GPa, as determined through impedance matching techniques using the known impact velocity and equations of state of the flyer plate and fixture. However, due to large impedance mismatches between the steel fixture and the aluminum compacts, the initial compaction stresses in the powders were much lower; approximately 2.5 and 3.5 GPa for the 68% and 80% TMD compacts as inferred from continuum level simulations. Only after several stress reverberations in the compact will the specimen ring-up to the incident shock stress in the steel [5-24].

The production of a mechanically sound compact from powder constituents requires not only densification of powders, but also sufficient particle movement such that strong mechanical bonds between neighboring particles can form. The greatest amount of particle movement takes place under the influence of the lower magnitude initial stress pulse, and it is this stress which is responsible for the majority of compaction and resultant mechanical integrity of the compact. Under the experimental loading conditions the stresses present cause nearly full densification of the compacts. Compact density ranges between 98.4 – 99.0 % TMD, and have approximate dimensions of diameter 12 mm and thickness 2 mm. Figure 5-4 shows compacted LN2 6061 BM 68, and details of the initial and final compact densities for each compact are given in Table 5-1.

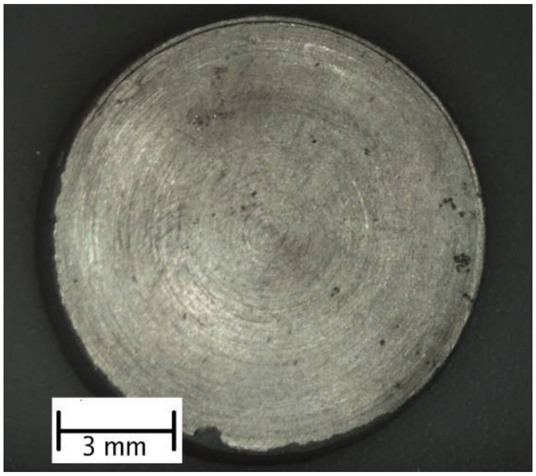

Figure 5-4. Shock Compressed LN2 6061 BM 68 Compact.

Table 5-1 Density of Powder Compacts Prior to Dynamic Loading ρ_{00} and Density of Shock Compressed Compacts ρ_C.

Powder	ρ_{00} (g/cm^3)	ρ_C (g/cm^3)
LN2 6061 BM	2.166	2.665 ± 0.004
LN2 6061 BM	1.842	2.658 ± 0.009
M4Sci 6061 EQ	1.844	2.673 ± 0.011

5.4.2 Microstructure of LN2 6061 Ball Milled Compacts

TEM and STEM analysis were conducted on samples taken from specimen cross-sections at the impact and rear surfaces to determine if the compacts exhibit through thickness variations in microstructure. Grain boundaries are observable in STEM image mode as a result of liquid metal embrittlement caused by the introduction of gallium during focused ion beam thinning of the samples [5-28]. Microstructural analysis of the compacts is presented in the following two sub-sections.

Microstructures for the LN2 Ball Milled (BM) 68% and 80% compacts appear very similar, and representative TEM and STEM images are given in Figure 5-5. The crystallite structure is bimodal in character dominated by larger lath-like grains and a low volume fraction of smaller equiaxed grains having diameters between 10-50 nm. The lath-like structure is similar to that observed in the starting powder; however, lath thickness is significantly reduced and typical lath thicknesses are between 50-100 nm.

Reduction in lath thickness results from the large amount of plastic deformation imposed on the particles during consolidation, and there have been many investigations to date concerning the deformation mechanisms responsible for plastic deformation as grain size enters the nano-regime [5-29 - 5-33]. It is the authors' belief that the dominant deformation mechanism responsible for lath reduction is slip. This hypothesis is supported by the predominately cellular microstructure observed following compaction. Though twinning may occur at these elevated strain rates, twinning in aluminum alloys tends to be favored at lower temperatures, small crystallite sizes, and in materials without precipitates or inclusions. Following ball milling, LN2 BM powders possess inclusions from the ball milling process in addition to any inherent precipitates in the alloy, all of which would serve to block twin formation. In addition, Gray [5-34] found no evidence of deformation twins in a 6061 Al alloy shocked to 13 GPa at -180 ºC, though grain sizes were much larger than in the present study.

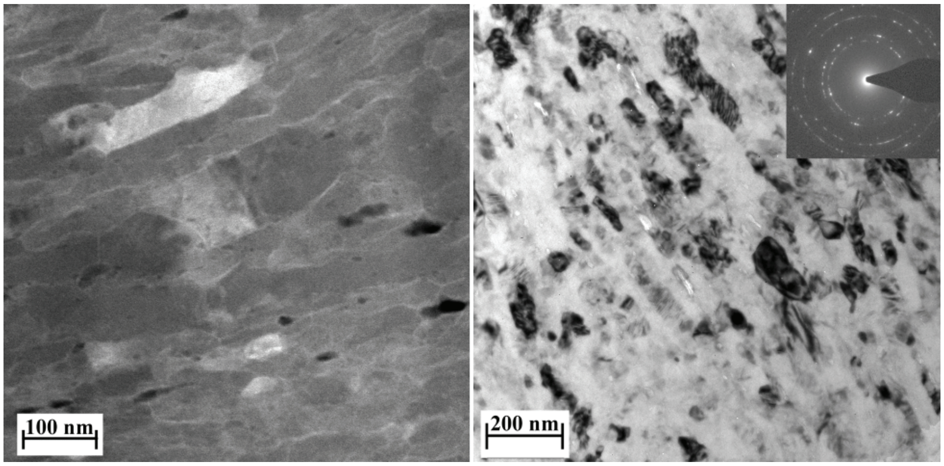

Figure 5-5 (a) STEM Image of LN2 6061 BM 68 and (b) TEM Image of LN2 6061 BM 80 Near Impact Face of Compact Showing Bimodal Grain Structure and Nanoscale Porosity.

Recalling the three stages of microstructure evolution that takes place during milling presented in [5-12], and that elongated grains have been attributed to insufficient milling times during nanopowder formation [5-8, 5-25], the following hypothesis regarding the reduction of lath thickness is presented. With the passage of the compaction stress a large number of dislocations are introduced through the propagation of shear bands. These dislocations interact with existing dislocations and form smaller subgrains that are slightly reoriented with respect to the initial lath orientation. TEM micrographs show many instances in the deformed microstructures where minimal contrast variation between neighboring laths is observed, indicating smaller laths may have originated from a similarly orientated larger lath.

Compacted samples exhibit a varied amount of microscale porosity and a fairly consistent amount of nanoscale porosity throughout the compact thickness. Nanoscale pores are located almost exclusively at grain boundaries, have typical widths of 10-20 nm, tend to be elongated in the lath direction, and can be observed in Figure 5-5. Increased amounts of micron scale porosity are observed near the rear surface of both LN2 BM compacts, and the increase in porosity at the rear surface is thought to result from radial stress effects. To gain further insight into the stress states present in the powder compact during impact, continuum level simulations of the impact event were undertaken and revealed radial stress waves approached the rear of the compact shortly after the initial compaction front. The interaction and reflection of these stresses could cause turbulent material flow and lead to shearing of the aluminum and subsequent void formation. Simulations also revealed a late time tension region which may also contribute to the observed porosity.

5.4.3 Microstructure of M4Sci 6061 Equiaxed (EQ) Compact

As detailed previously, the initial M4Sci EQ powder possesses a graded bimodal microstructure with smaller equiaxed grains near the particle surface and larger (> 1 µm) grains in the particle interior. Following dynamic compaction, a similar microstructure is observed in the compact. Figure 5-6(a) clearly shows this bimodal structure with smaller equaixed grains extending approximately 1 µm into the particle interior. Similar to the LN2 BM compacts, slip is believed to be the dominant deformation mechanism in the larger grains due to the T6 temper of the particles and the presence of precipitates which would prevent twinning.

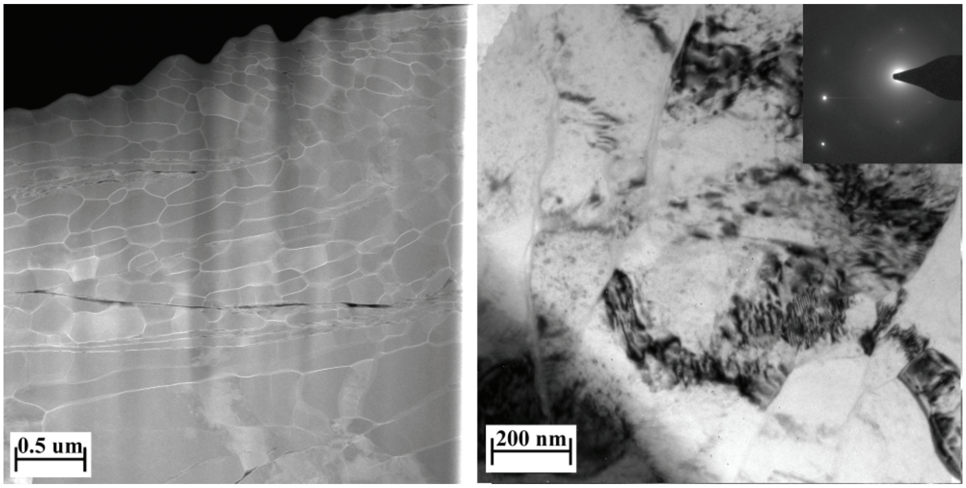

Figure 5-6 STEM Images of M4Sci 6061 EQ 68 Following Dynamic Compaction Showing (a) Graded Microstructure Near Rear Surface and (b) Low Misorientaion of Large Grains.

Large grains in the compacted specimen possess high dislocation densities and show areas of dislocation tangles often observed in the form of bands spanning the length of a grain. Figure 5-6(b) shows diffraction contrast in a large grain region as a result of the high dislocation density within the shock compressed samples. Banded structures are observed more frequently in the larger grains, which is consistent with observations of Zhu et al. [5-32] that grains are largely dislocation free in the size range of 50-100 nm as a result of the boundaries acting as sinks for dislocations. Intra-grain shear bands are also observed which traverse several of the larger grains. The presence of these bands shows the low misorientation angles between neighboring grains, and indicates the material may be in an intermediate step toward subgrain formation, see Figure 5-7.

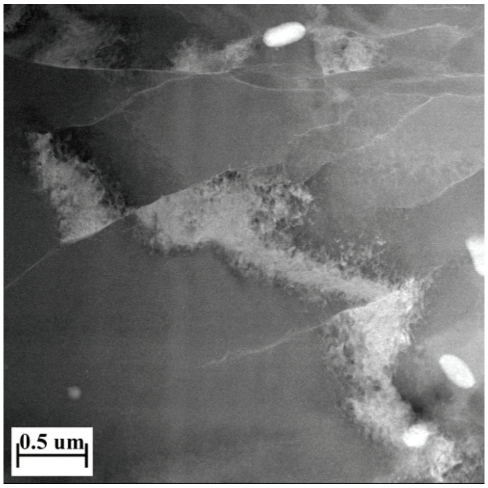

Figure 5-7 Dislocation Band Spanning Several Large Grains Showing Intermediate Step to Subgrain Formation as a Result of Plastic Deformation During Compaction.

Total porosity is reduced in the M4Sci EQ 68% compact compared to both LN2 BM compacts, with evidence of the micron scale porosity greatly reduced. The majority of porosity is observed inside or within close proximity to the fine grained regions and is dominated by smaller 10-100 nm diameter pores at grain triple points. M4Sci EQ particles are machined from stock in the T6 temper and inherently possess many fine-scale Mg_2Si precipitates. These precipitates inhibit grain boundary migration during particle formation and subsequently result in a large fraction of precipitates at particle grain boundaries. With precipitates preferentially located near grain boundaries, these could serve as void initiation sites and result in the observed void pattern. Bae and Ghosh [5-35] observed similar void patterns in an Al-Mg alloy and attribute this type of void formation to particle-matrix debonding. Larger, less frequently occurring voids are also observed and can span the length of multiple grain boundaries, reaching several microns in length, see Figure 5-7. These voids are also found predominately in the smaller grain region near particle surfaces and seem to be a result of the coalescence of multiple matrix-particle debonding instances.

5.4.4 Microhardness Profile

Hardness mapping of the compact cross-sections was carried out systematically over the breadth of the cross-section with 0.05” between columns through the compact thickness and 0.06” between rows along the compact diameter at an indentation load of 50 g. Average hardness values along the compact diameters for both LN2 BM and M4Sci EQ compacts are given in Figure 5-8 with overall averages of 193 and 105 $HV_{.05}$, respectively. Both LN2 BM compacts exhibit hardness values approximately 90 $HV_{.05}$ higher than the M4Sci EQ compact, and values are consistent with those reported by Brochu et al. [5-22] for a nanostructured Al-Mg alloy. High hardness values for LN2 BM compacts are attributed to their fully nanoscale grain structure.

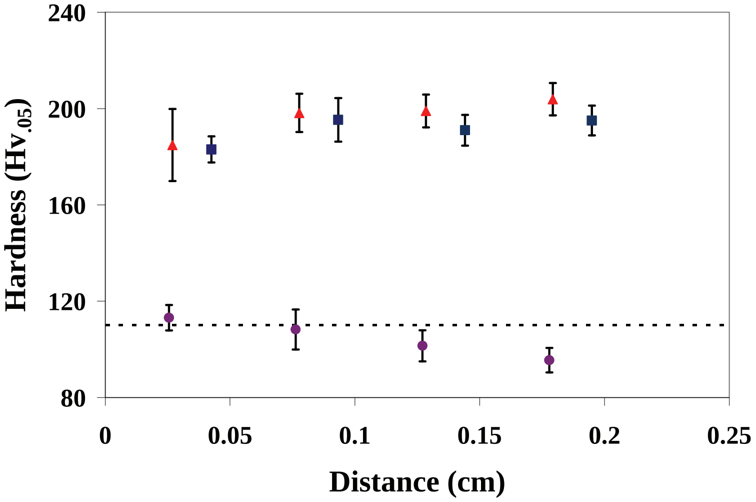

Figure 5-8 Vickers Hardness Values (HV.05) Averaged Along Specimen Diameters for (■) LN2 BM 80% (▲) LN2 BM 68% and (●) M4Sci EQ 68%. Bulk 6061 T6 Is Indicated By (---).

Hardness values along the compact diameter exhibit no observable trend in hardness, and minimal scatter is observed between recorded values. Through the compact thickness the LN2 BM compacts show a slight increase in hardness with distance from the impact face following the first series of indents; however, all values lie within their standard deviation to the overall average. Thus no definitive conclusion as to a trend in hardness for the LN2 BM compacts can be drawn at this time. The M4Sci EQ 68% compact, however, does exhibit a clear decrease in hardness with distance from the impact face. This reduction in hardness is attributed to higher temperatures experienced by the compact rear as a result of converging radial waves.

Continuum-level simulations of the impact event show converging radial waves with magnitudes > 10 GPa approaching the specimen rear less than 100 ns after the passage of the initial compaction front. The arrival of these converging radial waves leads to increased temperatures near the compact rear, and could lead to recovery of grain body dislocations and/or the reintroduction of precipitates into solution. For Al 6061 chips in the T6 temper, Swaminathan and co-workers [5-14] have shown that additional annealing results in a reduction in hardness as a result of coarsening of the originally ~ 80 nm grains. However, grain coarsening is not observed in the M4Sci EQ 68% compact, and the reduction in hardness to values below that of the bulk T6 alloy (dotted line in Figure 5-8) is thought to result from the reintroduction of precipitates into solution.

5.5 Shock Consolidation Conclusions

In this study, dynamic compaction was successfully used to consolidate fully and partially nanocrystalline 6061 aluminum powders, forming compacts ranging in density between 98.4-99.0 %TMD. Microstructures of fully nanocrystalline LN2 BM compacts exhibit grain refinement during consolidation yielding a bimodal grain structure with a large volume fraction of laths 50-100 nm in width and a smaller volume fraction of equiaxed grains 10-50 nm in diameter. Limited porosity is observed in these compacts with the level of nanovoids remaining consistent through compact thickness and a greater number of microvoids observed near the rear surface. Graded microstructural features are observed in the M4Sci EQ 68% compact, indicating preservation of initial microstructure, with larger grains showing high densities of dislocations in the form of bands which can span the length of several grains. The presence of these bands is thought to indicate the material is in an intermediate step toward subgrain formation. Compact hardness reflects microstructural features, with fully nanocrystalline compact hardness values reaching almost twice those of the partially nanocrystalline compacts. High hardness suggest components may also have high tensile strengths and work is currently underway characterize the elastic properties of the compacts.

5.6 Shock Consolidation Acknowledgements

The authors would like to thank Michael Rye and Paul Kotula for TEM sample preparation and analysis and Christopher Saldana for many useful conversations concerning the M4Sci EQ powder. Funding for this research is provided by Sandia National Laboratories, a multiprogram laboratory operated by Sandia Corporation, a Lockheed Martin Company, for the United States Department of Energy's National Nuclear Security Administration under Contract DE-AC04-94AL85000

6 A COMPARISON OF NANOCRYSTALLINE ALUMINUM PREPARED USING COLD SPRAY AND DYNAMIC CONSOLIDATION METHODS

As the analysis of the different consolidation methods proceeded, it became apparent that several of the characteristics of the different methods were similar and the team felt that it was prudent to perform a more in-depth comparative analysis. The following is a draft paper that will be submitted in the future. The paper, co-written by team members Anthony Fredenburg and Aaron Hall, is not quite complete due to the need to compare the starting powders used in each process. The materials require TEM analysis and this was not able to be completed during the project. However, knowing that the incoming materials were created by the same method, but using different parameters, the comparison is still valid and important.

6.1 Abstract for the Comparison of Consolidation Methods

Cold spray and dynamic consolidation techniques were used to successfully consolidate nanocrystalline aluminum 6061 powders to form bulk nanocrystalline components. Transmission electron microscopy (TEM) images of bulk components showed a reduction in grain size occurs during consolidation of powders for both processes. Cold spray coatings exhibited average grain sizes between 30-50 nm in diameter, and dynamically consolidated compacts contained a bimodal structure with smaller equiaxed grains 20-50 nm in diameter and elongated lath-like grains having thicknesses ranging between 50-100 nm. Mechanical properties of the cold spray coating and dynamically consolidated compact were obtained through nano-indentation and micro-indentation hardness measurements, respectively, with the cold sprayed coating exhibiting the highest hardness.

6.2 Introduction for the Comparison of Consolidation Methods

A recent trend in design of multi-component systems has been to reduce component size while maintaining or increasing its strength. This has led to the development of new classes of materials, such as high strength-light weight nanocrystalline (nc) aluminum alloys for use in microscale components. When component size reaches 10’s to 100’s of microns, conventionally processed large-grained components exhibit highly anisotropic mechanical properties due to directional dependence arising from a limited number of grains. Reducing grain sizes to nanometers in length eliminates this anisotropy as mechanical properties are derived from a larger aggregate of smaller crystallites. Numerous methodologies for producing bulk materials with nc-grain structures have been explored [6-1], and in this work attention is focused on bulk nanostructured materials formed through cold spray and dynamic consolidation methods.

Cold spray is a coating process which has successfully consolidated nc-materials including aluminum [6-2] and nickel [6-3] alloys and WC/Co [6-4] and copper alumina [6-5] composites. In this process 1-50μm size particles with nc-grain structures or agglomerates of nanosized powders are deposited onto a substrate at particle velocities ranging between 500-1000 m/s. Compressed gas, which can be heated up to 700 °C, flows through a converging/diverging nozzle and is used to accelerate the particles toward a substrate. Upon impact with the substrate, kinetic energy of the particles is transferred into mechanical work and heat through large shear stresses at the particle/substrate interface. This results in a large amount of plastic deformation and temperature generation in the vicinity of the interface and causes solid state bonds to form. Coatings are built on a layer by layer basis with previously deposited particles serving as the substrate for incoming particles. Though the gas is heated and significant temperatures are generated at the substrate/particle interface, temperature in the bulk of the particle remain much lower and make this process ideal for the consolidation of nanostructured materials

Another relatively low temperature consolidation technique is dynamic compaction/consolidation. Dynamic consolidation is a bulk material forming method which has been successfully used to produce both fully and partially nanostructured materials including aluminum alloys [6-6, 6-7], NiAl intermetallics [6-8], nc-Fe [6-9], and exchange coupled magnetic materials [6-10]. Typically, micron sized particles with nc-grain structures are quasi-statically compressed to 50-70 % of their theoretical density, then consolidated to near full density by the passage of a large amplitude (in excess of a materials yield strength) short duration (~1 μs) stress pulse. Stresses are generated by the impact of a high impedance flyer/driver with the lower impedance powder, where flyers/drivers can be accelerated by means of a compressed gas (plate impact) or explosives. Under the influence of the initial stress pulse, particles rearrange and slide past one another generating friction and heat at particle interfaces. Significant temperature increases are restricted to near surface regions as a result of friction; however, the bulk temperature of the particles remains relatively constant. Similar to cold spray, the low temperatures experienced by the bulk of the powders during dynamic compaction make this process well suited for the compaction and preservation of nanostructured materials.

In this work, nc-aluminum alloy powders compacted to near full density through cold spray and dynamic consolidation methods are examined. A brief description of the starting powders and processing methods are presented first. Microstructures and mechanical properties of the bulk materials are reported and discussed in the subsequent two sections, followed by concluding remarks.

6.3 Experimental Procedure for the Comparison of Consolidation Methods

Gas atomized 6061 aluminum powders (27.8 +/- 13.7μm) were obtained from Valimet (Stockton, Ca) and ball milled by Novemac LLC (Dixon, Ca) at liquid nitrogen (LN_2) temperatures using a proprietary, high efficiency, LN_2 ball milling process. Two batches of LN_2 ball milled 6061 Al powders were acquired from Novemac LLC, henceforth referred to as Batch 1 and 2; their morphologies are shown in Figure 6-1.

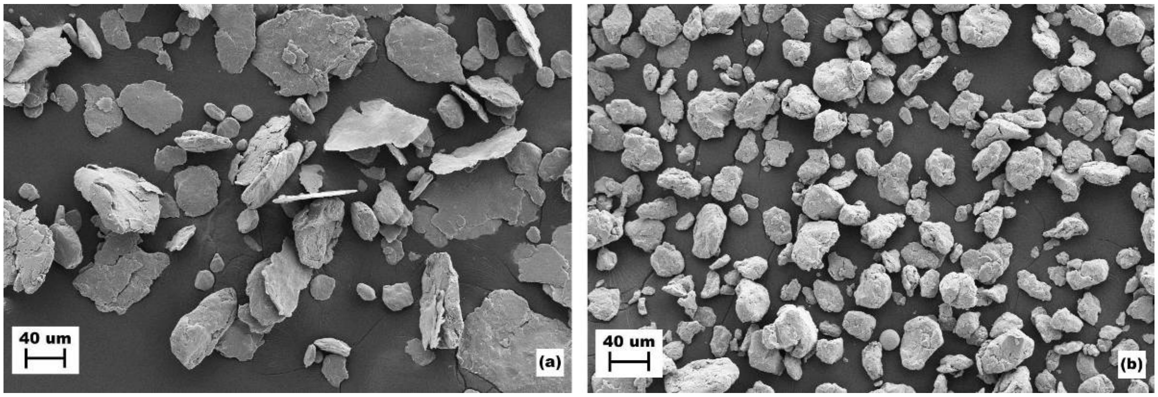

Figure 6-1 Nanocrystalline starting powder morphologies for (a) Batch 1 and (b) Batch 2.

Particle sizes for Batch 1 and 2 were measured using Fraunhofer diffraction as 55.7 +/- 28.1 μm and 40.4 +/- 14.4μm, respectively. Similar processing methods were used for both batches; however, particle morphology varies significantly as Batch 1 exhibits a plate-like morphology and Batch 2 shows an equiaxed/globular morphology. Transmission electron microscopy (TEM) images were only available for Batch 1 powders and a representative image is given in Figure 6-2. The microstructure consists of elongated lamellar grains 250-400 nm in thickness with lengths 5-15 times their thickness. Though particle morphology differs between the two batches, it is henceforth assumed that the microstructures for both batches are similar to those shown in Figure 6-2. Furthermore, the aim of this work is to compare the microstructures of the bulk materials following cold spray and dynamic consolidation, and not the starting powders.

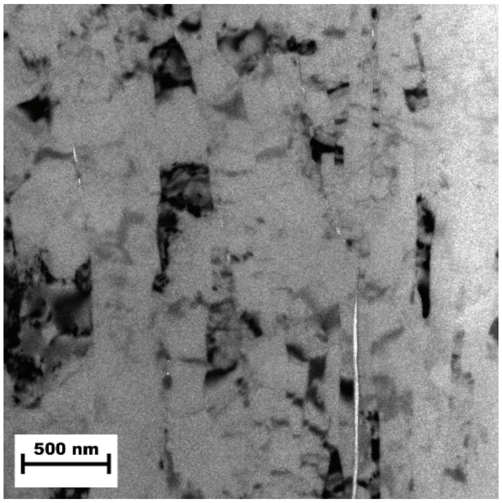

Figure 6-2 TEM image of LN2 ball milled starting powder microstructure, Batch 1.

Powders from Batch 1 were consolidated using the cold spray technique at Sandia National Laboratories Thermal Spray Research Laboratory, and Batch 2 powders were dynamically consolidated using the 80 mm gas gun at the Georgia Institute of Technology. TEM samples of consolidated materials were prepared using the focused ion beam lift-out technique with a Ga ion beam, and characterization was carried out on a Phillips CM30 TEM for cold sprayed specimens and an FEI Tecnai F30-ST TEM for dynamically consolidated specimens. Both microscopes operated at 300 kV. Nanoindentation Vickers hardness measurements were carried out on the cold sprayed material using an MTS Nanoindenter XP in continuous stiffness measurement mode with a standard Berkovich (T115) tip at indent depths of 250 and 1000 nm for both loading and unloading curves; hardness values for the 250 nm loading curve are reported here. Vickers microhardness was measured for the dynamically consolidated specimens using a Leco MHT Series 200 diamond tip micro-indenter with a 50 g load and 15 second dwell time. Specific details of experimental procedures and techniques for the cold sprayed material can be found in references [6-11] and [6-12] and in reference [6-13] for the dynamically consolidated material.

6.4 Results for the Comparison of Consolidation Methods

The results presented in the following two sections compare the microstructures and mechanical properties (hardness) of bulk nc-aluminum formed through two different processing methods, cold spray and dynamic consolidation. Results are taken from individual studies on cold sprayed

[6-11, 6-12] and dynamic consolidated [6-13] specimens and are presented here for comparison of bulk properties.

6.4.1 Microstructure

TEM images of representative microstructures for the cold sprayed and dynamically consolidated aluminum powders are shown in Figure 6-3. Both cold sprayed and dynamically consolidated samples exhibit grain refinement following consolidation. Beginning with elongated grains 250-400 nm in thickness, grain sizes of cold sprayed coatings are reduced to 30-50 nm in length. Dynamically consolidated samples exhibit a bimodal grain structure with smaller equiaxed grains 20-50 nm in diameter and slightly larger elongated laths with thickness ranging between 50-100 nm. Selected area diffraction does not indicate any preferred crystallographic orientation for either sample.

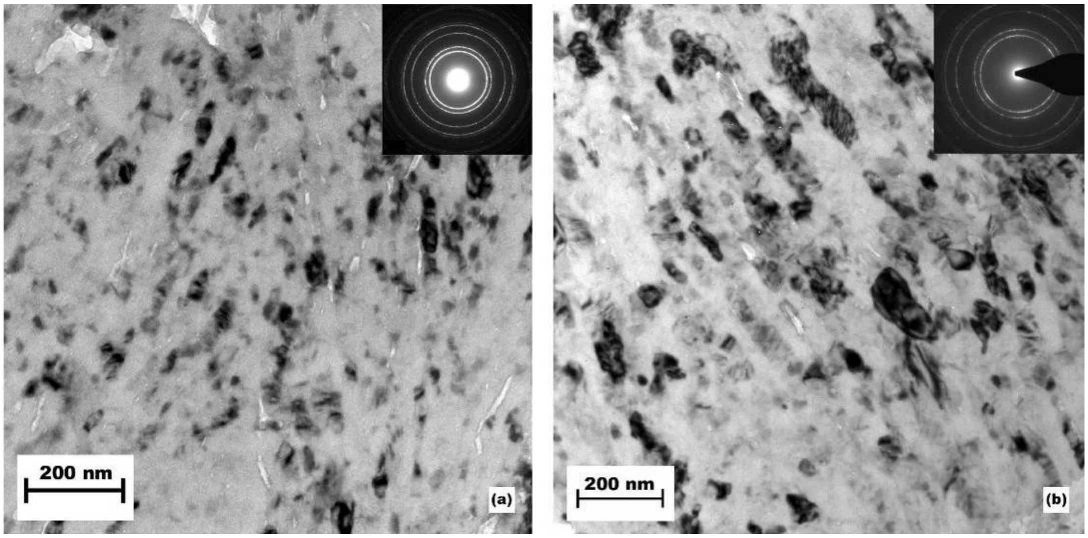

Figure 6-3 Microstructures of cold sprayed (left) and Dynamically Consolidated (right) nc-6061 Al Samples.

6.4.2 Hardness

Nano- and micro-hardness measurements for the cold sprayed and dynamically consolidated materials are reported in Table 6-1. Force-displacement nano-indentation measurements in [6-12] are reported in GPa, and the standard $HV_{.05}$ micro-hardness measurements in [6-13] are converted to GPa through the relation $GPa = 0.009807*HV$.

Table 6-1 Nano- and micro-hardness values reported for cold sprayed and dynamically consolidated samples.

Sample ID	**Nano- (GPa)**	**Micro- (GPa)**
Bulk Al 6061 T6	1.450 +/- 0.054	1.144 +/- 0.058
Cold Spray Al 6061 Coating	2.715 +/- 0.198	X
Dynamically Consolidated Al 6061	X	1.893 +/- 0.066

Both the cold sprayed and dynamically consolidated aluminum samples have higher hardness values than bulk Al 6061 T6 measured using their respective indentation technique. Nano-indentation of the cold sprayed coating and bulk 6061 T6 indicates coating hardness is increased

1.265 GPa over that of the bulk 6061 T6. Micro-indentation of dynamically consolidated Al and bulk 6061 T6 show an increase of 0.749 over that of bulk 6061 T6. Cold spray and dynamic consolidation specimens exhibit increases in hardness of 87 and 65 % respectively. In addition, hardness values measured using nano-indentation appears to be greater than those obtained through micro-indentations for the bulk Al 6061 T6 specimens.

6.5 Discussion for the Comparison of Consolidation Methods

6.5.1 Microstructure

Under the assumption that both initial microstructures resemble Figure 6-2, grain size reduction occurs during both cold spray consolidation and dynamic compaction of initially nanocrystalline Al powders. This reduction in grain size is thought to result from the large amount of plastic deformation that occurs during both consolidation processes. The minimum grain size in aluminum attainable through plastic deformation has been shown by Eckert [6-14] to be between 20-25 nm. Given that the powders start out with a lath-like structure with thicknesses between 250-400 nm, it is reasonable to assume plastic deformation during consolidation is responsible for the observed grain size reduction.

Plastic deformation of particles during cold spray occurs at two separate instances. As the particle initially impacts the substrate at high velocities it forms a crater in the substrate and material from the substrate and particle is jetted from the interface as the particle is flattened and bonds to the substrate [6-15]. In addition, as subsequent particles arrive at the previously deposited particles which are now acting as the substrate, additional plastic deformation occurs in the previously deposited particles as craters form to accommodate incoming particles. During dynamic consolidation, the bulk of plastic deformation occurs with the passage of the initial stress pulse with the rapid acceleration and deceleration of particles as they collide under the influence of the propagating stress pulse. This causes material to flow both parallel and perpendicular to the propagating stress pulse and can also result in turbulent (vortex) material flow at particle interfaces. The large amount of plastic deformation occurring during both consolidation processes results in substantial dislocation activity and grain refinement observed in the consolidated specimens. The extent of grain size reduction following the two consolidation techniques suggests particles undergo a greater amount of plastic deformation during the cold spray process. However, further work is needed examining the deformation behavior of particles during both consolidation techniques inclusive of the effects of particle morphology.

6.5.2 Hardness

Hardness results indicate that both cold sprayed and dynamically consolidated specimens show increases in hardness over bulk Al 6061 T6, with the cold sprayed coatings showing the highest overall hardness. The greater increase in hardness reported for the cold sprayed coating could be a result of the disparity in grain size between the two samples and porosity effects. Through empirical relationships like $\sigma_{TS} \sim 3$ HV [6-16], where σ_{TS} is the tensile strength, and the Hall-Petch relationship [6-17], a decrease in grain size can generally be associated with an increase in hardness. In this work, the cold sprayed coating has average grain sizes between 30-50 nm, which are smaller than those observed in the dynamically consolidated specimens. This reduction in grain size may contribute to the observed increase in hardness of the cold spray coating. In addition, nano-indentation measurements do not capture the effects of micro-scale porosity. Micro- and nano-scale porosity is observed in TEM images for both cold sprayed and dynamically consolidated specimens; thus nano-indentation measurements may result in higher reported hardness values as micro-porosity is not sampled in these measurements.

Another factor which may contribute to the higher hardness value reported for the cold sprayed coating is the indentation size effect. Table 6-1 shows higher hardness values for bulk Al 6061 T6 when indents are based on nano- as compared to micro-indentation. Elmustafa and Stone [6-18] have shown that hardness tends to increase with decreasing load for f.c.c. metals, and base their results on a dislocation mechanism similar to work hardening. Their analysis predicts higher hardness values for smaller indenter tip size and shallower indents which may contribute to the higher overall hardness observed in the cold sprayed coating.

6.6 Conclusions for the Comparison of Consolidation Methods

Nanocrystalline aluminum powders have been successfully consolidated to form bulk nanocrystalline aluminum 6061 alloys using both cold spray and dynamic consolidation techniques. Both processes show grain refinement following compaction resulting in microstructures consisting of 30-50 nm diameter grains for the cold sprayed coating and a bimodal structure for dynamically consolidated compacts. Cold sprayed coatings exhibit a greater amount of grain refinement than dynamically consolidated specimens. This is attributed to the greater amount of plastic deformation that occurs during the coating process; however, further investigation into the dynamics of deformation during each consolidation process is needed. Hardness measurements indicate cold sprayed coatings have a higher hardness than dynamically consolidated specimens, which is consistent with the level of grain refinement. However, variations in hardness measurement techniques may also be responsible for some of the observed increased hardness.

6.7 Acknowledgements for the Comparison of Consolidation Methods

Funding for this research is provided by Sandia National Laboratories, a multiprogram laboratory operated by Sandia Corporation, a Lockheed Martin Company, for the United States Department of Energy’s National Nuclear Security Administration under Contract DE-AC04-94AL85000.

7 CONCLUSIONS

Nanocrystalline metals carry the promise of high strength, high hardness, and high wear resistance in materials that designers have used for many years. This familiarity with the materials could help nanocrystalline metals to find significant use in a short time. Standing in the way of widespread use was the difficulty in consolidating the powder created by the most accessible nanocrystalline metal production methods.

The research conducted during this project has resulted in two methods of creating bulk nanocrystalline metal: cold spray and shock compaction. These methods are capable of not only creating bulk nanocrystalline material, but of further refining the material during the consolidation process. The consolidated material has been evaluated for microstructure and mechanical properties and has shown great potential. Consolidation of aluminum 6061 has demonstrated a hardness increase between 65% and 87%, depending on the process. The processes have shown the ability to create relatively dense material with porosity of 1-3%.

Other processes for creating nanocrystalline material were also evaluated during the project. Two machining based processes, Modulation Assisted Machining and Large Strain Extrusion Machining were evaluated for their ability to make nanocrystalline powders and bulk materials respectively. Initial testing showed the MAM powder to have a nanocrystalline shell, but to have larger nanostructured material inside the particles. LSEM was shown to create fully nanocrystalline material and was used to make the first ever meso scale nanocrystalline parts. The material, however, contains a significant amount of residual stress which limited the number of applications evaluated for the material.

This research clearly demonstrated the ability to create and utilize nanocrystalline materials and developed a greater understanding of their unique properties. It will now be important to pursue opportunities to evaluate these materials in specific applications to better understand best areas of opportunity for utilizing nanocrystalline material.

8 REFERENCES

Please note that there is some repetition in the references listed here. This is due to many of the chapters being self-contained papers that came as a result of this project. The duplication of references was permitted in order to retain the wholeness of the individual papers, especially since some of the papers are still in draft format and have not yet been submitted, and therefore can't be sited at the time of writing this report.

[1-1]Barker, L.M., and Hollenbach, R.E., "Laser interferometer for measuring high velocities of any reflecting surface," Journal of Applied Physics, vol. 43, no. 11, pp. 4669-75, Nov. 1972.

[1-2]Vandersall, K.S., and Thadhani, N.N., "Investigation of "shock-induced" and "shock-assisted" chemical reactions in Mo + 2Si powder mixtures," Metallurgical and Materials Transactions A, vol. 34A, no. 1, pp. 15-23, Jan. 2003.

[1-3]Xu, X., and Thadhani, N.N., "Investigation of shock-induced reaction behavior of as-blended and ball-milled Ni+Ti powder mixtures using time-resolved stress measurements," Journal of Applied Physics, vol. 96, no. 4, pp. 2000-09, Aug. 2004.

[1-4]Ferranti, L., and Thadhani, N.N., "Dynamic impact characterization of Al + Fe2O3 + 30% epoxy composites using time synchronized high-speed camera and VISAR measurements," Materials Research Society Symposium Proceedings, vol. 896, pp. 197-202, Nov. 2005.

[1-5]Martin, M., "Processing and characterization of energetic and structural behavior of nickel aluminum with polymer binders," PhD Thesis, Georgia Institute of Technology, April 2005.

[1-6]Thadhani, N.N., "Shock-induced chemical reactions and synthesis of materials," Progress in Materials Science, vol. 37,pp. 117-226, 1993.

[1-7]Graham, R.A., Solids Under High-Pressure Shock Compression, New York: Springer-Verlag, 1993.

[1-8] Rice, M.H., McQueen, R.G., and Walsh, J.M., "Compression of solids by strong shock waves," In Solid State Physics, vol. VI, edited by F. Seitz and D. Turnbull, New York: Academic Press, 1958, pp. 1-63.

[1-9]Herrmann, W., "Constitutive equation for the dynamic compaction of ductile porous materials," Journal of Applied Physics, vol. 40, no. 6, pp. 2490-99, May 1969.

[1-10]Carroll, M.M., and Holt, A.C., "Suggested modification of the P-α model for porous materials," Journal of Applied Physics, vol. 43, no. 2, pp. 759-61, Feb. 1972.

[1-11]Mackenzie, J.K., "The elastic constants of a solid containing spherical holes," Proceedings of the Physical Society, Section B, vol. 63, pp. 1-11, Jan. 1950.

[1-12]Carroll, M.M., and Holt, A.C., "Static and dynamic pore-collapse relations for ductile porous materials," Journal of Applied Physics, vol. 43, no. 4, pp. 1626-36, Apr. 1972.

[1-13]Kenkre, V.M., and Endicott, M.R., “A theoretical model for compaction of granular materials,” Journal of the American Ceramic Society, vol. 79, no. 12, pp. 3045-54, Dec. 1996.

[1-14]Raybould, D., Morris, D.G., and Cooper, G.A., “A new powder metallurgy method,” Journal of Materials Science, vol. 14, no. 10, pp. 2523-6, Oct. 1979.

[1-15]Raybould, D., “The properties of stainless steel compacted dynamically to produce cold interparticle welding,” Journal of Materials Science, vol. 16, no. 3, pp. 589-98. Mar. 1981.

[1-16]Morris, D.G., “Melting and solidification during dynamic powder compaction of tool steel,” Metal Science, vol. 15, no. 3, pp. 116-24, Mar. 1981.

[1-17]Kasiraj, P., Vreeland Jr., T., Schwarz, R.B., and Ahrens, T.J., “Shock consolidation of a rapidly solidified steel powder,” Acta Metallurgica, vol. 32, no. 8, pp. 1235-41, Aug. 1984.

[1-18]Schwarz, R.B., Kasiraj, P, Vreeland Jr., T., and Ahrens, T.J., “A theory for the shock-wave consolidation of powders,” Acta Metallurgica, vol. 32, no. 8, pp. 1243-1252, Aug. 1984.

[1-19]Raybould, D., “The cold welding of powders by dynamic compaction,” International Journal of Powder Metallurgy & Powder Technology, vol. 16, no. 1, pp. 9-14, 16-19, Jan. 1980.

[1-20]Gourdin, W.H., “Energy deposition and microstructural modification in dynamically consolidated metal powders,” Journal of Applied Physics, vol. 55, no. 1, pp. 172-81. Jan. 1984.

[1-21]Gourdin, W.H., “Prediction of microstructural modifications in dynamically consolidated metal powders,” In Shock Waves in Condensed Matter – 1983. Proceedings of the American Physical Society Topical Conference, pp. 379-82, edited by J.R. Asay, R.A. Graham, and G.K. Straub, New York: Elsevier, 1984.

[1-22]Gourdin W.H., “Dynamic consolidation of metal powders,” Progress in Material Science, vol. 30, no. 1, pp. 39-80, 1986.

[1-23]Gourdin, W.H., “Local microstructural modification in dynamically consolidated metal powders,” Metallurgical Transactions A, vol. 15A, no. 9, pp. 1653-64, Sept. 1984.

[1-24]Roman, O.V., Nesterenko, V.F., and Pikus, I.M., “Influence of the powder particle size on the explosive pressing process,” Combustion, Explostion, and Shock Waves (English Translation of Fizika Goreniya i Vzryva), vol. 15, no. 5, pp. 644-49, Sept.-Oct. 1979.

[1-25]Santiso, E, and Müller, E.A., “Dense packing of binary and polydisperse hard spheres,” Molecular Physics, vol. 100, no. 15, pp. 2461-69, August 2002.

[1-26]Cumberland, D.J. and Crawford, R.J., The Packing of Particles, Ch 4, Amsterdam: Elsevier, 1987.

[1-27]Cumberland, D.J. and Crawford, R.J., The Packing of Particles, Ch 8, Amsterdam: Elsevier, 1987.

[1-28]Yang, R.Y., Zou, R.P., and Yu, A.B., "Effect of material properties on the packing of fine particles," Journal of Applied Physics, vol. 94, no. 5, pp. 3025-3034, September 2003.

[2-1] G.L. Benavides, D.P. Adams, and P. Yang: Meso-scale Machining Capabilities, *SAND2001-1708*, Sandia National Laboratory, Albuquerque, NM (2001).

[2-2] M. Geiger, M. Kleine, R. Eckstein, N. Tiesler, and U. Engel: Microforming, *CIRP Annals-Manufacturing Technology*, **50 [2]**, 445 (2001).

[2-3] R. Schuster, V. Kirchner, P. Allongue and G. Ertl: Electrochemcial micromachining, *Science*, **289** [5476] 98 (2000).

[2-4] R.Z. Valiev, R. K. Isamgaliev, and I.V. Alexandrov: Bulk nanostructured materials from severe plastic deformation. *Prog. Mater. Sci*., **45**, 103 (2000).

[2-5] R.Z. Valiev, Y. Estrin, Z. Horita, T.G. Langdon, M. J. Zehetbauer, and Y. T. Zhu: Producing bulk ultrafine-grained materials by severe plastic deformation, *JOM*, **58-4**, 43 (2003).

[2-6] V.V. Stolyarov, Y.T. Zhu, I.V. Alexandarov, T.C. Lowe, and Z. Z. Valiev: Grain refinement and properties of pure Ti processed by warm ECAP and cold rolling, *Mater. Sci. Eng.* **A 343** [1-2], 43 (2003).

[2-7] M.R. Shankar, R. Verma, B.C. Rao, S. Chandrasekar, W.D. Compton, A. H. King, and K. P. Trumble: Severe plastic deformation of difficult-to-deform materials at near-ambient temperatures, *Metal. Mater. Trans.*, **A 38**, 1899 (2007).

[2-8] T.L. Brown, S. Swaminathan, S. Chandrasekar, W.D. Compton, A. H. King, and K. P. Trumble: Low-cost manufacturing process for nanostructured metals and alloys, *J. Mater. Res.*, **17**, 2484 (2002).

[2-9] M.R. Shankar, B.C. Rao, S. Lee, S. Chandrasekar, A. H. King and W. d. Compton: Severe plastic deformation (SPD) of titanium at near-ambient temperature, *Acta. Mater.*, **54** [14], 3691 (2006).

[2-10] W. Moscoso, M.R. Shankar, J.B. Mann, W.D. Compton, and S. Chandrasekar: Bulk nanostructured materials by large strain extrusion machining. *J. Mater. Res.*, **22**, 201 (2007).

[2-11] J.D. Embury and R.M. Fisher: The structure and properties of drawn pearlite, *Acta Metall.*, 14, 147 (1966).

[2-12] V.M. Segal, V.I. Reznikov, A.E. Drobyshevskiy, and V.I. Kopylov: Plastic working on metals by simple shear. *Russian Metallurgy* **1**, 99 (1981), and V.M. Segal: Materials processing by simple shear, *Mater. Sci. Eng. A* **197**, 157 (1995).

[2-13] Z. Horita, T. Fujinami, N. Nemoto, and T.G. Langdon: Equal-channel angular pressing of commercial aluminum alloys: grain refinement, thermal stability and tensile properties, *Metall. Mater. Trans. A* **31**, 691 (2000).

[2-14] A.P. Zhiyaev, S. Lee, G.V. Nurislamova, R.Z. Valiev, T.G. Langdon: Microhardness and microstructural evolution in pure nickel during high-pressure torsion. *Scripta Mater.*, **44**, 2753 (2001).

[2-15] D.A. Hughes, N. Hansen: Microstructure and strength of nickel at large strains. *Acta Mater.*, **48**, 2985 (2000).

[2-16] L. De Chiffre: Extrusion cutting of brass strips. *Int. J. Mach. Tool Des. Res.*, **23**, 141, (1983)

[2-17] W.C. Oliver and G.M. Pharr: An improved technique for determining hardness and modulus using loading and displacement sensing indentation technique, *J. Mater. Res.*, 17 [6], 1564 (1992).

[2-18] G.L. Benavides, L.F. Bieg, M.P. Saavedra, and E.A. Bryce: High aspect ratio meso-scale parts enabled by wire micro-EDM, *Microsyst. Technol.*, **8** [6], 295 (2002).

[2-19] G.L. Wynick and C.J. Boehlert: Use of electropolishing for enhanced metallic specimen preparation for electron backscatter diffraction analysis, *Mater. Charact.*, **55** [3], 190 (2005).

[2-20] M.R. Shankar, B.C. Rao, S. Chandrasekar, W.D. Compton, and A.H. King, Scr. Mater. (2007), published online, doi:10.1016/j.scriptamat.2007.11.040.

[2-21] S. Seaminathan, T.L. Brown, S. Chandrasekar, T.R. McNelly, and W. D. Compton: Severe plastic deformation of copper by machining: microstructure refinement and nanostructure evaluation with strain, *Scr. Mater.*, **56** [12], 1047 (2007).

[2-22] M.R. Shankar, S. Chandrasekar, A.H. King, and W.D. Compton: Microstructure and stability of nanocrystalline aluminum created by large strain machining. *Acta Mater.*, **53**, 4781 (2005).

[2-23] W.C. Liu, Z. Chen, and M. Yao: Effect of cold rolling on the precipitation behavior of delta phase in Inconel 718, *Metall. Mater. Trans. A*, **30A** [1], 31 (1999).

[2-24] W.C. Liu, F.R. Xiao, M. Yao, Z.L. Chen, S.G, Wang and W.H. Li: Quantitative phase analysis of Inconel 718 by X-ray diffraction, *J. Mater. Sci. Lett.*, **16** [9], 769 (1997).

[2-25] D. Y. Cai, W.C. Liu, R.B. Li, W. H. Zhang, and M. Yao: On the accuracy of X-ray diffraction quantitative phase analysis method in Inconel 718, *J. Mater. Sci*., **39** [2], 719, (2004).

[2-26] C. Slama, C. Servant, and G. Cizeron: Aging of Inconel 718 alloy between 500 and 750 degrees C, *J. Mater. Res*., **12** [9], 2298 (1997).

[2-27] L. A. Chapman: Application of high temperature DSC technique to nickel based superalloys, *J. Mater. Sci*., **39** [24], 7229 (2004).

[3-1] K.S. Kumar, H. Van Swygenhoven, et al.:Mechanical behavior of nanocrystalline metals and alloys, *Acta materialia*, **51** [19], 5743 (2003).

[3-2] L. Lu, M.L. Sui, et al.: Superplastic extensibility of nanocrystalline copper at room temperature, *Science*, **287** [5457], 1463 (2000).

[3-3] M.A. Meyers, A. Mishra, et al.: Mechanical properties of nanocrystalline materials, *Progress in Materials Science*, **51** [4], 427 (2006).

[3-4] H. Briesen: Electrically assisted aerosol reactors using ring electrodes, *MRS Symposium Proceeding*, **520** [3], (1998).

[3-5] J.D. Embury and R.M. Fisher: Structure and properties of drawn pearlite, *Acta Metallurgic*a, **14** [2], 147 (1966).

[3-6] G. Langford and M. Cohen: Strain hardening of iron by server plastic deformation, *ASM Transactions Quarterly*, **62** [3], 623 (1969).

[3-7] T.L. Brown, S. Swaminathan, et al.: Low-cost manufacturing process for nanostructured metals and alloys, *J. Mater. Res.*, **17** [10], 2484 (2002).

[3-8] M.R. Shankar, S. Chandrasekar, et al.: Characteristics of aluminum 6061-T6 deformed to large strain by machining," *JOM*, **56** [11], 224 (2004).

[3-9] S. Swaminathan, M. Ravi Shankar et al.: Large strain deformation and ultra-fine grained materials by machining, *Mater. Sci. Eng.*, **A410-411**, 358 (2005).

[3-10] M.R. Shankar, B.C. Rao et al.: Severe plastic deformation (SPD) of titanium at near-ambient temperature, *Acta materialia*, **54** [14], 3691 (2006).

[3-11] E. O. Hall: Deformation and aging of mild steel, *Physical Society – Proceeding*, **64** [381B], 747 (1951), and E. O. Hall: Variation of hardness of metals with grain size, *Nature*, **173** [4411], 948 (1954).

[3-12] N. J. Petch: Cleavage strength of polycrystals, *Iron and Steel Institute – Journal*, **174** (Part 1), 25 (1953).

[3-13] Christopher J. Saldana: Nanostructured particulate by modulation-assisted machining, Master thesis, Purdue University, West Lafayette, Indiana (2006).

[3-14] R.Z. Valiev and T.G. Langdon: Principle of equal-channel angular processing as a processing tool for grain refinement, *Progress in Materials Science*, **51** [7], 881 (2006), and F.H. Dalla Toore, E.V. Pereloma, et al.: Strain hardening behavior and deformation kinetics of Cu deformed by equal channel angular extrusion from 1 to 16 passes, *Acta Materialia*, **54** [4], 1135 (2006).

[3-15] R.Z. Valiev and R.K. Islamgaliev et. al.: Bulk nanostructured materials from severe plastic deformation, *Progress in Materials Science*, **45** [2], 103 (2000).

[4-1] H. Gleiter, Nanostructured Materials: State of the Art and Perspectives, *NanoStructured Materials*, 1995, 6(1-4), p 3-14

[4-2] C. C. Koch, Synthesis of nanostructured Materials By Mechanical Milling: Problemens and Opportunities, *NanoStructured Materials*, 1997, 9(1), p 13-22

[4-3] A. E. Romanov, Continuum Theory of Defects in Nanoscaled Materials, *NanoStructured Materials*, 1995, 6(1-4) p 125-134

[4-4] Trelewicz, J. R. and C. A. Schuh (2007). "The Hall-Petch breakdown in nanocrystalline metals: A crossover to glass-like deformation." Acta Materialia 55: 5948-5958.

[4-5] A. B. Frazier, R. O. Warrington, C. Friedrich, The Miniaturization Technologies: Past; Present; and Future, *IEEE Transactions on Industrial Electronics*, 1995, 42(5), p 423-430

[4-6] K. N. Bhat, Micromachining for Microeletromechanical Systems, *Defense Science Journal*, 1998, 48(1), p 5-19

[4-7] D. P. Adams, M. J. Vasile, A. S. M. Krishnan, Microgrooving and Microthreading Tools for Fabricating Curvilinear Features, *Precision Engineering-Journal of the International Societies for Precision Engineering and Nanotechnology*, 2000, 24(4), p 347-356

[4-8] J. Mohr, LIGA: A Technology for Fabricating Microstructures and Microsystems, *Sensors and Materials*, 1998, 10(6), p 363-373

[4-9] W. Bacher, W. Menz, J. Mohr, The LIGA Technique and Its Potential for Microsystems – A Survey, *IEEE Transactions on Industrial Electronics*, 1995, 42(5), p 431-441

[4-10] S. M. Spearing, Materials Issues in Microelectromechanical Systems, *Acta Materialia*, 2000, 48, p 179-196

[4-11] H. J. Fecht, Nanostructure Formation By mechanical Attrition, *NanoStructured Materials*, 1995, 6(1-4), p 33-42

[4-12] L. Ajdelsztajn, B. Jodoin, G. E. Kim, J. M. Schoenung, J. Mondoux, Cold Spray Deposition of nanocrystalline Aluminum Alloys, *Metallurgical and Materials --Transactions A*, 2005, 36A, p 657-666

[4-13] P. Alkimov, V. F. Kosarev, A. N. Papyrin, A Method of Cold Gas-Dynamic Deposition, *Sov. Phys. Dokl*, 1990, 35(12), p 1047-1049

[4-14] D. L. Gilmore, R. C. Dykhuizen, R. A. Neiser, T. J. Roemer, M. F. Smith, Particle Velocity and Deposition Efficiency in the Cold Spray Process, *Journal of Thermal Spray Technology*, 1999, 8(4), p 576-582

[4-15] R. C. Dykhuizen, M. F. Smith, D. L. Gilmore, R. A. Neiser, X. Jiang, S. Sampath, Impact of High Velocity Cold Spray Particles, *Journal of Thermal Spray Technology*, 1999, 8(4), p 559-564

[4-16] A. C. Hall, D. J. Cook, R. A. Neiser, T. J. Roemer, D. A. Hirschfeld, The Effect of a Simple Annealing Heat Treatment on the Mechanical Properties of Cold-Sprayed Aluminum, *Journal of Thermal Spray Technology*, 2006, 15(2), p 233-238

[4-17] R. C. Dykhuizen and M. F. Smith, Gas Dynamic Principles of Cold Spray, Journal of Thermal Spray Technology, 1998, 7(2), p 205 - 212

[4-18] J. Eckert, Relationships Governing the Grain Size of Nanocrystalline Metals and Alloys, *NanoStructured Materials*, 1995, 6(1-4), p 431-416

[5-1] Welch, C.M., and Compton, R.G., “The use of nanoparticles in electroanalysis: a review”, Anal. Bioanal. Chem., vol. 384, no. 3, pp. 601-619, 2006.

[5-2] Dresselhaus, M.S., et al., “New directions for low-dimensional thermoelectric materials”, Advanced Materials, vol. 19, no. 8, pp. 1043-1053, 2007.

[5-3] Dao, M., et al., “Toward a quantitative understanding of mechanical behavior of nanocrystalline metals”, Acta Materialia, vol. 55, no. 12, pp. 4041-4065, 2007.

[5-4] Das, S.K., Chow, S., Patel, H., “Heat transfer in nanofluids – a review”, Heat Transfer Engineering, vol. 27, no. 10, pp. 3-19, 2006.

[5-5] Koch, C.C. Nanostructured Materials: Processing, Properties, and Applications (2nd ed.) William Andrews Publishing, New York, NY, 2007.

[5-6] Oelhafen, P., and Schüler, A., “Nanostructured materials for solar energy conversion”, Solar Energy, vol. 79, no. 2, pp. 110-121, 2005.

[5-7] Suryanarayana, C., “Recent developments in nanostructured materials”, Advanced Engineering Materials, vol. 7, no. 11, pp. 983-992, 2005.

[5-8] Han, B.Q., et al., “Processing and behavior of nanostructured metallic alloys and composites by cryomilling”, Journal of Materials Science, vol. 42, no. 5, pp. 1660-1672, 2007.

[5-9] Han, B.Q., Mohamed, F.A., Bampton, C.C., and Lavernia, E.J., “Improvement of toughness and ductility of a cryomilled Al-Mg alloy via microstructural modification”, Metallurgical and Materials Transactions A, vol. 36A, no. 8, pp. 2081-2091, 2005.

[5-10] Lee, Z, et al., “Bimodal microstructure and deformation of cryomilled bulk nanocrystalline Al-7.5Mg alloy”, Materials Science and Engineering A, vol. 410-411, pp. 462-467, 2005.

[5-11] Huang, X., Hansen, N. Tsuji, N., “Hardening by annealing and softening by deformation in nanostructured metals”, Science, vol. 312, no. 5771, pp. 249-251, 2006.

[5-12] Fecht, H.J., “Nanostructure formation by mechanical attrition”, NanoStructured Materials”, vol. 6, pp. 33-42, 1995.

[5-13] Swaminathan, S., et al., “Nanostructured materials by machining”, American Society of Mechanical Engineers, Manufacturing Engineering Division, MED, vol. 16-2, pp. 981-985, 2005.

[5-14] Swaminathan, S., et al., “Severe plastic deformation (SPD) and nanostructured materials by machining”, Journal of Materials Science, vol. 42, no. 5, pp. 1529-1541, 2007.

[5-15] Atkinson, H.V., and Davies, S., “Fundamental aspects of hot isostatic pressing: an overview”, Metallurgical and Materials Transactions A, vol. 31 A, no. 12, pp 2981-3000, 2000.

[5-16] Ye, J., Ajdelsztajn, L., Schoenung, J.M., “Bulk nanocrystalline aluminum 5083 alloy fabricated by a novel technique: cryomilling and spark plasma sintering”, Metallurgical and Materials Transactions A, vol. 37 A, no. 8, pp 2569-2579, 2006.

[5-17] Ajdelsztajn, L., Jodoin, B., Kim, G.E., and Schoenung, J.M., “Cold spray deposition of nanocrystalline aluminum alloys”, Metallurgical and Materials Transactions A, vol. 36 A, no. 3, pp. 657-666, 2005.

[5-18] Jin, Z.Q., et al., “Shock compression response of magnetic nanocomposite powders”, Acta Materialia, vol. 52, no. 8, pp. 2147-2154, 2004.

[5-19] Chen, T., Hampikian, J.M., Thadhani, N.N., “Synthesis and characterization of mechanically alloyed and shock-consolidated nanocrystalline NiAl intermetallic”, Acta Materialia, vol. 47, no. 8, pp. 2567-2579, 1999.

[5-20] Morris, D.G., “Melting and solidification during dynamic powder compaction of tool steel”, Metal Science, vol. 15, no. 3, pp. 116-124, 1981.

[5-21] Gourdin, W.H., “Energy deposition and microstructural modification in dynamically consolidated metal powders”, Journal of Applied Physics, vol. 55, no. 1, pp. 172-181, 1984.

[5-22] Brochu, M., et al., “Dynamic consolidation of nanostructured Al-7.5%Mg alloy powders”, Materials Science and Engineering A, vol. 466, no. 1-2, pp. 84-89, 2007.

[5-23] Raybould, D., Morris, D.G., Cooper, G.A., “A new powder metallurgy method”, Journal of Materials Science, vol. 14, no. 10, pp. 2523-2526, 1979.

[5-24] Nieh, T.G., et al., “Dynamic compaction of aluminum nanocrystals”, Acta Materialia, vol. 44, no. 9, pp. 3781-3788, 1996.

[5-25] Liao, X.Z., et al., “Nanostructures and deformation mechanisms in a cryogenically ball-milled Al-Mg alloy”, Philosophical Magazine, vol. 83, no. 26, pp. 3065-3075, 2003.

[5-26] Goods, S.H., and Brown, L.M., “The nucleation of cavities by plastic deformation”, Acta Metallurgica, vol. 27, no. 1, pp. 1-15, 1979.

[5-27] Fredenburg, D.A., Vogler, T.J., Saldana, C.J., Thadhani, N.N., “Shock consolidation of nanocrystalline aluminum for bulk component formation”, in Shock Compression of Condensed Matter – 2007, American Institute of Physics, vol. 955 pp. 1029-1032, 2007.

[5-28] Hugo, R.C., and Hoagland, R.G., “In-situ TEM observation of aluminum embrittlement by liquid gallium”, Scripta Materialia, vol. 38, no. 3, pp. 523-529, 1998.

[5-29] Lao, X.Z., et al., “Deformation mechanisms in nanocrystalline Al: partial dislocation slip”, Applied Physics Letters, vol. 83, no. 4, pp. 632-634, 2003.

[5-30] Warner, D.H., Sansoz, F., and Molinari, J.F., “Atomistic based continuum investigation of plastic deformation in nanocrystalline copper”, International Journal of Plasticity, vol. 22, no. 4, pp. 754-774, 2006.

[5-31] Derlet, P.M., and Van Swygenhoven, H., “Length scale effects in the simulation of deformation properties of nanocrystalline metals”, Scripta Materialia, vol. 47, no. 11, ppl 719-724, 2002.

[5-32] Zhu, Y.T., and Langdon, T.G., “Influence of grain size on deformation mechanisms: an extension to nanocrystalline materials” Materials Science and Engineering A, vol. 409, no. 1-2, pp. 234-242, 2005.

[5-33] Zhu, Y.T., et al., “Nucleation and growth of deformation twins in nanocrystalline aluminum”, Applied Physics Letters, vol. 85, no. 21, pp. 5049-5051, 2004.

[5-34] Gray, G.T., “Deformation twinning in al-4.8 wt% Mg”, Acta Metallurgica, vol. 36, no. 7, pp. 1745-1754, 1988.

[5-35] Bae, D.H., and Ghosh, A.K., “Cavity formation and early growth in a superplastic Al-Mg alloy”, Acta Materialia, vol. 50, no. 3, pp. 511-523, 2002.

[6-1] Koch, C.C. Nanostructured Materials: Processing, Properties, and Applications (2nd ed.) William Andrews Publishing, New York, NY, 2007.

[6-2] Ajdelsztajn, L., Jodoin, B., Kim, G.E., Schoenung, J.M., Mondoux, J., “Cold spray deposition of nanocrystalline aluminum alloys”, Metallurgical and Materials – Transactions A, vol. 36A, pp. 657-666, 2005.

[6-3] Ajdelsztajn, L., Jodoin., B., and Schoenung, J.M., “Synthesis and mechanical properties of nanocrystalline Ni coatinga produced by cold gas dynamic spraying”, Surface and Coatings Technology, vol. 201, pp. 1166-1172, 2006.

[6-4] Kim, H.J., Lee, C.H., Hwang, S.Y., “Fabrication of WC-Co coatings by cold spray deposition”, Surface and Coatings Technology, vol. 191, pp. 335-340, 2005.

[6-5] Phani, P.S., Vishnukanthan, V., Sundararajan, G, “Effect of heat treatment on properties of cold sprayed nanocrystalline copper alumina coatings”, Acta Materialia, vol. 55, pp. 4741-4751, 2007.

[6-6] Brochu, M., Zimmerly, T., Ajdelsztajn, L., Lavernia, E.J., and Kim, G., “Dynamic consolidation of nanostructured Al-7.5%Mg alloy powders”, Materials Science and Engineering A, vol 466, pp. 84-89, 2007.

[6-7] Lee, Z., Witkin, D.B., Radmilovic, V., Lavernia, E.J., and Nutt, S.R., “Bimodal microstructure and deformation of cryomilled bulk nanocrystalline Al-7.5Mg alloy”, Materials Science and Engineering A, vol. 410-411, pp. 462-467, 2005.

[6-8] Chen, T., Hampikian, J.M., and Thadhani, N.N., “Synthesis and characterization of mechanically alloyed and shock consolidated nanocrystalline NiAl intermetallic”, Acta Materialia, vol. 47, pp. 2567-2579, 1999.

[6-9] Tanimoto, H., Pasquini, L., Prummer, R., Knonmuller, H., and Schaefer, H.-E., “Self-diffusion and magnetic properties in explosion densified nanocrystalline Fe”, Scripta Materialia, vol. 42, pp. 961-966, 2000.

[6-10] Chen, K.H., Jin, Z.Q., Li, J., Kennedy, G., Wang, Z.L., Thadhani, N.N., Zeng, H., Cheng, S.-F., Liu, J.P., “Bulk nanocomposite magnets produced by dynamic shock compaction”, Journal of Applied Physics, vol. 96, pp. 1276-1278, 2004.

[6-11] Hall, A.C., Brewer, L.N., Roemer, T.J., “Preparation of aluminum coatings containing homogeneous nanocrystalline microstructures using the cold spray process”, Journal of Thermal Spray Technology, vol. 17, pp. 352-359, 2008.

[6-12] Hall, A., Yang, P., Brewer, L., Buchheit, T., and Roemer, T., “Preparation and mechanical properties of cold sprayed nanocrystalline aluminum”, Expected submission to Journal of Thermal Spray Technology.

[6-13] Fredenburg, D.A., Vogler, T.J., Thadhani, N.N., Dance, W., “Shock consolidation of nano-crystalline 6061 aluminum powders”, Expected submission to *Metallurgical and Materials Transactions; A*

[6-14] Eckert, J., “Relationships governing the grain size of nanocrystalline metals and alloys”, Nanostructured Materials, vol. 6, pp. 413-416, 1995.

[6-15] Dykhuizen, R.C., Smith, M.F., Gilmore, D.L., Neiser, R.A., Jiang, X., and Sampath, S., “Impact of high velocity cold spray particles”, Journal of Thermal Spray Technology, vol. 8, pp. 559-564, 1999.

[6-16] Nishijima, S., Ishii, A., Kanazawa, K., Matsuoka, S., and Masuda, C., *Fundamental Fatigue Properties of JIS Steels for Machine Structural Use*, National Research Institute for Metals, Ibaraki, 1989, p. 77.

[6-17] Dieter, G.E., *Mechanical Metallurgy*, McGraw-Hill, New York, 1986, p. 189.

[6-18] Elmustafa, A.A., Stone, D.S., “Indentation size effect in polycrystalline F.C.C. metals”, Acta Materialia, vol. 50, pp. 3641-3650, 2002.

9 DISTRIBUTION

External Mailings

1 David Anthony Fredenburg
Georgia Institute of Technology
Love Bldg. Rm. 165
771 Ferst Dr.
Atlanta, GA 30332

1 Christopher Saldana
School of Industrial Engineering
Purdue University
315 N. Grant Street
West Lafayette, IN 47907-2023

Sandia National Laboratories – Internal Mailings

1	MS0123	Donna Chavez, LDRD	01011
1	MS1130	Aaron Hall	01813
1	MS1130	Timothy Roemer	01813
1	MS1245	David Gill	02452
1	MS1245	Pin Yang	02454
1	MS9042	Tracy Vogler	08776
1	MS0899	Technical Library	9536 (electronic copy)
1	MS0123	Donna Chavez, LDRD	1011 (electronic copy)

Sandia National Laboratories